THE SYNTHESIS AND CHARACTERISATION OF CONFINED POLYOXOMETALATES WITHIN NANOSTRUCTURED CARBON

MATTHEW GEORGE KEMP

Thesis submitted to the University of Nottingham for the degree of Master of Research

Acknowledgements

I would like to thank all members of the Khlobystov research group for making this an enjoyable year. I would especially like to thank them for making me feel welcome throughout my time in the laboratory. The contagious passion the group has for their research, created a perfect environment to develop as a chemist. Their friendship and support mean a lot, and I am proud to be part of such a committed group.

I would like to thank my supervisor Prof. Andrei Khlobystov for providing me with the opportunity to complete this research project. I thoroughly enjoyed working on a project with industrial applications, where his insight and guidance throughout the project has been invaluable. Throughout the year I have had his constant support, scientific advice and scientific interpretation. We have had numerous scientific discussions; and his knowledge has been priceless, his enthusiasm for knowledge is infectious.

Finally, I would like to gratefully acknowledge the mentorship I have received from both Jack Jordan and Max Astle. They have constantly supported me throughout this project, with frequent suggestions along with cheerful moments. Both Jack and Max were able to find the perfect level guidance, allowing development of my skills and this project to be my own work, however, always being available to intervene and steer me in the right direction whenever they judged it was required. I appreciate the time both Max and Jack donated to acquire countless TEM images, along with PXRD data. The commitment, guidance and support both two has dedicated towards me has been impeccable and has significantly contributed to the enjoyment and success of the project.

I would also like to say a big thankyou to my girlfriend who has always support me, even though the tough times in this project when I wanted to quit. She always taught me to push through to my goals and achieve the impossible.

Abstract

This study reveals the confinement effects of four different polyoxometalates within graphitised carbon nanofibers. A standard ionic liquid mediation filling procedure was developed for the encapsulation of POMs within GNFs. The basic characteristics of each polyoxometalate were analysed using a wide range of analytical techniques such as FTIR, PXRD and TGA, each POM was then compared to each other to gain further understanding on how both Keggin and Wells-Dawson type polyoxometalates function under a constricted space.

POMs@GNF composites were characterised via TGA, PXRD, TEM, EDX and electrochemical techniques. It was noted that precursor concentration was found to influence particle aggregation, location of POM deposition and both thermal and catalytic activity of POM@GNF composites. Besides being hollow nano-containers, GNFs can act as templates for the growth of bulk metal oxides. Preliminary electrocatalyst tests were also undertaken with some of the POM samples, indicating that on encapsulation they retain their redox based behaviour. Overall, this work provides examples of heteronuclear polyoxometalate encapsulation within GNFs and also explains how the synergistic effects between POMs and GNFs leads to an electronic coupling system in which electrons from the metallic like GNF are preferentially donated to POM guest species.

Introduction

1.1 Polyoxometalates

Polyoxometalates (POMs) can be defined as early transition metal clusters and are considered as one of the most popular growing fields within research and development today, not only are they popular in electrocatalysis, but they are also popular in other regions of research such as desulfurization and energy storage. POMs are comprised of oxygen and early transition metals (e.g. M = Mo, W, V or Ta) and these transition metals are at their highest oxidation states. They also may contain a variety of heteroatoms which include (X = P, As, Si and Ge). Overall, POMs can be defined as molecular oxides which are distinguishable from the majority of metal oxides.[1]. They may contain tens to hundreds of metal atoms which can reach nucleraties as high as 368 metal atoms in one single cluster molecule, these clusters then go on to form what we know as POM nanoparticles. Berzelius reported the first synthesised POM around the early 19th century, however in 1864 it was Marignac who successfully synthesised silicotungstic acid.[2] There are numerous applications of POMs as acid and oxidation catalysts both in homogenous and in heterogenous conditions. Polyoxometalates can be classified as isopolyanions and heteropolyanions and they are frequently formed in aqueous media. However, in some cases the assembly of the oxoanions may also occur in non-aqueous media or even in the solid state such as in minerals. The stability of POMs in aqueous or non-aqueous solvents is generally measured by their ability to retain their structural properties without undergoing degradation or transformation to other forms/decomposition products. Nevertheless, POMs under particular conditions may undergo degradation and thanks to modern techniques, we now have a clearer understanding of the mechanisms behind why POMs transform from one to state to another during this process.[3] The two basic structures of POMs are the Keggin structure ($X/M = \frac{1}{2}$) and the Wells-Dawson structure in which ($X/M = {}^{2}/_{28}$). The assembly of two or several Keggin or Dawson fragments leads to the formation of other complex polyoxometalate structures **fig 1.**[4] POMs are formed via the condensation of multiple oxometalte precursors in acidic conditions and in the presence of hetero anions templated structures can form, with the templating anions forming at the centre of the oxometallate cage **fig 2.** Considerable interest surrounding POMs use as photo- catalysts, electro-catalysts and electrochemical storage materials are due to their highly rich and reversible redox chemistry.[5] The numerous metal centres in high oxidation states means that electrons can rapidly and reversibly transfer. This electron transfer can be photochemically or electrochemically induced.[6-7]

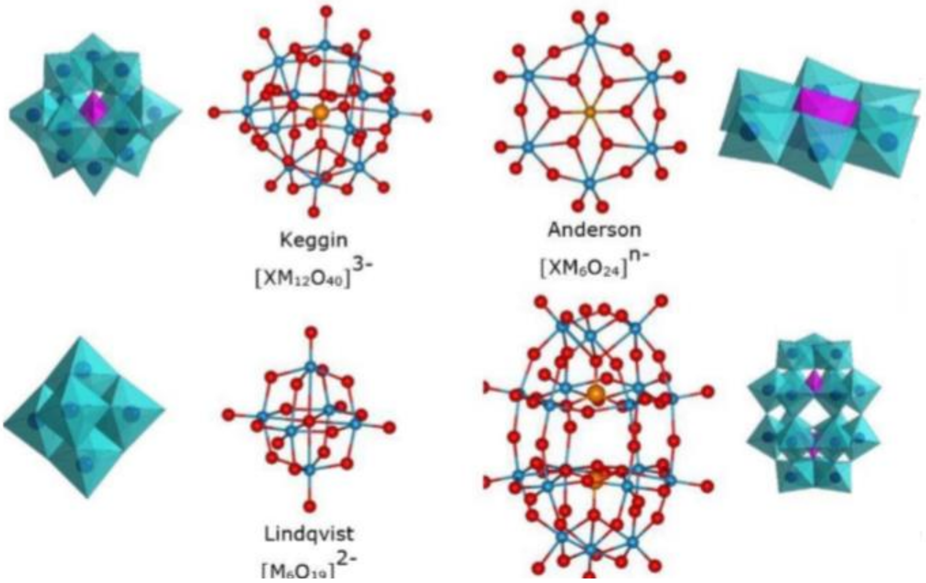

Figure 1. Common POM structures from the literature. Polyhedral models show a metal atom at the centre of each polyhedral, with an oxygen at every vertex. Template anions can be seen at the centre of each structure. Next to each structure a tetrahedron ball and stick model can be seen.

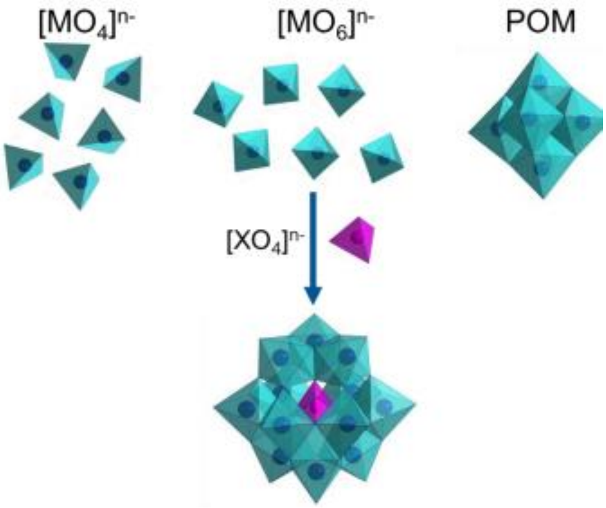

Figure 2. POM formation from oxometallate precursors under acidic conditions.

1.2 POM structure types

The structure of polyoxometalates contain a high atomic proportion of oxygen atoms that are linked to different clusters, they also often contain at least two other elements. One of these other elements is a transition metal atom from group V or VI in its highest oxidation state, e.g. (Mo^{6+} or W^{6+}) or more commonly known as addenda atoms. The second is called a heteroatom and its proportion is much smaller than its counterpart e.g. (P^{5+} or Si^{4+}). The existence of the enormous variety of polyoxometalates synthesised today is because more than half of the elements in the periodic table can be incorporated within the structure of these compounds. Overall the composition of these clusters can be very complex because various elements can be present in the structure. A general classification of the two different POM structures used in this thesis are given below. This classification is mainly focused on polyoxometalates that fall under the Keggin and Wells-Dawson structure type due to their important use in catalysis and electrocatalysis. Let it be noted that the crystal structure of a heterpolycompound is governed by two basic principles.

- *Any atom (M) is in the centre of polyhedral cavities, usually octahedral, forming a polyhedral type MO_x through coordination of P-D π bonds. The oxygen atoms are located at the top.*
- *The polyoxometalates are characterized by octahedral MO_6 units that can have no more than two vertices free by oxygen atoms.*[8-9]

1.3 The Keggin Structure Type

The basic structural unit of a keggin polyoxometalate consists of a central tetrahedron $[X_n^+O_4]$ (8-n) surrounded by 12 octahedral MO_6 groups which organise themselves into four groups of M_3O_{13} that share vertices or edges in order to minimise electrostatic repulsion between themselves. If we look in detail to the primary structure of the Keggin POM, we can see that there are four different types of oxygen[10] **fig 3.**

- *12 corner-sharing oxygen atoms, these oxygens connect the octahedra's that share the vertex and not share any internal oxygens*
- *4 internal oxygens connecting the atom to the triads of octahedra M_3O_{12}*
- *12 edge-sharing oxygen atoms; they connect the octahedra that share the edge connecting two addenda that share the same internal oxygens*
- *12 terminal oxygen atoms; are connected to only one M with partial double bonds.*

1.4 The Wells-Dawson structure

The Wells-Dawson or simply named the Dawson polyoxoanion can be assigned the general formula $[X_2M_{18}O_{62}]$ where (M = W or Mo), and X is a fundamental central heteroatom which can include As, V or Si. This central heteroatom forms two tetrahedral heteroanions in which units of PO_4^{3-} form together to make the metal-oxide framework. It is known that the tungsten Dawson anion, can be synthesised by refluxing sodium tungstate solution with excess H_3XO_4 and subsequently isolated via the addition of potassium or ammonium cations or by ether extraction in which the free acid can be utilised. The molybdenum Dawson structure can be synthesised through the direct dimerization of XMo_9 anions. There are to date only six known isomers of the $[X_2M_{18}O_{62}]^{n-}$ structure which are assigned with the following prefixes. α, α*, β, β*, γ, and γ*. The structural composition of the most common α-isomer can be described as two A- type -$\{XM^9\}$ units coordinated together **fig 4**.[11-12] This dimerization takes places directly in the synthesis of $[X_2M_{18}O_{62}]^{n-}$

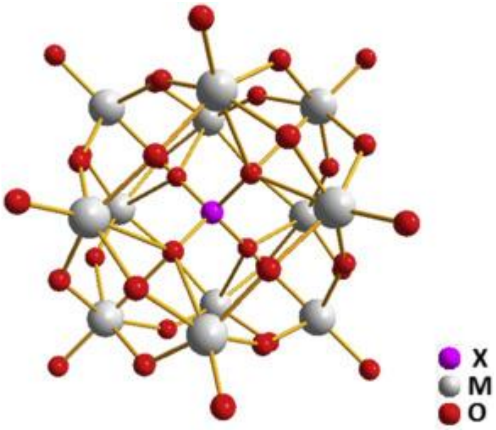

Figure 3. The structure of the Keggin anion [$X_3M_{12}O_{40}$]. The red segments represented the 12 terminal oxygen atoms and 4 internal oxygen. The pink segment represents the "addenda atom" and the grey segments represent the metal atoms.

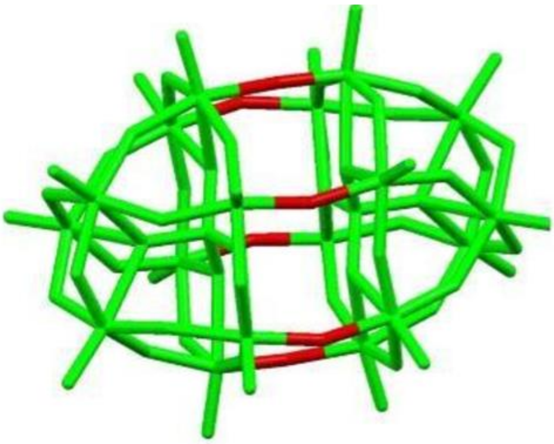

Figure 4. The structure of the Wells-Dawson anion [$X_2M_{18}O_{62}$]$^{2x-16}$. The green segments represent the A-type [XM_9] units with a direct link (red segment) across the lacunae structure.

2.0 Polyoxometalate reactivity

2.1 Acidic properties

It has long since been demonstrated that acidic varieties of POMs such as $H_3PW_{12}O_{40}$ exhibit Bronsted acid like properties in the solid state and therefore they are more potent acids in relation to more conventionally used solid acids such as SiO_2-Al_2O_3. It can be deemed that heteropolyacids are much stronger compared to that of oxoacids of both constitute elements and ordinary mineral acids. This strong acidity is caused by a multitude of factors of which are:

Dispersion of the negative charge that lays over most of the atoms on the polyanion. This coupled with the fact that the negative charge is less distributed over the outer surface of the polyanion which is owed to the double bond character of the M=O which in turn polarises the negative charge of the terminal oxygen to the metal. [13-14]

The secret into the effectiveness of polyoxoanions as catalysts is their high Bronsted acidity associated with them. This elevated Bronsted acidity is a result of the large polarisation of the negatively charged polyoxoanionic species. Their acid-base properties can be varied over a broad range by altering their chemical composition. Some POMs exhibit unique structures which exhibit exceptionally high proton mobility, in which heteropolyanions can stabilise cationic organic in addition to inorganic intermediates.[15-16] In aqueous solution acidic forms of POM, are strong, fully dissociated acids. It has been shown that $PW_{12}O_{40}^{3-}$ anions remain deprotonated even after the acceptance of two and three electrons respectively. In solution, POMs are stronger than the usual mineral acids such as H_2SO_4, HCl and HNO_3. The central atom is the important factor in determining the acid strength and the acidity related to the total charge on the anion. [17-18]

Redox properties 2.2

The addenda metal atoms in most POMs are in their highest oxidation states (d^0) and it is therefore clear that these complexes are in general capable of acting as oxidising agents, they are also bonded to O_2^- ligands, which produce very ionic strucures.[19] Formally, we have pairs like W_6^+ O_2^- which can be compared to metal oxide crystals since the surface of their molecular oxo metal aggregates are similar to that of infinite surfaces. Overall there is little ligand-to-metal donation in their structure, so metal centres are willing to accept external electrons because their valence shell is empty.[20] The overall charge of these anions depends on the heteroatom X and on the addenda metal. Fully oxidised M atoms in POMs usually have formal charges between 4^+ and 6^+. Obviously, the state of reduction of these molecules can vary this number. Even though they are negatively charged, reductions are common and often accompanied by protonation.[21] It was noted that certain polyanions, especially that of the 12-molybdo Keggin type species were readily reduced to form blue species more commonly known as heteropoly-blues or molybdenum blues[22]. In most of the POMs structures the addenda atoms occupy "octahedral" sites with either one or two terminal oxygen atoms. As a result, they can undergo facile reversible reductions to yield species of the type {MOL5} in which one or more of the metal centers has been reduced to the [d^1] configuration.[23] Based upon the solvent, the acidity of the solution and the charge of the polyanion can differ. The reductions involve either single electron or multielectron steps which are often followed by protonation. It can be shown that the oxidation potential is highly dependent on that of the addenda atom and is widely influence by that of the central hetero atom. Overall, the oxidation potentials of polyanions containing MO are high and these ions are easily reduced.

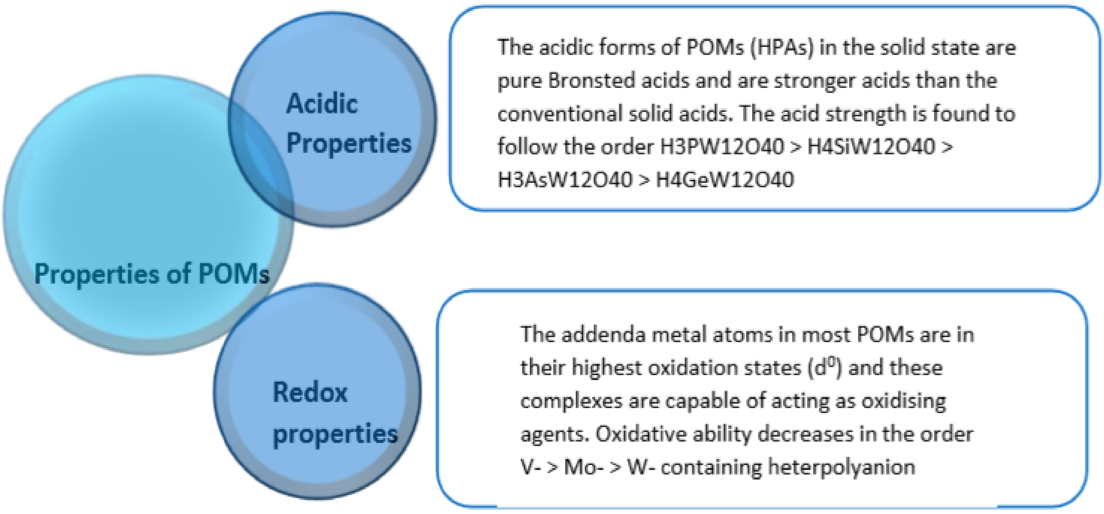

The acidic forms of POMs (HPAs) in the solid state are pure Bronsted acids and are stronger acids than the conventional solid acids. The acid strength is found to follow the order H3PW12O40 > H4SiW12O40 > H3AsW12O40 > H4GeW12O40

The addenda metal atoms in most POMs are in their highest oxidation states (d^0) and these complexes are capable of acting as oxidising agents. Oxidative ability decreases in the order V- > Mo- > W- containing heterpolyanion

Figure 5. A summary of the various properties of POMs and the explanation behind these properties.

2.3 Electrochemical properties

Souchay pioneerd the application of electrochemistry to the study of POMs via the field of polarography. [24] However, it was not until the late 1960's when more detailed investigations were done. Based on these studies it was shown that heteropolyanions undergo several rapid one and two electron reversible reductions to produce so called "heteropoly blues" it was also noted that further irreversible multielectron reductions were possible with POM decomposition.[25] The electrons are accepted by the addenda ions of the heteropolyanions $[XM_{12}O_{40}]^{n-}$. If the addenda ions are identical, then the electrons become delocalized on the addenda oxide framework in a process known as rapid electron hopping (intramolecular electron transfer). This reduction increases the overall negative charge density of the heterpolyanions and thus their basicity is also increased. It is well documented that one-electron waves in acidified media, in which protonation accompanies the reduction are converted into two electron waves. As the pH of the solution is increased, the reduction potentials become more negative (0.060 V/pH unit) until a pH is reached at which point the reduced POM is no longer protonated. It was shown that both Keggin and Dawson-type heteropolyanions undergo several one-electron reductions when not protonated and their reduction potentials were not pH-dependent. Keggin- type heterpolyanions can accept a limited number of electrons without undergoing decomposition, and in some cases the reduced compounds have been able to be isolated. It can be shown that in general, the reduction potentials of the Keggin heterpolytungstates are controlled by 2 factors;

1) Their reducibility increases in the sequence α-, β-, and γ-isomers according to the number of rotated M_3O_{13} *groups*

2) The reduction potential of the one-electron waves decreases linearly with a decrease in the valence of the central metal, i.e., an increase in the negative charge of the heteropolyanions.

Under alkaline pH conditions, reduced POMs are kinetically more stable than their oxidised self's. Solutions of reduced POMs can be generated via controlled electrolysis under appropriate conditions of both solvent an acidity. It has been shown in some studies reduced anions undergo irreversible isomerization. e.g polarograms of reduced Keggin and Wells-Dawson anions in aqueous and organic solvents show that they gradually transform from α to β isomers. This is due to two different behaviours. [26]

1) *The more positive reduction potentials of the β isomers*

2) *The lability of polyoxometalates compared to polyoxotungstates.*

2.4 Mixed- Valence POMs

As mentioned earlier, heteropoly blues are reduced POMs where extra electrons have been delocalized over the d-metal orbitals. The name is given due to the blue colour that is observed when a POM is reduced, however the term "heteropoly blue" is normally given to any reduced species for ease of convivence. Overall the most widely studied heteropoly blues are the Wells-Dawson and Keggin POMs. In the Keggin anions all the metal centres are regarded as equivalent, however in the Wells-Dawson anion two types of metal atoms are distinguished, commonly regarded as the "cap and belt" positions. It has been noted that ESR spectra of one-electron reduced anions show a very broad or sometimes unobservable line at room temperature. These observations are interpreted according to the model of mixed-valence metal centres, in which a delocalised electron at high temperatures becomes trapped on a metal atom as the temperature is gradually lowered.[27]

Although most talk is centred around "heteropoly blues", there is also something called "heterpoly browns" these are mixed valence compounds where the extra electrons are localized on specific atoms. [28]

2.5 Electrocatalytic performance

Overall there are three type of electrocatalytic processes associated with POM systems. The first is Homogenous electrocatalytic reduction: as mentioned previously after the reduction of many POMs on an electrode, a series of heteropoly blues are formed. These anions most often have increased electrocatalytic activity and can be used in some reactions. For example, [α-[$SiW_{12}O_{40}^{4-}$] in acidic aqueous solution is easily reduced to [α-$SiW_{12}O_{40}^{5-}$] and [α-$H_2SiW_{12}O_{40}^{6-}$] on the cathode and exhibit a high electrocatalytic activity for nitrite ion reduction and hydrogen evolution.[29]

The second type is homogeneous electrocatalytic oxidation. Due to the central atom and the coordination atom in the POM being in their highest valence state, it is difficult to reoxidise them on the anode and therefore it is necessary to replace one or more of the coordination atoms with some transition metal/lanthanide ions with a variable valence which allows them to be used as electrocatalytic oxidants. For example, ruthenium substituted $[PW_{11}O_{39}RU (H_2O)]^{4-}$ has the ability to ease lose two electrons and therefore oxidises to $[PW_{11}O_{39}RuO]^{4-}$ the oxidation in turn catalyses the oxidation of organic compounds such as alcohols and dimethyl sulfoxide.[30]

The third type is heterogenous electrocatalysis and can be used to modify electrode surfaces, heteropoly anions can be used to modify electrode surfaces, e.g in conducting polymers for use in heterogenous electrocatalysis. For example, the Wells-Dawson anion [$P_2W_{18}O_{62}^{6-}$] can be incorporated into electrodes of 4-vinylpyridine-12-dibromodecane. These modified electrodes maintain the electrocatalytic properties of the heteropoly anions in solution and in some instances, they have a better and increased catalytic effect. [31]

2.6 Application of POMs

Since the discovery of POMs, scientific researchers have found significant value in POMs within a variety of fields such as science and technology. The research area in regard to POM chemistry is roughly about two centuries old, however they are still nonetheless a rapidly growing group of compounds especially due to their large domains of applications among the community of which include: the modification of carbon electrodes, capacitors, colorants for pigmenting paints and solar cell, energy storage and catalysis. Among the numerous applications, catalysis is by far the most important and it forms the major bulk of the total field of applications. POM based catalysts have played an important role in the field of acid as well as oxidation catalysis due to their high Bronsted acidity as well as their tendency to exhibit fast reversible multi-electron redox transformations under mild conditions and their inherent stability towards oxidants.

2.7 Catalysis using Keggin Type POMs

Hill et al were the first group to use Keggin type POMs as a catalyst.[32] They found that a tetra-substituted Keggin POM $[Fe^{II}_4(H_2O)2(PW_9O_{34})2]^{10-}$ had a incredibly high selectivity to the epoxidation of alkenes, which at the time was not found in any other POMs containing iron. It was therefore shown that POMs with a multi-iron sandwich had a stronger catalytic selectivity to the reaction, this prompted other research groups to try catalysis with differing types of POMs. Subsequenctly Neumann et al used $[WZnMn_2^{II}(ZnW_9O_{34})_2]^{12-}$ as catalysts for the epoxidation of olefins via H_2O_2 oxidation.[33] Overall it shows that high charged POMs are helpful for catalysis and therefore POM chemistry has become a hot topic in recent years.

2.8 Structure of Carbon nanotubes (CNTs)

Carbon nanotubes (CNTs) have attracted great interest from the scientific community since 1991 due to their remarkable physical properties.[34] Most of the current interest in nanotubes is focused on practical applications of CNTs. To use these nanotubes in various applications, it is necessary to modify the nanotubes in various ways. One of these ways is to fill them with foreign materials such as metals or metal oxides, inorganic materials and other compounds [35-37]. It is known that the templating effect provided by the cavities of nanotubes effectively forces inserted materials to adopt a 1-dimensional structure/morphology and leads to alternative routes of 1 dimensional nanocrystal synthetisation.[38] Using nanotubes as a confinement for encapsulated materials, the chances of increased lattice structure deformation or even the formation of new structures is greatly increased and therefore the endless possibility to induce new behaviours or properties/characteristics of encapsulated materials is far more likely to occur. Overall Filling CNTs and GNFs should be preferred over the adsorption of materials onto the outside walls due to the enhanced catalytic effect present with confinement. Up until present, many aspects once concerning researchers about CNTs research development have been overcome. For instance, the synthetic routes for large-scale and diameter-controlled production are well established and supplied commercially and theoretical hypothesis to predict various properties of CNTs are all well supported via experimental and computational results. Due to these great results, more and more research groups are trying to integrate CNTs into already applicable devices and interest in the incorporation of advanced materials within CNTs has greatly increased. However, many challenges with respect to CNT dispersibility and solubility have yet to be overcome. One way to overcome this as mentioned above is to modify the nanotubes via adding groups or via the encapsulation of materials into the cavities, through these modifications, differing composites with increased versatility can be synthesised, allowing for exhibition of more fascinating and different properties then before.[39-41]

Although it is possible for carbon nanotubes to take many forms, to really grasp the structure, it is best to begin with the simplest form of nanotube which is the single walled nanotube (SWCNT). A nanotube is essentially a rolled graphene sheet around one single atom thick of sp^2 hybrized carbon atoms, added to this is two hemifullerences added at each end of the cylinder to close it. Overall there are many ways to roll up graphene into a cylinder and therefore different configurations of nanotubes are available **fig 6-7**. These configurations can be shown via hamada's indices.[42] Hamada's indices state that if a cylinder is formed via the overlap of an O atom with an A atom in another ring of graphene, the helicity vector which is equal to OA can be decomposed into two vectors parallel to the graphene lattice vectors as seen in the equation below:

$$C_h = na^1 + ma^2$$

When N is equal to M or when M or N is 0, in which case c_h is parallel to one of the symmetry planes of graphene, two specific nanotubes can be synthesised: armchair(N=M) and zigzag (N or M=0). When N=M=0 chiral nanotubes can be synthesised.

Multiwalled carbon nanotubes (MWNTs), are comprised of multiple rolled up layers of graphene yielding cylindrical hollow structures of diameter 10-30 nm and interlayer spacing 0.34 nm. The name multiwalled nanotube is restricted to nanostructures with outer diameters of about 30 nm.

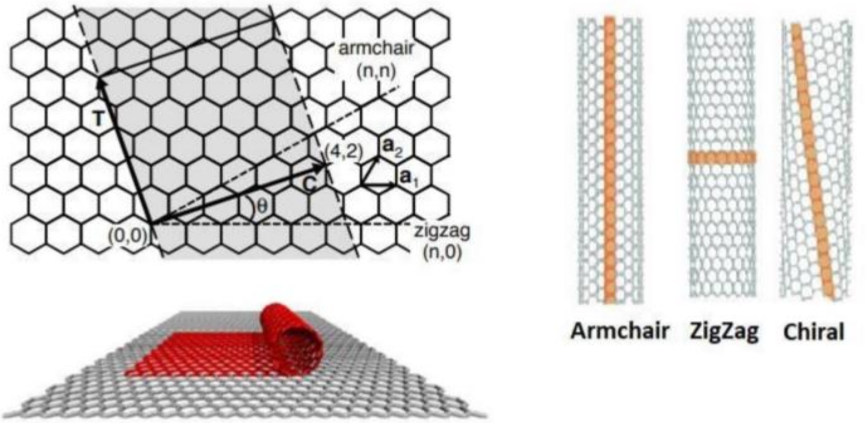

Figure 6. Schematic representation of single-walled carbon nanotubes (SWCNT) (From left to right): Armchair, Zizgzag and Chiral.

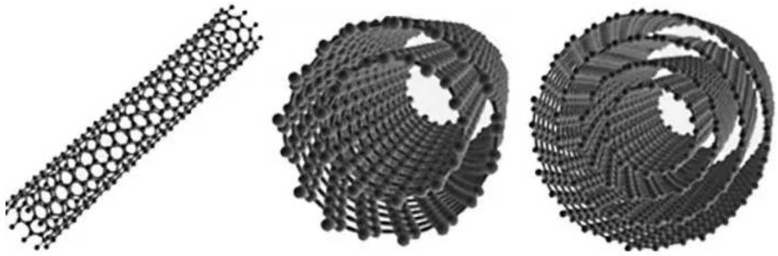

Figure 7. Schematic representation of single-walled carbon nanotubes (SWCNT) Double-walled carbon nanotubes (DWCNT) and multi-walled carbon nanotube (MWCNT)

2.9 Structure of Graphitised carbon nanofibers (GNFs)

Unlike that of carbon nanotubes, Graphitised carbon nanofibers consist of concentric layers of graphene and differ in the sense to other nanotubes in that the structure of their inner and outer surfaces are essentially distinct from each other. The outer surface area of a GNF is composed of a continuous, atomically flat graphene layer (ca. 50 to 60). [43] It should also be noted that their internal surface possesses a succession of step edges which are formed via the rolling up of graphene sheets (3-4 nm high and spaced 8-15 nm away from each other) which overall allows for the formation of a robust hollow structure, as shown in **fig 8**

High resolution transmission electron microscopy (HRTEM) analysis of GNF (Pr-19) clearly shows the structure of the internal step edges and the hierarchical arrangement of the GNF **fig 9**. These step edges can function as possible anchoring points for guest nanoparticles. Hollow graphitised carbon nanofibers (GNF) are considerably wider compared to that of MWCNTs (which on average have internal diameters typically above 50 nm). **Fig 8** reveals HRTEM images of GNF (PR-19) possessing an internal diameter of 65 nm and an outer external diameter of 140 nm. Apart from the robust and hollow structure of GNFs, their wide internal channels allow for the facilitation and effective bulk transport of molecules through their tubular structure. This bulk transport along with the GNFs wide internal channels make it the most suitable candidate for the study of chemical reactions at the nanoscale. In contrast, multiwalled carbon unlike GNFs possess an atomically smooth interior, and hence, control of nanoparticle formation through interactions with the nanotube surface is unfeasible.

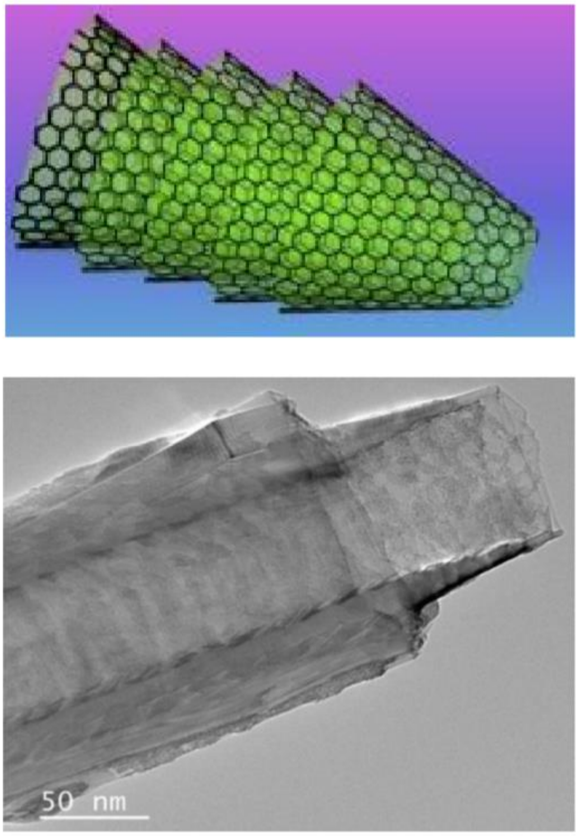

Figure 8. Schematic representation of a graphitised nanofiber (nano-cone stacking) and a GNF TEM image showing the internal structure.

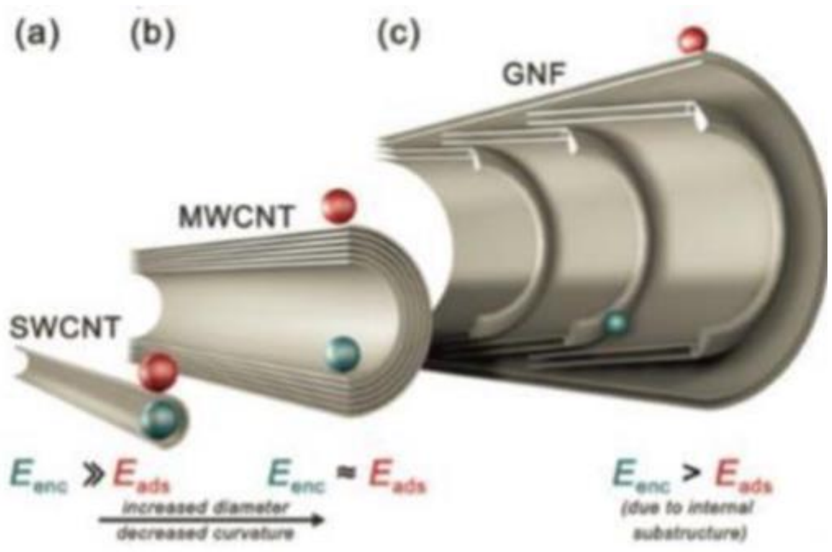

Figure 9. Schematic representation of different morphologies of CNTs and their differing affinities for encapsulation (E_{enc}) and surface adorption (E_{ads})

3.0 Filling Carbon Nanotubes

The motivations with filling CNTs first arrived quickly after they were discovered, however what makes filling nanotubes so special? Firstly, the inner cavity of nanotubes can act as nanoreactors for the synthesis of nanomaterials. Due to the confinement cavity, inserted materials are forced to adopt a 1-dimensional morphology. Furthermore, the encapsulation of materials within CNTs acts as a shelter for these materials from reactions with the surrounding medium, typically oxidation as well as dissolution of the confined material both in aqueous and no aqueous media. In this regard filling CNTs is considered a possible approach to obtain materials that could never had existed unless encapsulated.

3.1 Filling of nanotubes via liquid phase methods.

In the process of liquid phase filling, composites are synthesised by soaking opened CNTs in a concentrated solution of the desired material. Although a wide range of materials are permitted to be introduced into nanotubes this way, it is normally only seen as a candidate when gas phase and molten phase filling has been ruled out, normally due to inappropriate physical properties of the filling material in question. Normally, filling CNTs with inorganic compounds via solution filling requires some sort of post treatment usually through reduction [44] or calcination[45], however chen et al reported a one-step filling process in which he utilised closed nanotubes, metal, nitric acid and heating to force metal nanoparticles within the CNT.[46] After this release a multitude of other research groups started coming up with one-step filling processes. Another example is the synthesis of CrOx@SWCNTs by soaking raw SWCNTs within a super saturated solution of CrO3 in concentrated HCl, in which case the CrO_2Cl_2, facilitated the opening of the SWCNTs.[47] Overall it can be deemed that the solution method is useful for confining molecules and various other nanoparticles within nanotubes **fig 11.**

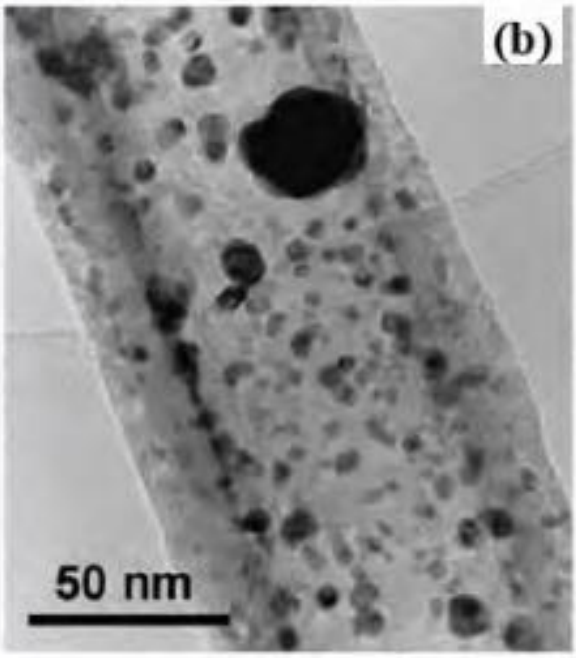

Figure 11. TEM image of MWCNTs filled with Pd nanoparticles prepared by immersing opened MWCNTs into Pd salt solution followed by a calcination and reduction process.

Overall, other than structural benefits it is likewise demonstrated that both the kinetics and selectivity of chemical reactions are ultimately influenced by the confinement of guest species within GNFs. This is due to the spatial confinement imposed on the guest species via the confinement within the GNF, due to this confinement nanoscale chemical transformations in GNF nanoreactors exhibit distinct results compared to the bulk solution or gas phase. For instance, it can be shown that the hydrosilylation reaction of phenylacetylene and triethylsilane within a $[Rh_4(CO)_{12}]$ catalyst nanoscale reactor yields an 8-fold increase in the production of β(E)- vinyl silane in comparison to the reaction which is undertaken in the bulk solution phase. [48] It was also shown that in the oxygen reduction reaction using Pt nanoparticles confined within a GNF the composite retains electrochemical activity after 50000 cycles, whilst the activity of Pt adsorbed onto amorphous carbon without encapsulation greatly reduces the number of cycles that catalyst can undertake to 10000. [49] These effects of confinement are caused by interactions among carbon nano-structures (CNT) and reactants/products, which are summarised by Khlobystov in **table 1** below:

Interactions between CNT and catalyst	Interactions between CNT and reactants	Interactions between CNT and products
Electron transfer between catalyst and interior of CNT	Causes an alignment of reactant within the nanotube which in turn facilitates the reaction	Efficient transport of product molecules from nano-reactor to bulk phase
Surface of nanotube altering the catalytic activity of the guest species	Van der Waals or electron transfer interactions between reactants and nanotube interior in turn lowers activation energy pathway of the reactant	
Enhanced stability of catalyst inside nanotube	Attractive interactive forces occur between the nanotube interior surface and the reactant molecules, which in turn leads to a higher local concentration and effective pressure inside nanostructured carbon systems	Restriction of reaction space inside the interior of the nanotube, allowing for product formation of one product which is stereotypically more favourable

Table 1. Interactions and effects between CNTs and catalysts/reactants.

Taking advantage of GNFs compared to MWCNTs Khlobystov et al. reported GNFs as nano reactors to study chemical transformations in a confined space.[50] Nanostructured metals encapsulated within the hollow structure of GNFs have shown superior catalytic performances in comparison to free standing or surface-adsorbed nano catalysts. To give a few examples, nanoparticles (NPs) of rhodium (Rh) and rhodium-platinum (RhPt) alloy embedded inside GNF for regioselective hydrosilylation of terminal alkynes, Au NPs encapsulated inside GNF for oxidation of silane by hydrogen peroxide, Pt NPs inside GNF for oxygen reduction reaction and Pd complexes inside GNF for Heck reaction. [51-54] Besides high selectivity and conversion, GNF nanoreactors that have an embedded catalyst normally exhibit good recyclability.

Although many investigative reactions have been researched and achieved for metals inside carbon nanotubes and their catalytic applications have been extensively researched, polyoxometalates (POMs) confinement has been studied significantly less. Being mildly like metal-oxide compounds, POMs can offer a new class of materials with more distinct properties when encapsulated within GNFs.

3.2 Confinement of metal oxides/ POMs at nanoscale

The Principle of the encapsulation of metal oxides/POMs within a porous matrix has widely been investigated and used to prepare stable and well dispersed novel materials grown within hollow nanostructures, this allows prevention of sintering of nanoparticles under extreme reaction conditions.[55] Besides stability, nanoparticles offer a broad range of interesting properties which solely come about due to their encapsulation, some of these properties include, modification of redox behaviour, size-controlled growth and catalysis selectivity.[56-57] These properties have been an area of significant interest among the scientific community specifically for their use in preparing stable nanoreactors to study chemical transformations at the nanoscale. Materials that have a porous structure such as CNTs are perfect potential containers for the confinement of POMs and metal oxides. Polyoxometalates encapsulated within MOFs have been applied as nanoreactors for catalysis [58-59]. Ma et al. reported the encapsulation of POMs within cationic metal-organic frameworks (MOFs) that exhibits an increased catalytic activity towards the selective oxidation of Styrene to Benzaldehyde. As a result of this POM encapsulation, the Metal-Organic Framework did not only increase oxidation rates of these aldehyde, it also showed distinct structural stability and high selectivity properties **fig 12.**

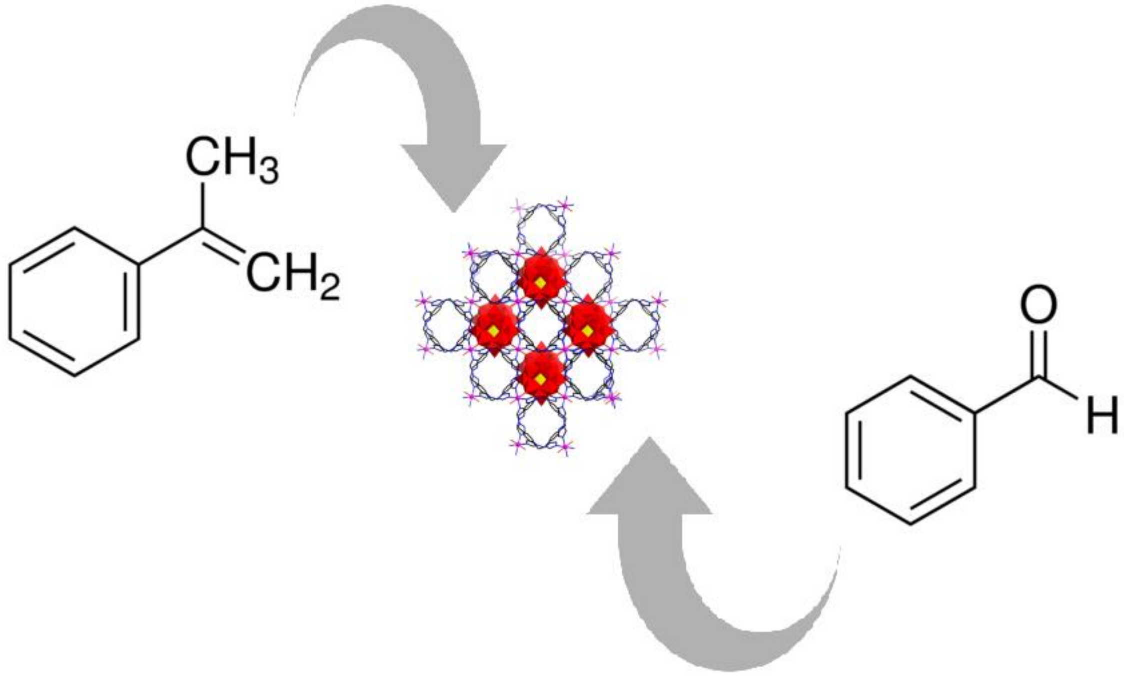

Figure 12. A Schematic Representation of the selective oxidation of Styrene to Benzaldehyde via the use of a Polyoxometalate-based Metal-Organic Framework.

Furthermore, selectivity towards these substrates and the negligible loss of catalytic activity has been observed. Similarly, to MOFs, Carbon nanotubes (CNTs) are also extremely effective for encapsulating nanoparticles due to their porous like structure. Their porosity offers steric restriction to prevent aggregation of nanoparticles and therefore allowing the production of somewhat uniformly distributed nanoparticles inside the internal channels of CNTs.[60]

After the contemplation of MOFs and Zeolites, carbon nanotubes (CNTs) offer the best potential advantages for the encapsulation of guest molecules, specifically POMs. This is due to CNTs unique tubular morphology coupled with their high thermal stability. In CNTs, curvature of the CNT walls causes a shift in the π electron density gradient, as a consequence of this phenomena the increased electron density nanoparticles within the carbon nanotubes exhibit unusual properties which are distinct from those that have been adsorbed onto the outside surface of porous networks or consequently on their own standing.This effect of encapsulation of metal nanoparticles inside CNTs creates a separate class of novel materials which could have promising applications for not only catalysis but for other areas of chemistry, such as electrochemistry, photoactive chemistry and also energy storage. These improved chemical activities of nanoparticles confined within CNTs can be attributed to the effect of spatial confinement at nanoscale, which can result from 4 key factors:

Restricted Space inside the host matrix

Due to the restriction of space within the CNT, small size nanoparticles are prepared, and agglomeration of nanoparticles is prevented. Since agglomeration of particles within CNTs reduced catalytic activity significantly, a lower chance of agglomeration within the CNT offers the best chance for increased activity of the catalyst. For example, Rh-Mn nanoparticles which are confined within a CNT exhibit higher activity for syngas conversion due to the absence of nanoparticle aggregation.[61] Deactivation of iron oxide nanoparticle catalysts adsorbed outside the CNT were observed due to agglomeration in contrast to the better catalytic performance of confined iron oxide nanoparticles within CNTs

Electronic interaction of metal/metal oxide nanoparticles with CNT

Electronic interactions occur between the confined metal nanoparticles and the CNT host, and because of this interaction catalytic activity of encapsulated catalysts can be affected. It was demonstrated in 2010, that Bubeck et al developed a green method for the reduction of GOs via an ultraviolet-irradiated photo reduction process **fig 13**.[62] H_3PW_{12} was used as a photo catalyst and also acted as an anionic surface-active molecule, which further increased rGOs dispersibility within water by attaching to the surface of reduced graphene oxide. The group further reported that the conductivity of the POM-modified reduced graphene oxide can reach as high as 400 S m^{-1}. The results demonstrate that the POM-assisted photo reduction method significantly increased electronic conjugation between GO sheets which resulted in a significantly higher electronic conductivity.

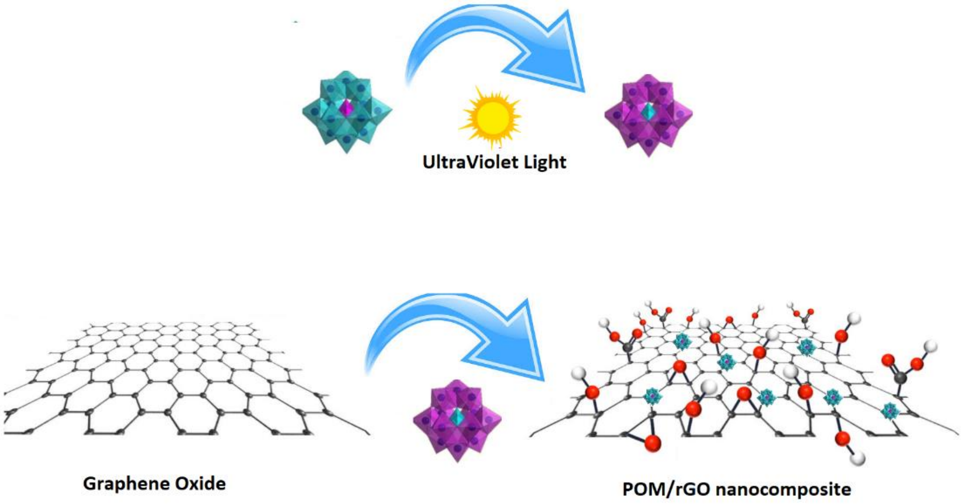

Figure 13. The Photochemical reduction-assisted assembly of POM/rGO nanocomposites.

Enhanced reactant concentration within the CNT

Due to the confined space and therefore strong interactions of reactant molecules within CNTs, it can be said that the concentration of reactants within the CNTs is effectively increased. Due to this increase of concentration, an increased proximity between catalyst and reactants is noted and as reactants increases the reaction rate is accelerated.

Enhanced rate of molecular uptake and release from within the CNT

Transport of molecules within the internal diameters of CNTs become less hindered due to the molecular reordering of incoming molecules within the CNT. Due to this lower transport resistance, rate of reactant molecules is thereby increased which leads to an influences rate of catalytic performance of the confined complex. Due to the above effects, the encapsulation of nanoparticles at the nanoscale level and the preparation of these novel materials with fine-tuned catalytic, electrochemical and photocatalytic attributes have attracted significant attention. Several examples of nanoparticle encapsulation and their significant properties have been demonstrated by several research groups and are outline in **table 2.**

Metal nanoparticles confined within CNTs	Effect on the properties of the material when confined	Properties/Applications of confinement	Reference
Re_xO_y@SWNT	In tubule reduction to metallic rhenium under mild conditions.	Used within mechanistic modelling for heterogenous catalysis.	63
Pd@CNT	Enrichment of reactants inside CNT Channel	92% enantioselective hydrogenation of α, β unsaturated carboxylic acid	64
Pd@MWCNT	Increased selectivity towards C=C bond hydrogenation	Selective hydrogenation of cinnamaldehyde into hydrocinnamaldehyde	65
Cu@MWCNT	Formation of small size particles inside MWCNT and prevention of aggregation	Higher rate of hydrogenation of methyl acetate with Cu@MWCNT	66
FeS_2@CNT	Increased conductivity and structural integrity	High specific capacity and cycling stability as LIBs anodes	67

Table 2. *Summary of confinement of metal nanoparticles within carbon nanotubes (CNTs) and their effects on confinement.*

3.3 POM/Nanocarbon Hybrids

Although the photoactive and redox properties of POMs have already been reviewed, when novel materials such as these are developed and synthesised it really is necessary that we're able to connect these molecular clusters together on a conductive recyclable host as a result of POMs discrete nature and their solubility. CNTs are ideal for this role as they have high conductivity and possess a high surface area. Dispersion of Polyoxometalates onto this carbon support allows for the molecular dispersion of POM clusters which permits each and every anion to participate in energy/electron transfer processes. Nearly every reported POM/CNT hybrid so far has been constructed by means of utilisation of covalent bonding or intermolecular interactions which functionalise binding to the exterior side wall of the CNT **fig 14.**

Figure 14. The functionalisation of CNTs with POMs through the use of covalent bonds

Covalent bonding of polyoxometalates to nanocarbons necessitates access to stable organo-functionalized POMs which is often difficult. This process alone is often quite challenging and frequently difficult as a result of synthetic struggles as more typical functionalisation groups are confined to organo-functionalized alkoxides, which are usually that of phosphonates and silanes. [68] Usually, one organic functionalised group can be linked only with a particular cluster type, however no technique currently exists to accomplish that coordinated functionisation. Additionally, the cluster assembly could also be achieved two ways by means of (direct functionalization) or (post functionalisation) in which both methods face issues. This can make it hard for non-expert chemists to find an ideal synthetic approach. What's more, the bonding between polyoxometalates and functional organic groups can be often considered comparatively weak, which renders the application of these kinds of materials badly hampered.[69]

In general, the development of specialised functionalization routes resulting in stable, long lived organic-inorganic hybrid materials is an important challenge which needs to be solved through the use of modern POM research. So far to date, there is little to no research about this method, however there is a single report of a covalent functionalisation of CNTs with POMs in which the typical approach used within the synthesis is to use a functionalized amide bond.[70] By allowing conversion of the CNT surface acid groups, POMs were able to be introduced, which could then be linked to oxidised nanocarbons through the formation of amide bonds. Together with covalent bonding, there are also non-covalent functionalisation routes that can be often taken to attain the synthesis of POM-CNT hybrids. Non-covalent bonding may be achieved via making use of a range of intermolecular interactions which arise between POMs and CNTs. The current ongoing simplest method to synthesise POM/CNT hybrids is with the use of electrostatic interactions. These interactions allow for the attachment of anionic POMs to positively charged CNTs. Cationic functionalization of CNTs can often be achieved via covalent attachments of cations to the CNT surface, or more commonly through intermolecular interactions in which a cationic species is attached to a CNT through π- π interactions. When an extended aromatic system is covalent bonded to a POM, this hybrid materials enables it to be linked to CNTs via a phenomenon called π-π stacking. As explained previously, this process nevertheless requires access to organofunctionalized POMs which in itself is a struggle to synthesise.

Layer by layer or more widely known as LBL assembly can be accomplished by the recurrent stacking of POMs and CNTs by way of wet chemical deposition methods. **Figure 15** shows through the utilisation of cationic modification methods of CNTs, strong electrostatic interactions can be applied to stack alternating Nano carbon/POM layers. It must be noted that a disadvantage of the LBL deposition technique is that it provides only access to layered structures. Whilst the electronic interaction and dispersion of POM may not be ideal, the simplicity and variability of this synthetic method makes it ideal and therefore it is one of the most commonly used techniques regarding the fabrication of POM nanostructured carbon hybrids.

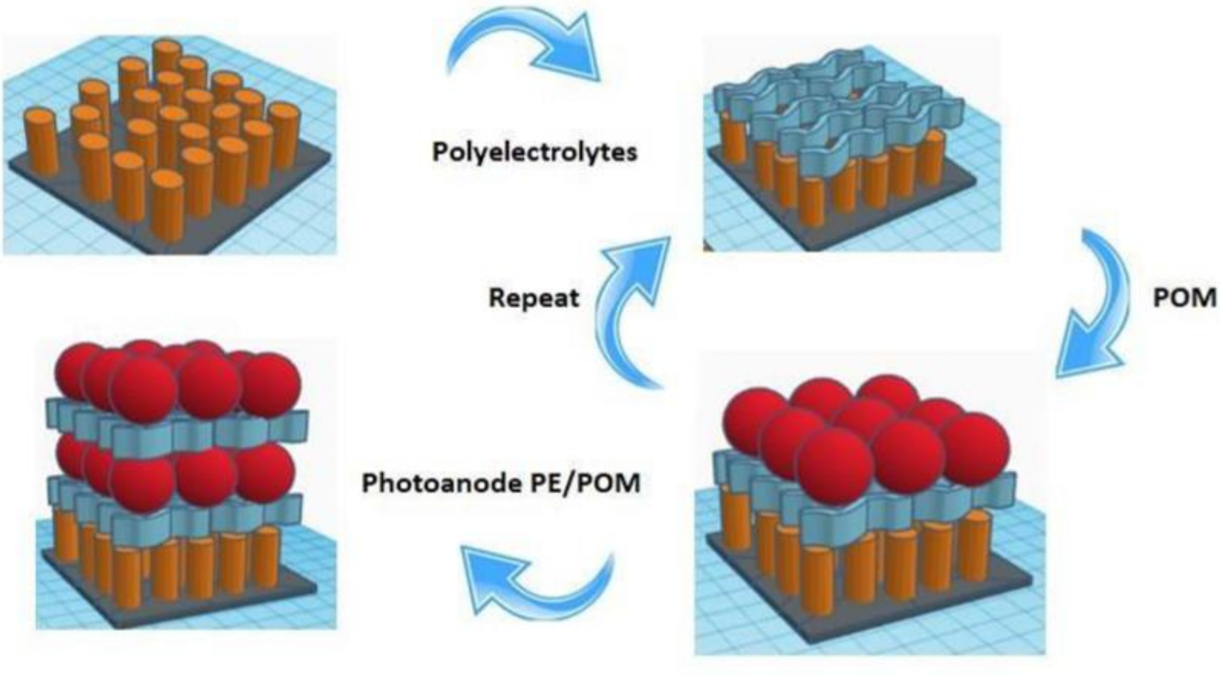

Figure 15. Schematic representation of layer by layer assembly of polyelectrolytes and POMs to form a photoanode PE/POM composite

Besides the above-mentioned fabrication methods of POM/nanocarbon hybrids, electro-assisted or photo-assisted assembly has also been utilised to manufacture POM/nanocarbon hybrids materials. For instance, Wu et al. successfully synthesised a nanocomposite as a result of using SiW_{12}-catalysed electrochemical reductions in which SiW_{12} transferred electrons from the graphene oxide electrode which in turn produced reduced graphene oxide. SiW_{12}

then subsequently adsorbed onto the reduced graphene oxide surface leading to the formation of a highly dispersed, porous SiW_{12}/RGo hybrid.[70] The high porosity of the composite makes the material an interesting applicant for the use in lithium ion batteries as it was shown to have a high specific capacity of around (275 mA h g^{-1}) which is approximately 1.7 times the capacity of pure SiW_{12}. It can be concluded that currently within the scientific research community, POM/nanocarbon composite research has mostly been focused on electrocatalysts for use in electrochemical energy storage.

3.4 Applications of POM/nanocarbon composites

Based on their overall redox-activity POM/nanocarbon composites can be utilised within a wide range of electron transfer and storage processes. At the moment, most of the current research focused around these composites has been centered on electrocatalysis and energy storage systems. For example (? Et al.) showed that the high redox activity of POMs enables them to function as ideal materials for the catalytic transfer of electrons to and from a substrate for use in oxidative electrocatalysis.[71] This application is appealing for the development and functionalised of multi-electron transfer reactions which under normal circumstances are typically hampered due to their high overpotentials which can lead to an overall low conversion. POMs therefore are an ideal prospect material which could be used to increase this low conversion as they are able to be chemically inserted with high redox-active metals e.g (Ru, Mn and Co) **fig 16**. Hence, technologically important electrocatalysts for the splitting of water and other relevant oxidation/reduction reacts become more easily accessible with the successful assembly of a working POM/nanocarbon composite.

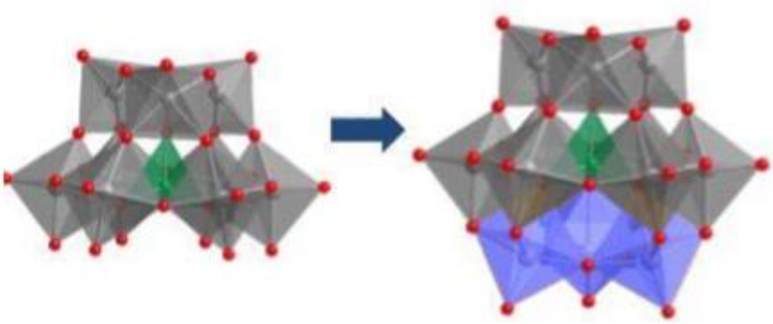

Figure 16. Schematic representation of Lindquist POM anion being chemically insert with a high redox active metal (Ru).

Another use of POM/nanocarbon composites is in water oxidation reaction. It is deemed that water oxidation is usually the most difficult half reaction of the overall water splitting process, this is due to quite high over potentials incurred in the process even whilst using noble metals such as platinum for the basis of the electrode. To overcome this obstacle requires the development and usage of high-functionalised POM based water catalysts which can be further functionalised with redox-active metals such as Ru. Prato et al. electrostatically assembled a POM based water catalyst prototype consisting of $(M_{10}[Ru_4(H2_O)4(u\text{-}O)4(u\text{-}OH)2(y\text{-}SiW_{10}O_{36})_2]$ on multi-walled carbon nanotubes (MWCNTs).[72] This material acted as the conductive substrate for the formation of an active water oxidation catalyst **fig 17.**

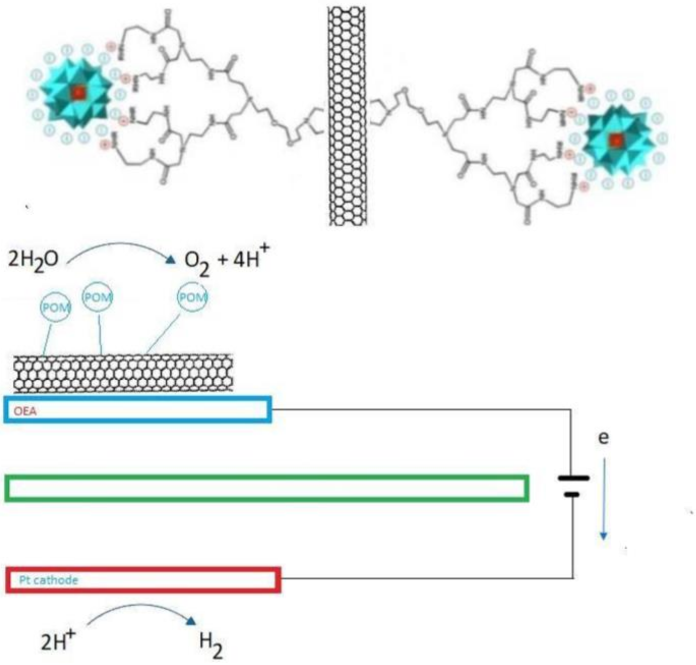

Figure 17. General scheme for a water-splitting electrocatalytic cell with the integrated nanostructured oxygen-evolving anodes.

Perhaps another important use of POM/nanocomposite structure is in the oxidation of methanol, in which the usage of precious metal catalysts to facilitate this reaction has attracted great interest from research groups. Methanol is most used as an energy carrier in which it is considered a direct electron donor in methanol fuel cells.[73] Current typical methanol oxidation systems use noble metals- more commonly platinum. On the other hand, the utilisation of platinum within the electrooxidation of methanol is fairly complex due to the formation of unwanted chemisorbed reaction intermediates such as CO and HCO which can often leads to catalyst poisoning **fig 18.**

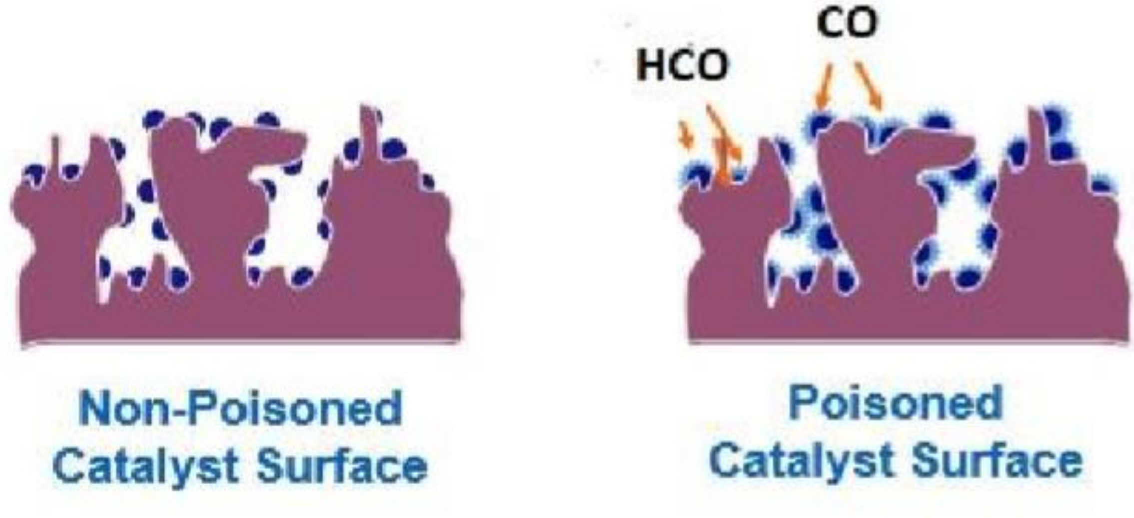

Figure 18. Schematic for "catalyst poisoning" on a catalyst surface, using the intermediates HCO and CO

Incorporating POMs into electrode-based materials is just one viable approach to address this problem. POM clusters can be incorporated and utilised as electro oxidation catalysts whilst serving as electron and proton relays. These electron and proton relays exhibit remarkable thermal and chemical stability, which in turn allows for the long-term use of POM- modified electrodes at temperatures above 100 degrees, this increase in temperature effectively lowers the chance of catalysis poisoning. It was demonstrated in 2006, by Chen et al.[74] that a new catalyst support based on CNTs modified with the Keggin type POM $H_3PMo_{12}O_{40}$ had been synthesised. This new catalyst support demonstrated spontaneous and strong chemisorption of POMs onto the CNT. Throughout their work, the authors describe that the composite was utilised in the use of a redox-active support for highly dispersed Pt and Pt-Ru electrocatalysts which were deposited via electrodeposition. It was determined that the activities of the Pt and Ru nanoparticles were significantly enhanced which was attributed to a wide variety of factors. It was concluded that during early catalytic tests both the combination of the unique electrical properties of CNTs coupled with the high protonic conductivity of POMs lead to an increase in current densities within the composite. Coupled with these increased densities was an increased specific activity and improved cycle stability which had not yet been seen within non-POM modified systems. It was also reported in 2008 that Kim et al proposed the synthesis and functionalisation of a pt@POM/CNT tri-component substituted composite for usage in methanol oxidation which further allowed for the reduction of noble metals used within the composite. The [PMo_{12}] polyoxometalate anion was chemically inserted within a Pt-supported carbon nanotube via colloidal synthesis. It was shown by the group, that this composite proved far superior and exhibited much better Pt-based mass activities along with an increased stability within the use of methanol oxidation compared to other previously synthesis Pt/CNT samples. Overall these publications served as one of the first studies in which POMCNT supports proved viable in the functionalisation of catalytic applications **fig 19.**

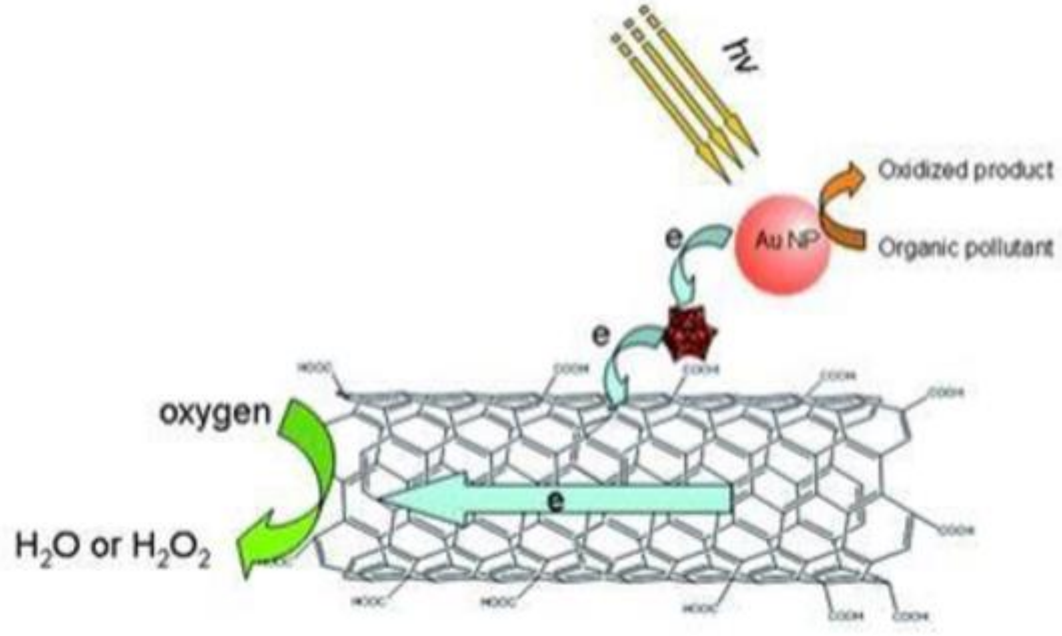

Figure 19. The POM-CNT hybrid synthesised via pan et al. The oxidation of dye occurs at the AuNp-POM site, whilst charge separation is achieved through electron transfer from the CNT where oxygen then becomes reduced

3.5 Scope for further investigation

The confinement of metal nanoparticles inside porous structures has been studied extensively **Table 1,** however attempts to study the effects of the encapsulation of POMs inside nanostructured carbon are limited. To date there are only a handful of papers that have been published which display the effects of Polyoxometalate confinement within carbon nanotubes. Furthermore, graphitised carbon nanofibers which compared to SWNTs are a superior nano-container are an ideal host, for the encapsulation of POM guest species due to their greatly increased surface area. Due to this increased surface area interactions between the nanostructured carbon and POM guest species can be greatly enhanced and therefore it is important to evaluate their catalytic and electrochemical activity. Similar catalytic and electrochemical importance of polyoxometalates adsorbed onto nanostructured carbon has been studied however as mentioned confinement has had limited attempt. The possible nanoscale effects of a POM-GNF hybrid could produce interesting results, which at the moment remain unexplored. Polyoxometalates being unique in redox, electrochemical photoactive and catalytic properties, their confinement could lead to the formation of a variety of interesting nanocomposite materials with properties that could greatly enhance our knowledge in the field.

It can be seen in the literature, that several research groups reveal that both tungsten and molybdenum POM based catalytic systems show excellent potential not only for energy storage but for oxidative desulphurisation (ODS). Despite Mo_X compounds being very active catalysts, it appears that molybdenum POMs have a greater catalytic potential, however accompanied with this increase in catalytic potential arises a multitude of problems including stability issues. Throughout the literature the primary role of these experiments is to disperse the metal POM particles to increase the surface area, which in turn increases the number of POM moieties available for reaction. Graphene oxide is widely used for this, however the application of Graphitised carbon nanofibers (GNFs) is currently gaining traction. GNFs can be defined as quasi one-dimensional materials which are comprised of single, double or multiple layers of graphene and they possess unique electronic, physical and mechanical properties. Overall, they possess an array of excellent of properties which include; excellent electrical conductivity, physiochemical stability and a high surface area. Additionally, due to their high surface area, an expansive array of guest molecules can be encapsulated within the hollow graphitic interior of nanostructured carbon via the utilisation of van der Waals' forces. As consequence of this confinement, synergistic effects can arise between guest molecules and the host GNF, which can lead to the alteration of chemical and physical properties of the guest species in comparison to their properties as a Bulk entity. Overall an exciting application of these hybrid materials is in the role of nanoreactors, in which the kinetics of a chemical reaction may be accelerated, along with the conversion and selectivity of products improved relative to their bulk solution counterparts. It is therefore that study of these new hybrid of novel materials be undertaken to see if better alternatives to already known materials can be found.

3.6 Aims and Objectives

The aim of this study is to further study host-guest interactions of CNTs specifically GNF's through the encapsulation of POMs with specific interest in the interior dimension and the step edges of GNFs and how the encapsulation of the POM guest species properties can be enhanced with confinement. Overall the outlook is to develop novel hybrid nanomaterials through new paths to hybridisation for sustainable catalysis and storage. This will be achieved through the following objectives:

The first objective of this project is to synthesise four different POM catalysts and characterise them. Previous work within other research groups has highlighted both the potential of tungsten and molybdenum POMs for use in both catalysis and electrochemical reactions. In order to further investigate these materials, effective synthesis and characterisation of these POMs must be completed.

The second objective in this project is to develop and synthesise a hybrid material of POMs@GNF and effectively quantify them and compare them to bulk POMs using several techniques. A key aspect of this project is to select suitable POMs which could be suitable in the use of energy storage, whilst remaining stable and also enhancing any properties these POMs may have via their encapsulation within carbon.

The final objective of this project is the preliminary evaluation of the newly synthesised catalyst.

As mentioned previously, many reported efforts to date have mainly centralised and focused on the functionalisation of CNTs through their exterior functionalisation, this study will focus mostly on the encapsulation of POMs within GNFs.

3.7 POM Characterisation

In this chapter, the characterisation of the catalysts chosen and used throughout this work are presented and discussed. The main techniques used in the characterisation of these materials is outlined and described in previous chapters. The catalysts under study include bulk Keggin heteropoly acids $K_3PW_{12}O_{40}$, $K_3PMo_{12}O_{40}$ and the bulk Wells-Dawson heteropoly acids $K_6P_2W_{18}O_{62}$ and $K_6P_2Mo_{12}O_{62}$.

3.8 Thermogravimetric analysis of desired Polyoxometalates.

Thermogravimetric analysis (TGA) was used to determine both the water content and the thermal stability of each individual catalyst synthesised. On a whole, solid heteropoly acid compounds such as those mentioned above accommodate large amounts of water of crystallisation and depending on the amount of hydration water and counter-cation, several crystallographic arrangements of these catalysts exist **fig 20.**

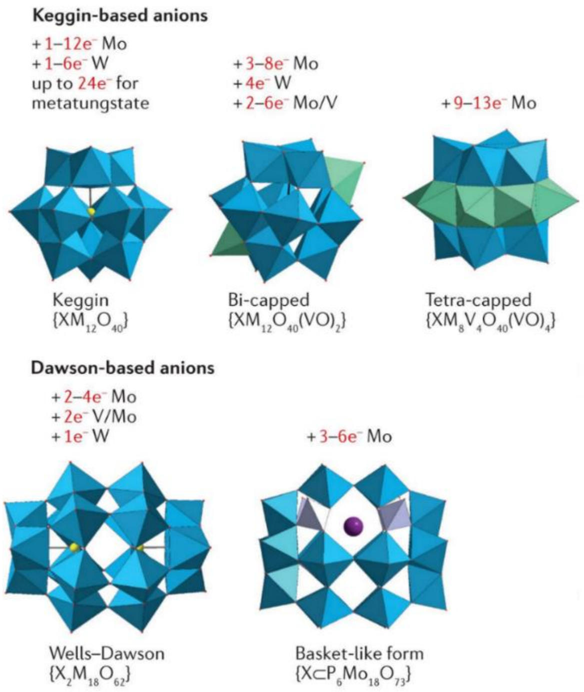

Figure 20. Differing crystallographic arrangements of both Keggin-based anions and Dawson-based anions.

The TGA results for the bulk heteropoly acids are summarised in **table 3.** It should be noted that the results for the bulk Keggin and Wells-Dawson anions are close to the results obtained by other research groups.

Sample Name	Temperature Range Steps (^{O}C)	Weight loss Steps (%)
Wells Dawson Phosphotungstic acid [$K_6P_2W_{18}O_{62}$]	**25-200**	**3.75**
Wells Dawson Phosphomolybdic acid [$K_6P_2Mo_{18}O_{62}$]	**30-125** **125-500** **500-1000**	**5.44** **4.66** **14.68**
Keggin Phosphomolybdic acid [$K_3PMo_{12}O_{40}$]	**50-125**	**2.8**
Keggin Phosphotungstic acid [$K_3PW_{12}O_{40}$]	**50-125** **125-500** **500-1000**	**2.28** **0.72** **9.00**

Table 3. A table to show the comparison in Weight loss (%) of common heteropoly acids at varying temperatures.

The thermal behaviour of heteropoly acid catalysts have already been widely studied and investigated among a multitude of research groups. Three common stages of weight loss have been found upon thermogravimetric analysis of solid heteropoly acid hydrates. To begin with, water of crystallisation evolves when the temperature of the sample is increased from room temperature to 100-125^{O}C. These waters are hydrogen-bonded together and are often zeolitic meaning that they can be easily and reversibly removed from the solid catalyst. This hydration-dehydration process is often accompanied by the continuous expanding and shrinking of the volume of the crystal cell **fig 21**. It should be noted that the amount of crystallisation of water is not easy to control via synthetic methods and thus depends on the conditions under which the acid was prepared. In this case, the first weight loss for each heteropoly acid corresponded at around 30-125^{O}C which is often excess water of crystallisations. In the second stage at around 125-500 ^{O}C stronger bound waters are suggested to hydrate the acidic protons in the heteropoly acid. In contrast a deeper analysis of the synthesised four POM's is explored below.

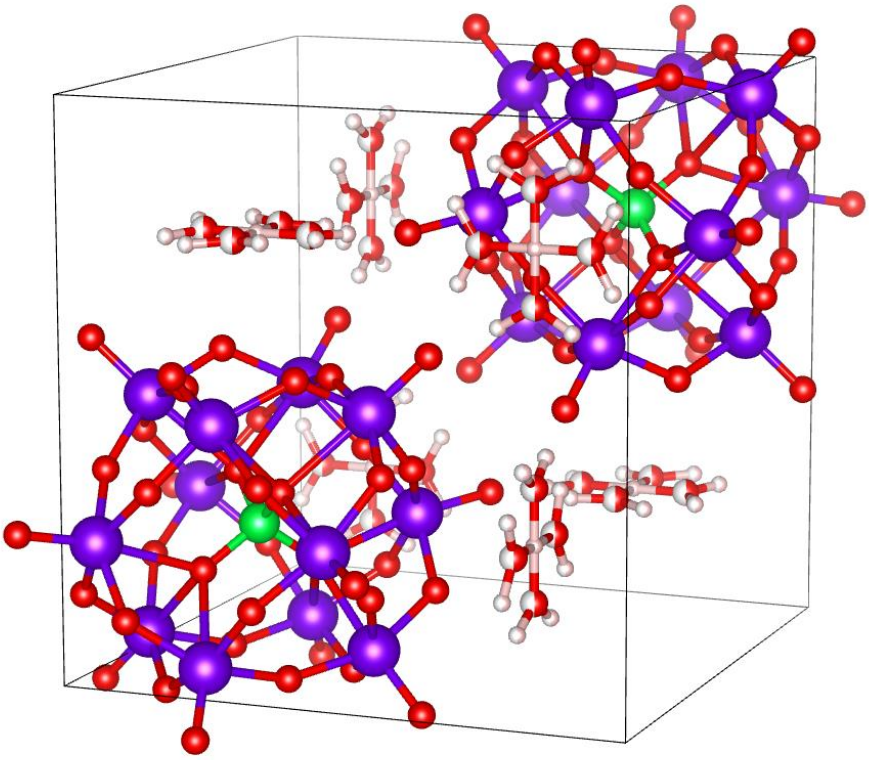

Figure 21. shows the removal of waters of crystallisation from a POM upon heating to a certain temperature.

3.9 Thermogravimetric Analysis (TGA) of $K_3PW_{12}O_{40}$/$K_3PMo_{12}O_{40}$

The vacuum- dried polyoxometalates were compared in order to quantify the amount of water of crystallisation that had essentially been removed with the structural decomposition of the POMs. This was done as the intermediate hydrates increase the overall weight of the POM.XH_2O compound and therefore quantification of the water content was therefore important in order to prepare POM solutions of a specific concentration for filling into the GNFs. TGA profiles of these compounds are shown below in **table 4**

The overall number of water molecules in each case was calculated by the weight loss that occurred from 30-300 ^{O}C. The intermediary hydrates number calculated via TGA were;

Calculated intermediary hydrated POMs Formula
$K_3PW_{12}O_{40}.4H_2O$
$K_3PMo_{12}O_{40}.17H_2O$
$K_6P_2W_{18}O_{62}.6H_2O$
$K_6P_2Mo_{18}O_{62}.13H_20$

Table 4 . The chemical formulas of the intermediary hydrated POMs synthesised.

Thermogravimetric (TGA) analysis of $K_3PMo_{12}O_{40}$ shows two mass loss steps **fig 22** the first signal between 0 and 150 ^{O}C corresponds to the departure of water of crystallisations. A second mass loss at temperatures between 700-1000 ^{O}C was attributed to water content resulting from combination of H^+ ions and network oxygen. This mass loss leads to a reversible modification of the polyanion, which is outlined below.

$$\mathbf{H_3PMo_{12}O_{40}.XH_2O \rightarrow H_3PMo_{12}O_{40} \rightarrow [PMo_{12}O_{38.5}] \rightarrow ½P_2O_5 + 12MoO_3}$$

The $K_3PW_{12}O_{40}$ acid **fig 23** shows three weight loss sections which could be observed at 134, 340 and 500 ^{O}C. The POMs are usually synthesised containing large waters of crystallisation and most of these water molecules are released at around 100 ^{O}C. Two mass loss signals between 50-140 ^{O}C correspond to the departure of water of crystallisations. A second mass loss at temperature between 250-350 ^{O}C, was attributed to water content resulting from combination of H^+ ions and network oxygen. It can be noted that the decomposition of the $PW_{12}O_{40}$ anion is said to take place at around 350-650 ^{O}C and the equation for its decomposition is outlined below.

$$\mathbf{H_3PW_{12}O_{40}.XH_2O \rightarrow H_3PW_{12}O_{40} \rightarrow ½P_2O_5 + 12WO_3 + {}^{3}/_{2}\ 14H_2O}$$

4.0 Thermogravimetric Analysis (TGA) of $K_6P_2W_{18}O_{62}$/ $K_6P_2Mo_{18}O_{62}$

To examine the thermal stability of these compounds, thermal gravimetric analysis was carried out on each sample. Thermogravimetric curves **fig 24** were obtained under the flow air. The thermal analysis of $K_6P_2Mo_{18}O_{62}$ displays a major weight loss at around 25-100 ^{O}C and a minor weight loss at 150-500 ^{O}C and a second major weight loss at 500-1000 ^{O}C. The first change in mass would be related to water loss from $K_6P_2Mo_{18}O_{62}$ upon heating since it contains constitution water molecules. The minor loss and second major loss could be attributed to the beginning of decomposition of the Dawson unit, which becomes significant above temperatures of 500 ^{O}C and undergoes the following decomposition.

$$\mathbf{2H_6P_2Mo_{18}O_{62} \rightarrow 2H_3PMo_{12}O_{40} + H_6P_2Mo_5O_{23} + [Mo_7O_{24}]^{6-}}$$

Compared to that of $K_6P_2Mo_{18}O_{62}$, $K_6P_2W_{18}O_{62}$ shows a single weight loss step at 25-200 ^{O}C which can be attributed to constitution water molecules **fig 25**. It can be shown that unlike the other POMs tested, $K_6P_2W_{18}O_{62}$ shows remarkable stability and does not decompose under higher temperatures unlike that of its Keggin counterpart. As there are no decomposition stages for this unlike other POMs, no decomposition equation can be shown.

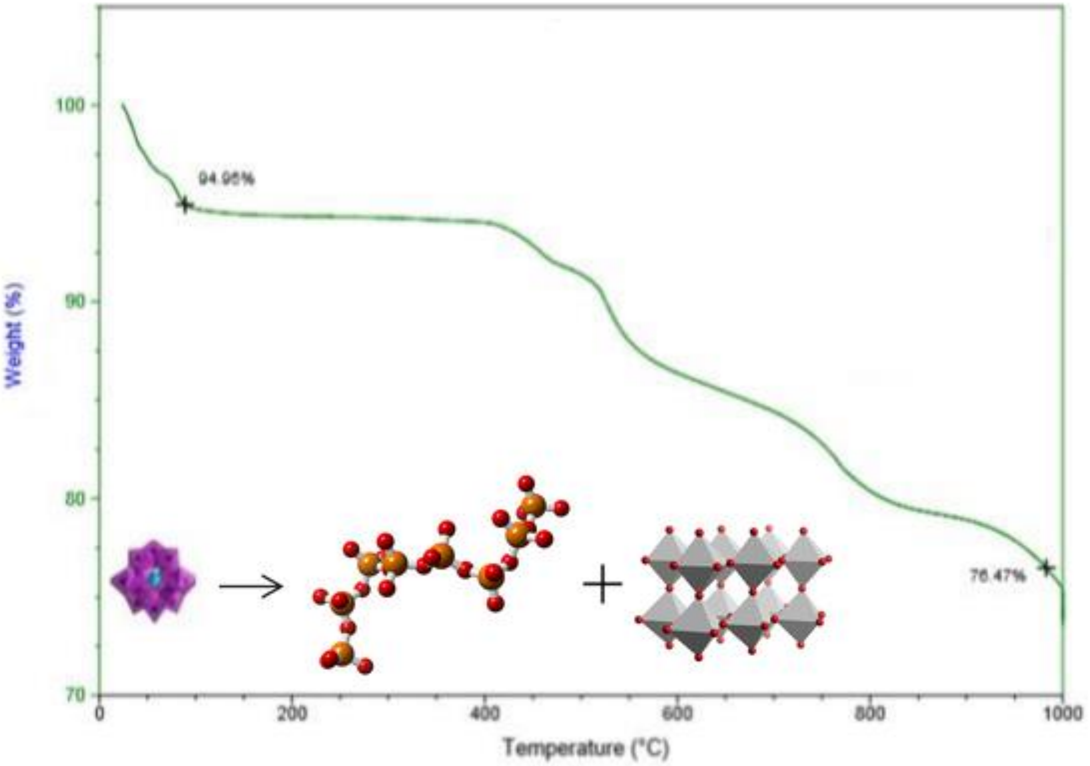

Figure 22. Thermogravimetric analysis of $K_3PMo_{12}O_{40}$ showing mass losses at 0-150 and 700-1000 °C respectively

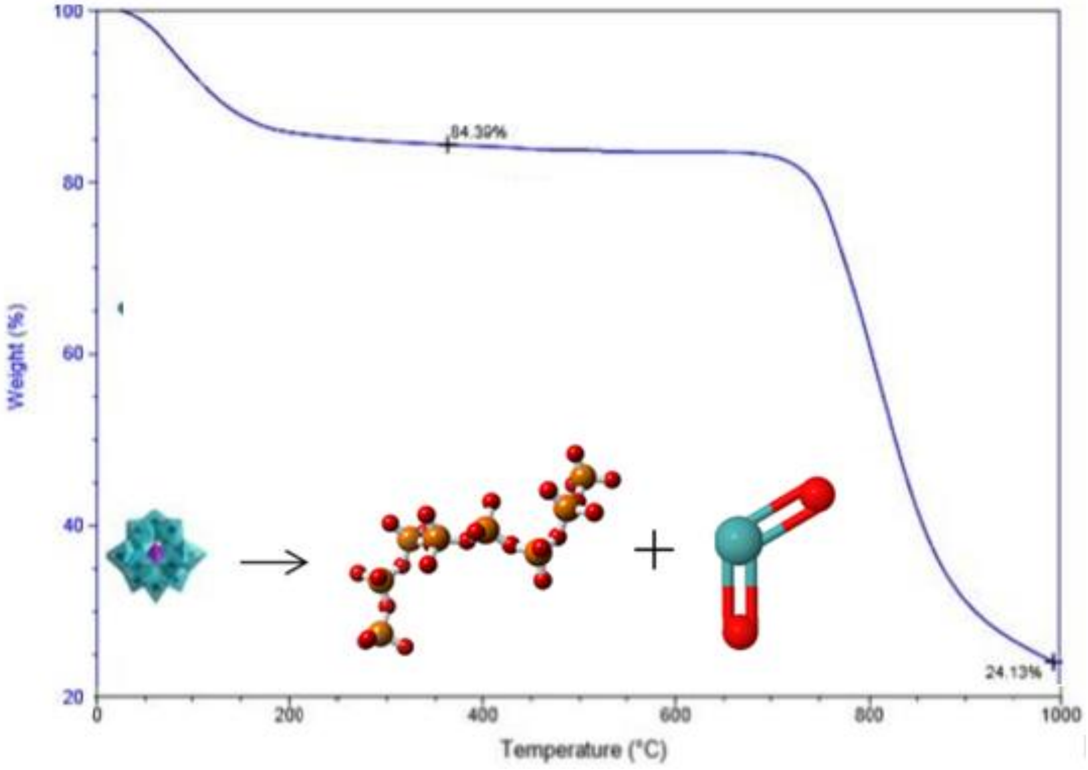

Figure 23. Thermogravimetric analysis of $K_3PW_{12}O_{40}$ showing mass losses at 25-50 and 400-1000 °C respectively

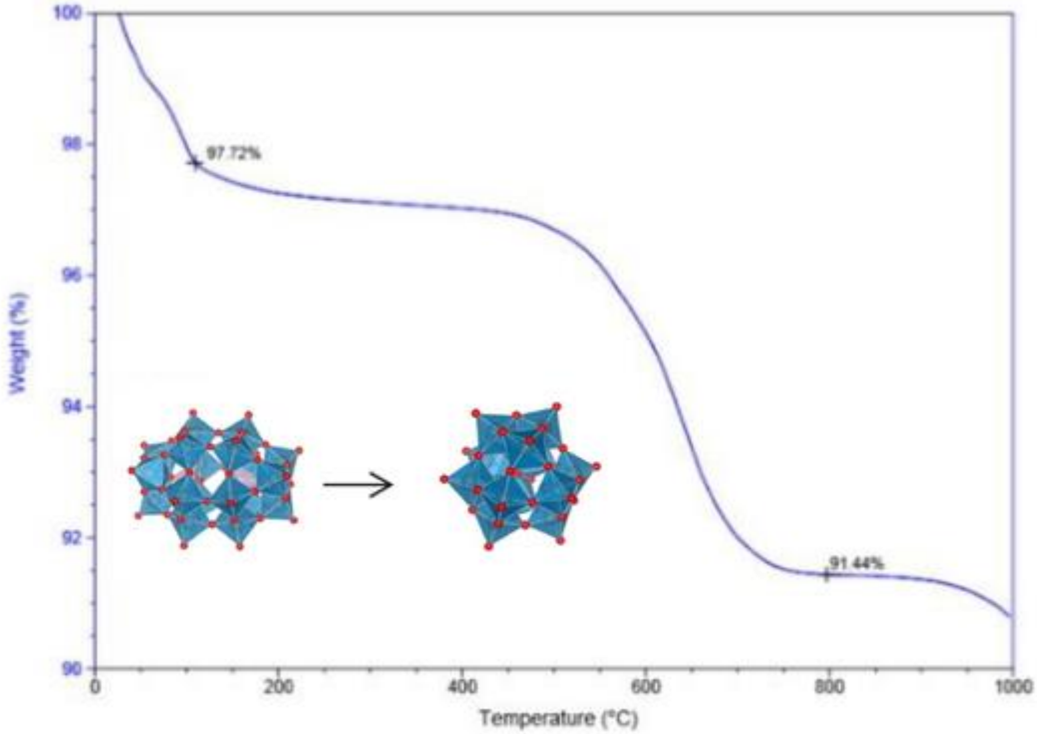

Figure 24. Thermogravimetric analysis of $K_6P_2Mo_{18}O_{62}$ showing mass losses at 25-50 and 400-1000 ^{O}C ***respectively***

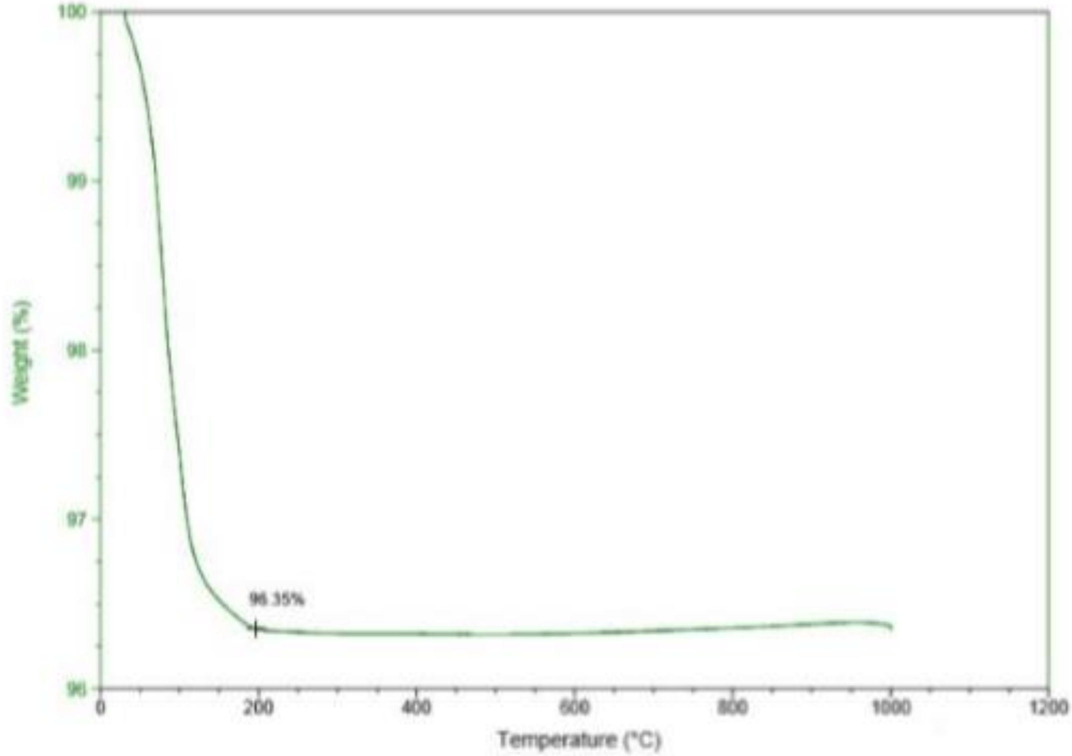

Figure 25. Thermogravimetric analysis of $K_6P_2W_{18}O_{62}$ showing mass losses at 25-50 and 400-1000 ^{O}C ***respectively***

4.1 Infrared of $K_3PMo_{12}O_{40}$/$K_6P_2Mo_{18}O_{62}$

Infrared spectroscopy is one of the most frequently employed techniques for the characterisation of polyoxometalates because of the characteristic peaks of their structures. Most of the characteristic bands of the Keggin anion are found in the HPA fingerprint region (1200-500 cm $^{-1}$). The IR spectra of bulk $K_6P_2Mo_{18}O_{62}$, $K_6P_2Mo_{18}O_{62}$, $K_3PMo_{12}O_{40}$ and $K_3PW_{12}O_{40}$ recorded in this work show bands characteristic of Keggin and Wells-Dawson anions in the region below 1200 cm^{-1} The IR spectrum of $K_3PMo_{12}O_{40}$ is shown below in **fig 26** which shows typical Keggin structure characteristic IR peaks. Keggin-type HPAs are formed via the assembly of three Mo_6 octahedra by edge-sharing oxygen atoms ($M{-}O_c{-}$ M) to form M_3O_{13} sets, which further condense by sharing corner oxygen atoms ($M{-}O_b{-}M$) around a central atom to form a cage. Each M_3O_{13} also presents three terminal oxygen atoms ($M{=}O_t$). The FTIR spectrum of $K_3PMo_{12}O_{40}$ is dominated by four characteristic peaks at 1051 cm^{-1} (ν_{as} P−O), 951 cm^{-1} (ν_{as} $Mo{=}O_t$), 877 cm^{-1} (ν_{as} $Mo{-}O_b{-}Mo$), and 741 cm^{-1} (ν_{as} $Mo{-}O_c{-}Mo$), these peaks are all in good agreement with previously published FTIR. The Keggin structure was preserved when the POM was calcined at 300 ^{O}C and 400 ^{O}C. However, at 300 ^{O}C IR peaks corresponding to MoO_3 were observed at (984 and 894 cm^{-1} respectively). The intensity of the MoO_3 characteristic peaks increased as the samples were calcined at 400-500 ^{O}C. Overall this means that the Keggin structure started to decompose at around 400 ^{O}C, hence the highest stability temperature of the $K_3PMo_{12}O_{40}$ polyoxometalate was around 390 ^{O}C.

The spectra of the phosphomolybdate Wells-Dawson acid $K_6P_2Mo_{18}O_{62}$ is shown below in **fig 27** which shows typical Wells-Dawson structure characteristic IR peaks. The structure of the Wells-Dawson $K_6P_2Mo_{18}O_{62}$ involves two half units of a central PO_4 tetrahedron surrounded by nine MO_6 (M=Mo) octahedra. Therefore, four kinds of oxygen atoms appear in the FT-IR. The first is due to $P{-}O_a$ in which the oxygen atom are connected to the molybdate atom. The second is $M{-}O_b{-}M$ oxygen bridges, (corner-sharing oxygen bridges between different M_3O_{13} groups), the third is $M{-}O_c{-}M$ oxygen bridges and the last is $M{-}O_d$ terminal oxygen atoms. Therefore, four characteristic bands of $K_6P_2Mo_{18}O_{62}$ were seen which were ν_{as} ($M{-}O_d$, 958, 968and 966 cm^{-1}); ν_{as} ($M{-}O_b{-}M$, 910, 915 and 917 cm^{-1}); ν_{as} ($M{-}O_c{-}M$, 778, 783 and 785 cm^{-1})

and v_{as} (P-O_a, 1080, 1091 and 1091cm^{-1}). The Wells-Dawson structure was preserved when the POM was heated to 300 and 400 ^{O}C respectively. At 500 ^{O}C, IR peaks corresponding to both the Keggin $K_3PMo_{12}O_{40}$ structure and MoO_3 were starting to be observed at around 984 and 894 cm^{-1} suggesting partial decomposition of the Wells-Dawson structure into its subsequent Keggin counterpart with further decomposition corresponding to a molybdenum oxide species. The intensity of the MoO_3 characteristic peaks increased as the samples were calcined past 400 ^{O}C respectively. This means that the Wells-Dawson structure was destroyed at 500 ^{O}C, hence the highest stability temperature of the Wells-Dawson $K_6P_2Mo_{18}O_{62}$ acid is 400 ^{O}C

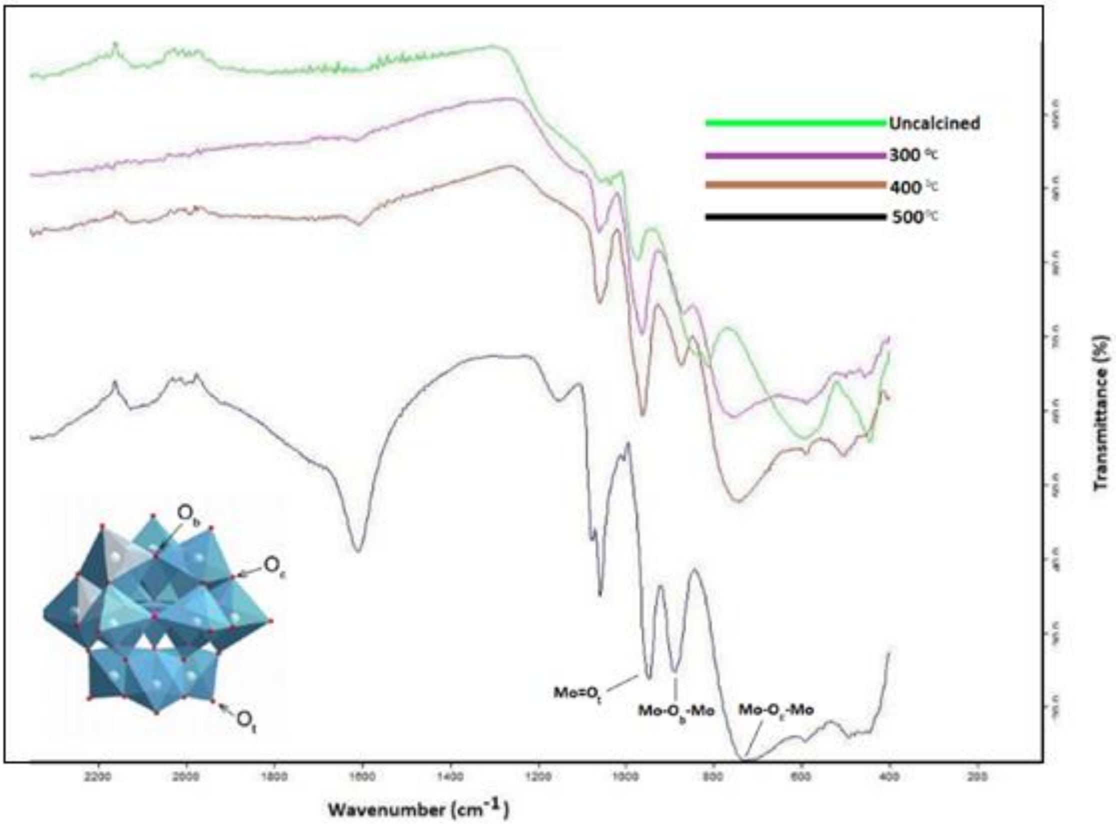

Figure 26. An infrared spectrum showing the uncalcined $K_3PMo_{12}O_{40}$ and Calcined $K_3PMO_{12}O_{40}$ at a) 300°C, b) 400°C and c) 500°C

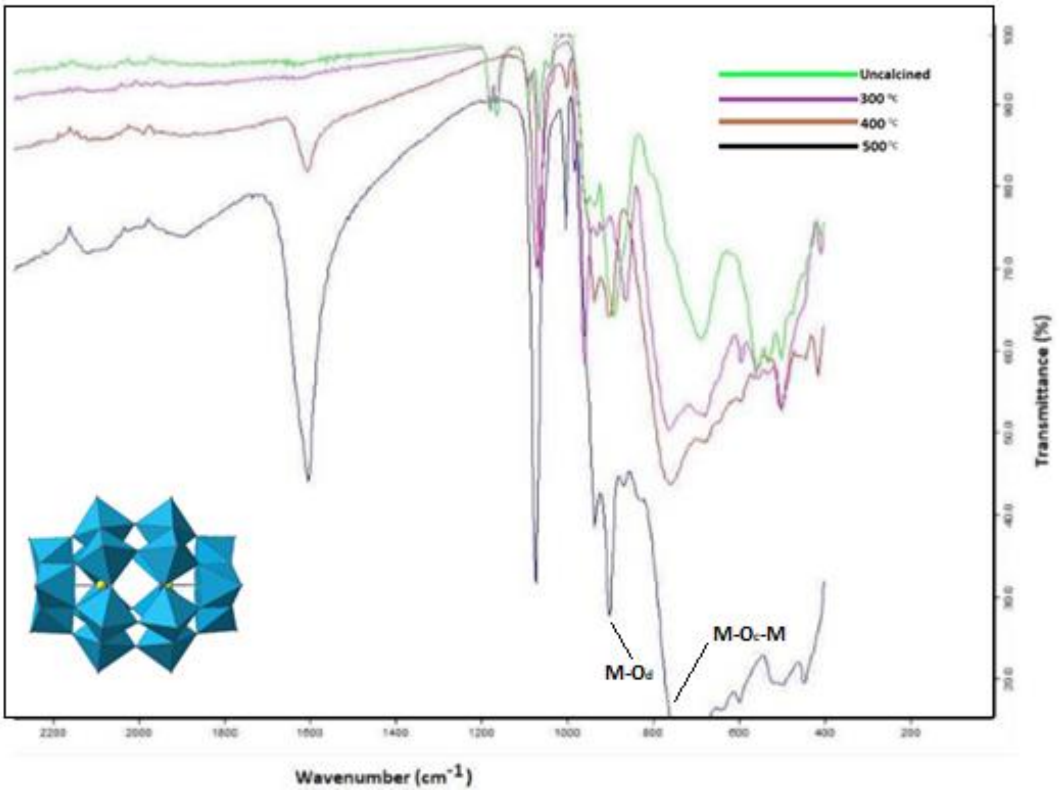

Figure 27. An infrared spectrum showing the uncalcined $K_6P_2Mo_{18}O_{62}$ and Calcined $K_6P_2Mo_{18}O_{62}$ at a) 300°C, b) 400°C and c) 500°C

4.2 Infrared of $K_3PW_{12}O_{40}/K_6P_2W_{18}O_{62}$

FTIR analysis has been used in previous studies to show the structural variations due to the nature of the heteroatom (X) and /or of the transition metal element (M). Valuable information was obtained regarding the assignment of the absorption frequency of the M=O, M-O-M, and X-O vibrations. Essayem et al. reported that the Keggin anion vibration bands of tungstophosphoric acid appeared at 1079 cm^{-1} due to (P-O$_a$)vibration, 975 cm^{-1} due to as the terminal v_{as} (W =O$_t$) vibration, 887 and 795 cm^{-1} assigned to v_{as}(W–O$_b$– W) and v_{as} (W–O$_c$–W), respectively. Weaker absorptions appeared at 596 and 525 cm^{-1} due to δ(O-P-O) and v_{as} (W–O–W), respectively. Figure 20 shows the FTIR spectra of $K_3PW_{12}O_{40}$ which shows that there is a progressive peak at (1611-1628) cm^{-1} upon calcination of the acid which suggests that this absorption is due to the same protonated water cluster in uncalcined samples.

IR bands of $K_3PW_{12}O_{40}$ **fig 28** recorded after thermal treatment of the sample at 300 and 400 ^{O}C the band at 776 cm^{-1} ascribed to v_{as} (W –O$_c$–W) or such vibration bands were not affected.

Moreover, the $v_{as}(W-O_c-W)$ band and $v_{as}(W-O_b-W)$ band were not affected. Overall It can be observed that the characteristic bonding absorptions of the anion, P–O , $v_{as}(W=O_t)$, $v_{as}(W-O_c-W)$ and $v_{as}(W-O_b-W)$ were obtained for all samples, providing evidence that no apparent decomposition of the primary Keggin structure has occurred after thermal treatment. This may be related to higher thermal stability of potassium salts coupled with the high thermal stability of tungsten compared to molybdenum species.

A fingerprint of the Wells-Dawson heteropoly anion $P_2W_{18}O_{62}^{6-}$ structure **fig 29**. The bands at 960, 914 and 783 cm^{-1} correspond to the W-O species of the cage structure surrounding the central phosphorous species. Looking at Figure 21 it can be shown that the characteristic bonding absorptions of the anion obtained for all samples uncalcined and calcined alike suggests that no apparent decomposition of the primary Wells-Dawson structure had occurred after thermal treatment. This is further proof from the TGA analysis from earlier.

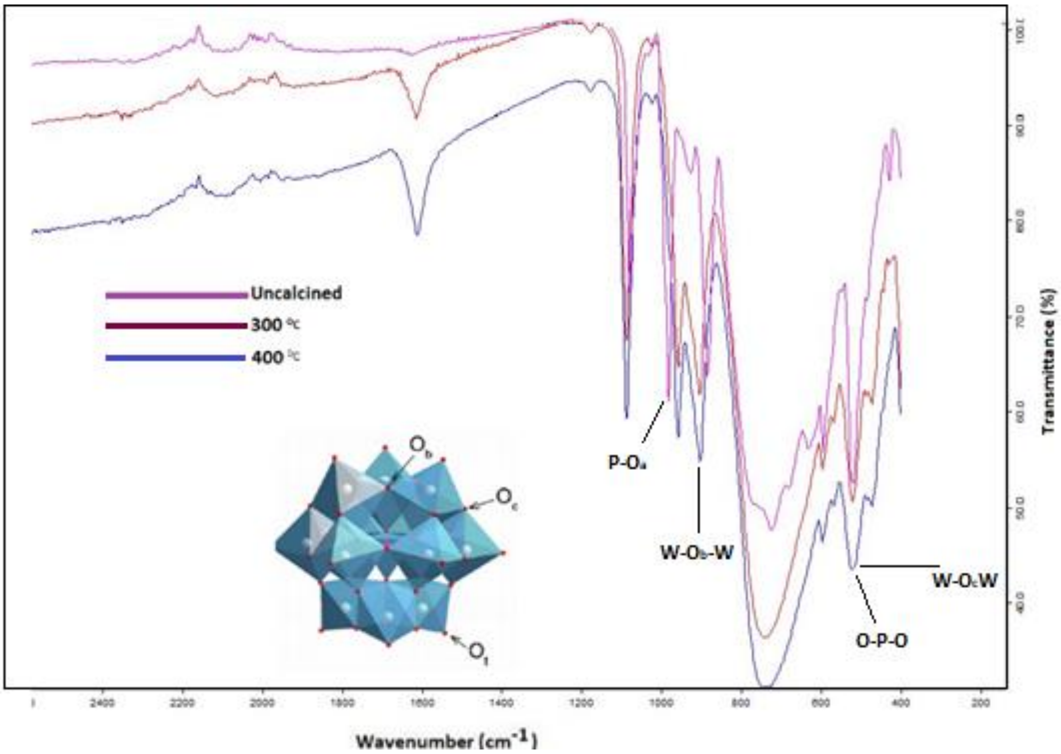

Figure 28. An infrared spectrum showing the uncalcined $K_3PW_{12}O_{40}$ and Calcined $K_3PW_{12}O_{40}$ at a) 300°C, b) 400 °C and c) 500 °C

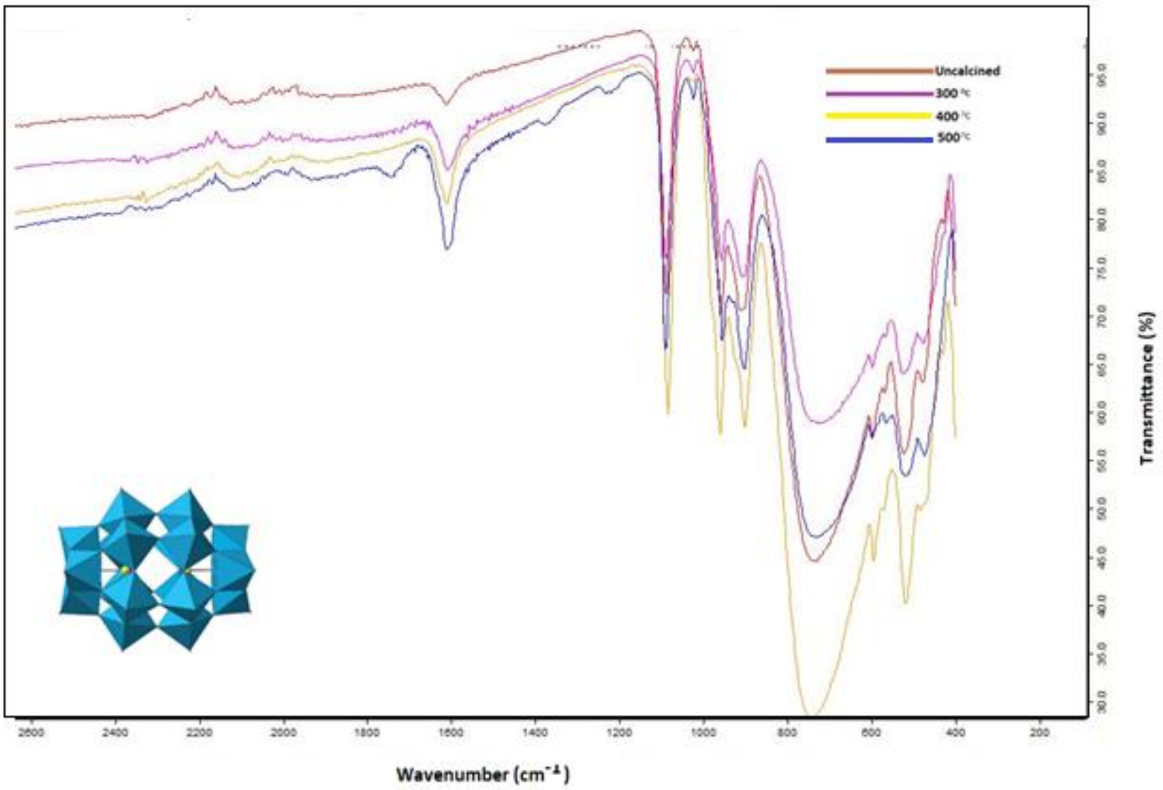

Figure 29. An infrared spectrum showing the uncalcined $K_6P_2W_{18}O_{62}$ and Calcined $K_6P_2W_{18}O_{62}$ at a) 300°C, b) 400 °C and c) 500 °C

4.3 PXRD of $K_3PMo_{12}O_{40}/K_6P_2Mo_{18}O_{62}$

The thermal transformation of $K_3PMo_{12}O_{40}$ from its hydrated form ($K_3PMo_{12}O_{40}.17H_2O$) through its intermediates (anhydrous acid $K_3PMo_{12}O_{40}$ and anhydride $K_xPMo_{12}O_{38.5}$) and to its final decomposition products; molybdenum trioxide MoO_2 and phosphorous P has been suggested and shown from previous in-situ PXRD studies. The PXRD peaks of the uncalcined $K_3PMo_{12}O_{40}$ **fig 30** is similar to the characteristic peaks of the monoclinic Keggin structure. However, a complete change in the PXRD pattern was observed when the catalyst was calcined at 500 ^{O}C. This change resulted in the formation of an unidentified phase, which is thought to be microcrystalline or amorphous in origin. The nature of this phase is highly dependent on the level of hydration (Waters of crystallisation) hence making it extremely difficult to study the crystallographic nature of this partially dehydrated material. However, images taken during transmission electron microscopy showed that this material was semi crystalline. When the catalyst was calcined at 500 ^{O}C, peaks belonging to MoO_2 and an unknown phase were observed. The calcined sample clearly shows peaks with d spacing of (40° and 60°) which correspond to MoO_2 peaks. It was also observed that the solubility in water of this mixture of phases, had dropped, which was due to the formation of a less soluble MoO_2 decomposition product. It was also observed from the IR result that the 300 ^{O}C calcined sample had Keggin characteristic peaks, whereas the 400 ^{O}C sample had MoO_2 characteristic peaks. This means that the unidentified phase in the XRD of the 300 ^{O}C calcined sample has a Keggin structure which dominated up until 380 ^{O}C however at 400 ^{O}C the MoO_2 structure dominates.

Fig 31 shows a comparison between the powder XRD pattern of pure hydrated $K_6P_2Mo_{18}O_{62}$ and $K_6P_2Mo_{18}O_{62}$ calcined at 500 ^{O}C. The structure of the Wells Dawson $K_6P_2Mo_{18}O_{62}$ revealed quite a crystalline material, which can be distinguished by multiple sharp peaks present in the PXRD spectra (2θ=24.4° and 25.6°). On the non-calcined sample, a peak clearly corresponding to $K_6P_2Mo_{18}O_{62}$ can be seen at 28.5°, however upon calcination to 500 ^{O}C the peak has shifted to the right to around 29.5° which is indictive of composition change due to increasing lattice strain on the material. However, from previous research we know that this decomposition results in the formation of $K_3PMo_{12}O_{40}$ due to $K_6P_2Mo_{18}O_{62}$ extreme instability at higher temperatures. It can also be seen that MoO_3 was formed via this calcination as peaks corresponding to the crystal phases of [020], [220], [031] and [231] of MoO_3 were seen at peaks 37.1 °, 53.6 °, 60.8 ° and 66.7 ° respectively. This indicates that upon calcination to 500 ^{O}C the decomposition products are more favoured over the POM structure and the original Keggin structure has almost completely decomposed.

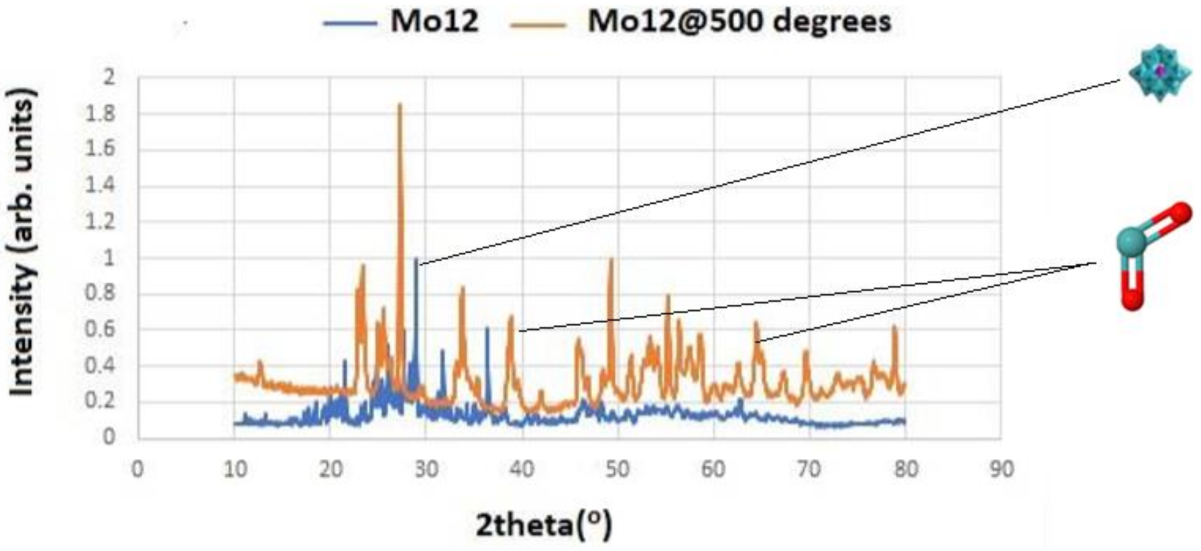

Figure 30. PXRD spectra comparing that of $K_3PMO_{12}O_{40}$ to $K_3PMO_{12}O_{40}$ calcined at 500^OC

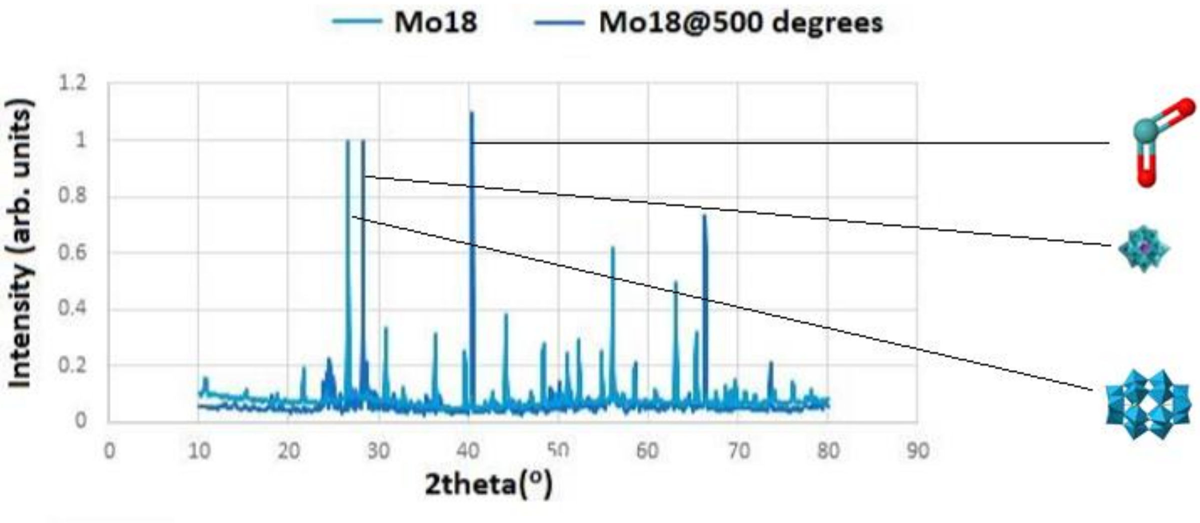

Figure 31. PXRD spectra comparing that of $K_6P_2MO_{18}O_{62}$ to $K_6P_2MO_{18}O_{62}$ calcined at

4.4 PXRD of $K_3PW_{12}O_{40}$/$K_6P_2W_{18}O_{62}$

The powder X-ray diffraction patterns of $K_3PW_{12}O_{40}$ **fig 32** suggest that the material was crystalline in nature. The XRD pattern of $K_3PW_{12}O_{40}$ show sharp diffraction peaks around 10.2°, 20.6°, 25.2° and 34.7° which corresponds to the Keggin anion. The calcination hardly changed the XRD patterns of the $K_3PW_{12}O_{40}$, except that their intensities increased, and the line widths became narrower, which is consistent with the surface area analysis and the IR spectra previously established.

Figure 33 shows X-ray diffraction patterns of fresh $K_6P_2W_{18}O_{62}$ and $K_6P_2W_{18}O_{62}$ calcined at 500. Figure 24 shows two signals at 24, 26 and 32◦, which coincide with those reported for the isomer of the $K_6P_2W_{18}O_{62}\cdot 10H_2O$ Dawson-type heteropolyoxoanion. No modifications in the positions of the signals are observed at 300 and 400^{O}C suggesting that, unlike in other heteropolyoxoanions, the secondary structure of these Dawson heteropoly salts do not change after losing the water of crystallization. However, an increase in the background and intensity loss is observed in the XRD spectra of the samples calcined at 500^{O}C. Previous studies reported a similar effect in the XRD diffract grams of Keggin and Dawson acids upon calcination at 250–400^{O}C and 300–600^{O}C, respectively. The authors attributed the phenomena to the electrostatic repulsion of the dehydrated anions, causing a disorder of the secondary structure.

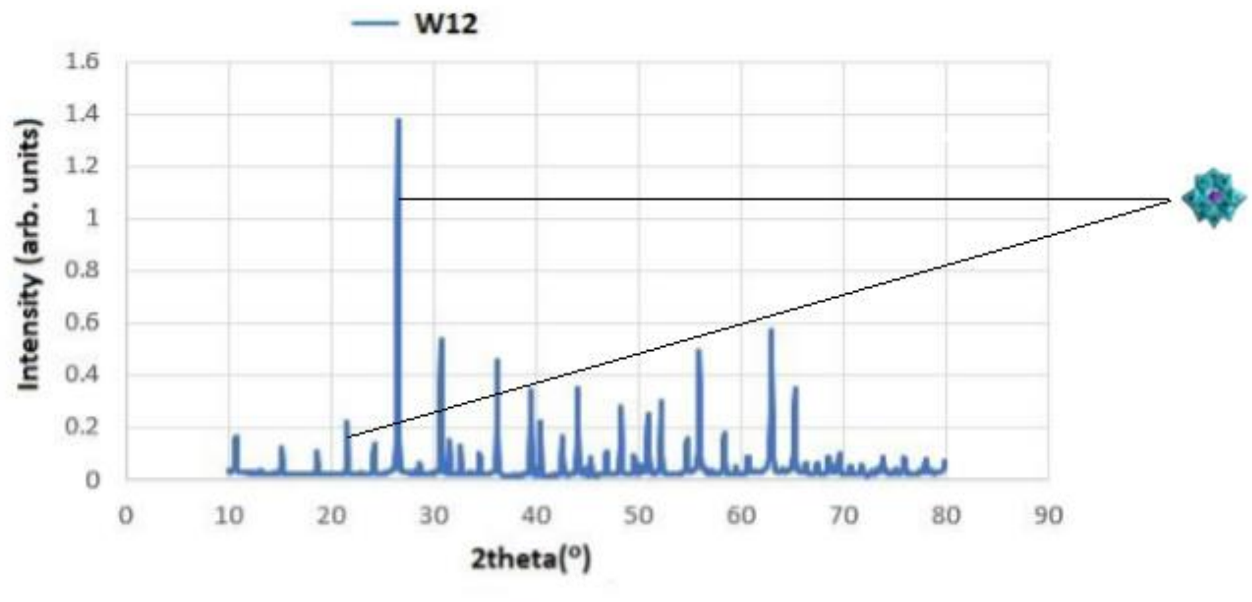

Figure 32. PXRD spectra of $K_3PW_{12}O_{40}$ polyoxometalate

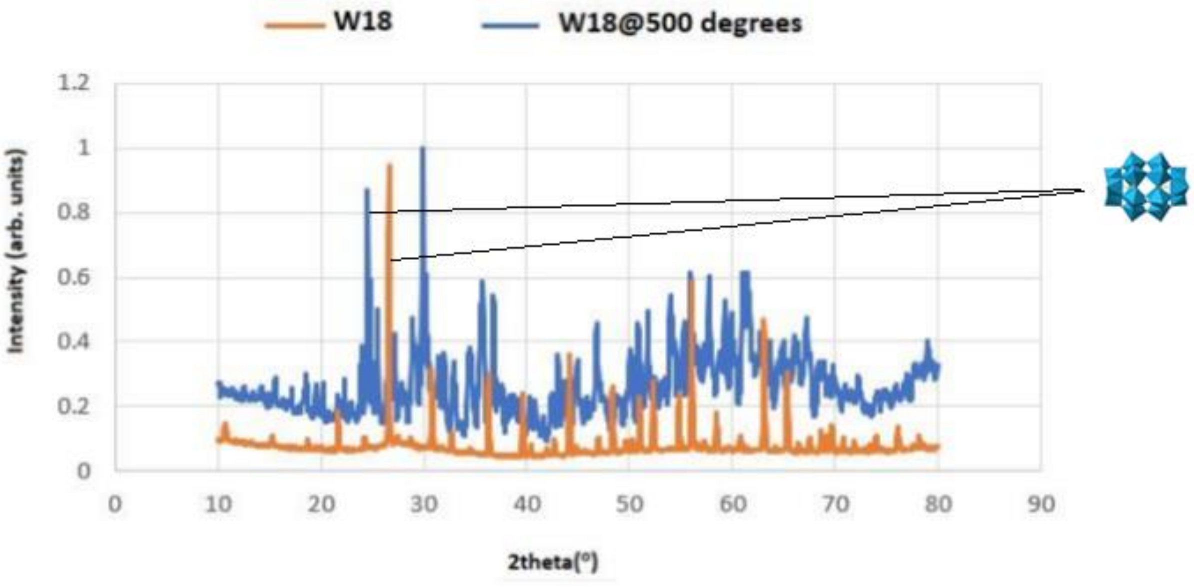

Figure 33. PXRD spectra comparing that of $K_6P_2W_{18}O_{62}$ to $K_6P_2W_{18}O_{62}$ calcined at

4.5 Thermal stability of Polyoxometalates

Overall in general, polyoxometalates are well known for their redox and photo/electro active properties, as well as their relative stability. The thermal stability of heteropoly compounds is of great importance for their use in catalysis. Some compounds are stable and can be applied as catalysts at moderately high temperatures, up to 400-450 ^{O}C. The thermal stability, however, may not be enough for catalyst regeneration. Thermal decomposition of polyoxometalates → metal oxide is a complex multistep process. The catalyst activity may be lost at an early stage of decomposition. For example, solid acid catalysts e.g $H_3PW_{12}O_{40}$ lose their activity at the onset of thermal decomposition of the keggin structure, when the acid protons are lost well before the formation of WO_3 and P_2O_5 is complete. A great deal of caution should be exempted when comparing the thermal stabilities from different sources. The decomposition temperatures are subject to many parameters such as the heating rate, amount of sample, shape of crucible, the purity of the sample, it is also possible that decomposition on the surface of the sample may occur at lower temperatures than in bulk.

Generally, Wells-Dawson Tungsten compounds are the most stable among polyoxometalates. The order of stability is shown below;

$$\mathbf{K_6P_2W_{18}O_{62} > K_3PW_{12}O_{40} > > K_3PMo_{12}O_{40} > K_6P_2MO_{18}O_{62}}$$

Thermal stability is usually determined by thermal analytic methods such as TGA and frequently in combination with other techniques, such as X-ray diffraction, infrared and NMR. However, Tsigdinos introduced a relatively simple method that allows estimation of thermal stability of polyoxometalates. This method includes heat treatment followed by a solubility test. If after heating, the compound is soluble in water its structure is deemed to remain intact, otherwise the structure has decomposed.

Polyoxometalates undergo dehydration by losing the water of crystallisation, when thermally treated at 100 ^{O}C. This process is followed by the structural decomposition (loss of constitutional water), which occurs at 350-600 ^{O}C. In the case of the $K_6PMo_{12}O_{40}$ catalyst, the Keggin structure is destroyed above 450 ^{O}C and the decomposition leads to the formation of a less active molybdenum trioxide and phosphorus peroxide products which can be seen in the equation below.

$$\mathbf{H_3PMo_{12}O_{40} \rightarrow ½\ P_2O_5 + 12MoO_3 + 3/2\ H_2O}$$

The thermal stability of the polyoxometalates depends on the heteroatom, polyanions and the polyanion structure. Compounds containing phosphorous as a central atom are more thermally stable than those contain silicon as such, and compounds having tungsten as an addenda atom are more stable than those contain molybdenum containing compounds. The keggin type $K_6PW_{12}O_{40}.14H_2O$ and $K_6PMo_{12}O_{40}.14H_2O$ start to decompose at around 456 and 375 ^{O}C respectively as can be seen in the TGA and FTIR above.

It is well known that the less stable compounds start to decompose at lower temperatures when heated. It was therefore discovered that at lower temperatures, before the formation of crystalline MoO_3, compounds such as PMo_{12} start to partially disintegrate to form isopolymolybdates and PMo_{12}-x lacunary structures by expelling molybednyl species from the Keggin structure in which a MoO_3 lattice formed from the isolated molecules of POMs, then the rearrangement of Keggin anions, followed by the reorganisation and condensation of MoO_3 had to occur. The structural and thermal instability of POMs is still the major drawback of using POMs especially in high temperature catalysis reactions. Although it may be argued that the defined POM structure can in fact be stabilised via the method of encapsulation in which GNFs provide. These GNFs could in fact shield POMs from these high temperature decompositions whilst providing thermally stable catalysts.

4.6 POM@GNF Characterisation

Whilst other forms of carbon nanotubes such as SWNTs have many beneficial properties, such as facile guest-host electron transfer and a low level of light absorption through the single graphitic layer, there can be mass transport problems due to their narrow diameter. The narrow diameter of the interior dimension can make the diffusion pathway of larger molecules significantly problematic which in turn limits reaction rates. GNFs provide a much larger internal channel which ranges between 50-100nm, which removes the aspect of mass transport issues associates with SWCNTs, MWCNTs and DWCNTs. Additionally, GNFs have an increased surface area compared to these other forms carbon as the stacks of graphitic layers within the internal dimension provide many sites for POM molecules to adsorb to. For these reasons, it was decided to load the selected POMs within the interior of GNF. Additionally, this study allows study into the feasibility of POM loading onto other forms of nanotubes. POM@GNF was synthesised via a liquid filling method whereby GNFs are added to an aqueous solution of POMs **figure 34.**

4.7 GNF shortening via Ball Milling

In order to encapsulate POMs inside hollow nanostructured GNFs and to perform chemical reactions in a confined space, the diameter and length of the GNF must be suitable for easy transport of reactants and products to and from its internal cavity. Smaller diameters with a greater length of GNF slows the diffusion rate and as a result the rate of chemical reaction becomes reduced. Overall cutting the length of the carbon nanotubes is essential to meet the demand for short nanoreactors. There are several different methods for cutting carbon nanotubes, for example; mechanical methods such as ball milling and oxidative methods using reagents, such as nitric acid, mixture of nitric and sulphuric acid, potassium permanganate, or using catalytic metal and metal oxide nanoparticles, such as nickel oxide, iron and silver nanoparticles. Among these methods, ball milling is the cleanest process that effectively controls the length of carbon nanotubes without posing a significant damage to the structure. The overall effectiveness of this method for making short length nanotubes has been demonstrated. Therefore, in this work graphitised carbon nano fibres (PR-19) were subjected to both ball milling to reduce their length and these results were compared to non-ball milled GNFs **figure 35.**

Figure 34. A schematic representation of POM filling within a GNF.

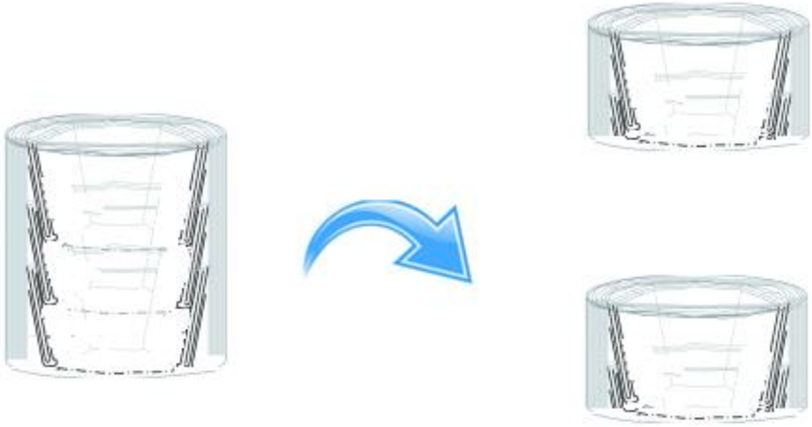

Figure 35. A schematic representation of Ball milling of GNFs to achieve shorter

4.8 Method of preparation of POMs inside graphitised carbon nanofibers.

For the performance of the tungsten/molybdate Wells-Dawson/Keggin GNF hybrids to be evaluated via electrochemistry or catalysis a successful synthesis first needs to be completed. Previous research within the group developed a suitable liquid-phase filling synthesis to produce composite materials of (M_nO_x) based carbon nano reactors. Due to the POMs ease of solubility in water and their ability to recrystallize rather easily this filling method appeared to be a suitable method to synthesise the desired POM composites.

Two concentrations of $K_6P_2W_{18}O_{62}$/$K_6P_2Mo_{18}O_{62}$@GNF were made up one at higher concentration (0.01M) and one at low concentration (0.05M). Whist this was possible for both Wells-Dawson POMs, the Keggin POMs proved too unstable for an increased concentration whilst loading. Upon the addition of $K_6P_2W_{18}O_{62}$/ $K_3PW_{12}O_{40}$ POMs to GNFs, there was a colour change seen from a clear solution to a milky white, indicating a colloidal suspension had formed. This indicated that GNFs were less easily oxidised than other forms of carbon nanotubes. This suggests that the C^+ may not form, indicating that electrostatic interactions may not be the forces at work leading to POM loading inside the GNF. As with most carbon nanomaterials, the W18@GNF samples were analysed via TGA, PXRD and TEM and EDX to determine if the POMs had become encapsulated or not. $K_6MO_{18}P_2O_{62}$ and water were taken in a 1:10 molar ratio and stirred together until dissolved. Upon the addition of the lower concentration of $K_6P_2Mo_{18}O_{62}$ a colour change from yellow to dark green had occurred, indicating partial reduction of the molybdate POMs. It was also noted that, at the higher concentration of Mo18 on addition of the GNFs, the yellow solution became dark green, indicating that POMs in solution had become reduced, to so called heteropoly blues. As mentioned previously, the redox properties of POMs are well known, with the species able to both acts as a reducing agent and an oxidising agent. Additionally, this observation of the reduced POMs in solution indicates that upon addition to the solution, GNFs are oxidised. This redox process occurs when the POMs meet the sp2 carbon atoms from the walls of the GNF and the POMs then re-enter solution. We can think of the charges of the separate species as such: positively charged GNFs and negatively charged POMs. This can be summarised as such:

Having two oppositely charged species in proximity of one another would lead to strongly attractive electrostatic interactions between the two. GNFs present a better opportunity of encapsulating the material within the interior than loading material onto the exterior due to their high curvature and greater interior surface area especially at the internal step edges (Eenc > Eabs). This effect, when couple with the strong, attractive electrostatic interactions between the species, leads to the POMs become encapsulated within the GNF giving $K_6P_2Mo_{18}O_{62}$@GNF

4.9 Thermogravimetric analysis (TGA) of $K_6P_2W_{18}O_{62}/K_3PW_{12}O_{40}$@GNF And $K_6P_2Mo_{18}O_{62}/K_3PMo_{12}O_{40}$ hybrids

To ascertain the loading of both $K_6P_2W_{18}O_{62}/K_3PW_{12}O_{40}$ into their respective GNF nanocomposites and to study their thermal stability, thermogravimetric analysis was carried out. **Fig 36** depicts thermogravimetric curves of both GNF, $K_6P_2W_{18}O_{62}/K_3PW_{12}O_{40}$@GNF with different concentrations of precursor. As seen, the total weight loss for both $K_6P_2W_{18}O_{62}/K_3PW_{12}O_{40}$@GNF occurred from 25 to 1000^{o}C and was found to be around 89% and 14% respectively. This weight loss corresponds to carbon gasification due to the combustion of the GNF in which the residual mass left beyond 600^{o}C corresponds to the loading percentage of both composites. It can be shown that for $K_6P_2W_{18}O_{62}$@GNF that an increase in residual mass of the sample is in good agreement with the increase in amount of precursor, however for $K_3PW_{12}O_{40}$ loading at this concentration was impossible due to stability effects. The $K_6P_2W_{18}O_{62}$@GNF nanocomposite starts to combust at around 670^{O}C which is lower than that of the combustion temperature of pure GNF 700 ^{O}C. This is due to the catalytic effects of $K_6P_2W_{18}O_{62}$ imposed on the GNF which exhilarates its combustion in air. This is a consequence of noncovalent interaction between W18 nanoparticles and the GNF, in which W18 coordinates to π bonds (C=C) of the GNF. As a result of this coordination C=C bonds become weakened and thus the GNF combusts at a lower temperature. This phenom can be explained using the Chatt-Duncanson Model. The model dictates that a simga-type donation from the C=C π orbital of the GNF into an empty d-orbital of the POM species whilst subsequently π back-donation from a filled d-orbitial of the POM species into an empty C=C π star orbital of the GNF. The greater the electron density back-donated into the p* anti-bonding orbital of the GNFs, and the greater the electron density donated from the filled p bonding orbital, the lower the bond order and hence the weaker the C=C bonds in the GNF become, leading to cleavage at lower temperatures. Additionally, the greater the p-backbonding from the filled d orbital, the more electron deficient the molybdenum becomes, leading to an increase in Lewis acidity, which can improve the ability of the metal centre to act as an oxidising agent.

It was shown that compared to $K_6P_2W_{18}O_{62}$, the $K_3PW_{12}O_{40}$@GNF composite combusted at around the same temperature as pure GNF, which suggests C=C bond coordination within this structure is not significantly weekend. It was shown that a one-step decomposition of both $K_6P_2W_{18}O_{62}$/$K_3PW_{12}O_{40}$@GNF nanocomposites occurred, this suggests that uniform oxidation within the nanocomposite occurred, which was attributed to the formation of stable tungstate nanocomposites instead of two separate entities. The loading was determined to be around 0.029% wt.

Looking at the $K_6P_2Mo_{18}O_{62}$ graph in **fig 36**, it can be seen that the (0.005M) solution has around a 1.813% wt and the (0.01M) solution has a loading of around 51.96% which is an increase of around 2700 times. This weight increase could be attributed to possible agglomeration or possibly heavier dense decomposition products such as MoO_2 which have adsorbed onto the sides of the GNFs outer wall. Overall in both samples the POM combustion temperatures are significantly lower than the decomposition of the carbon GNF further indicating significant interactions between the GNF and the POM species that are either encapsulated within the GNF or adsorbed onto the external surfaces, which in fact suggests a composite has formed.

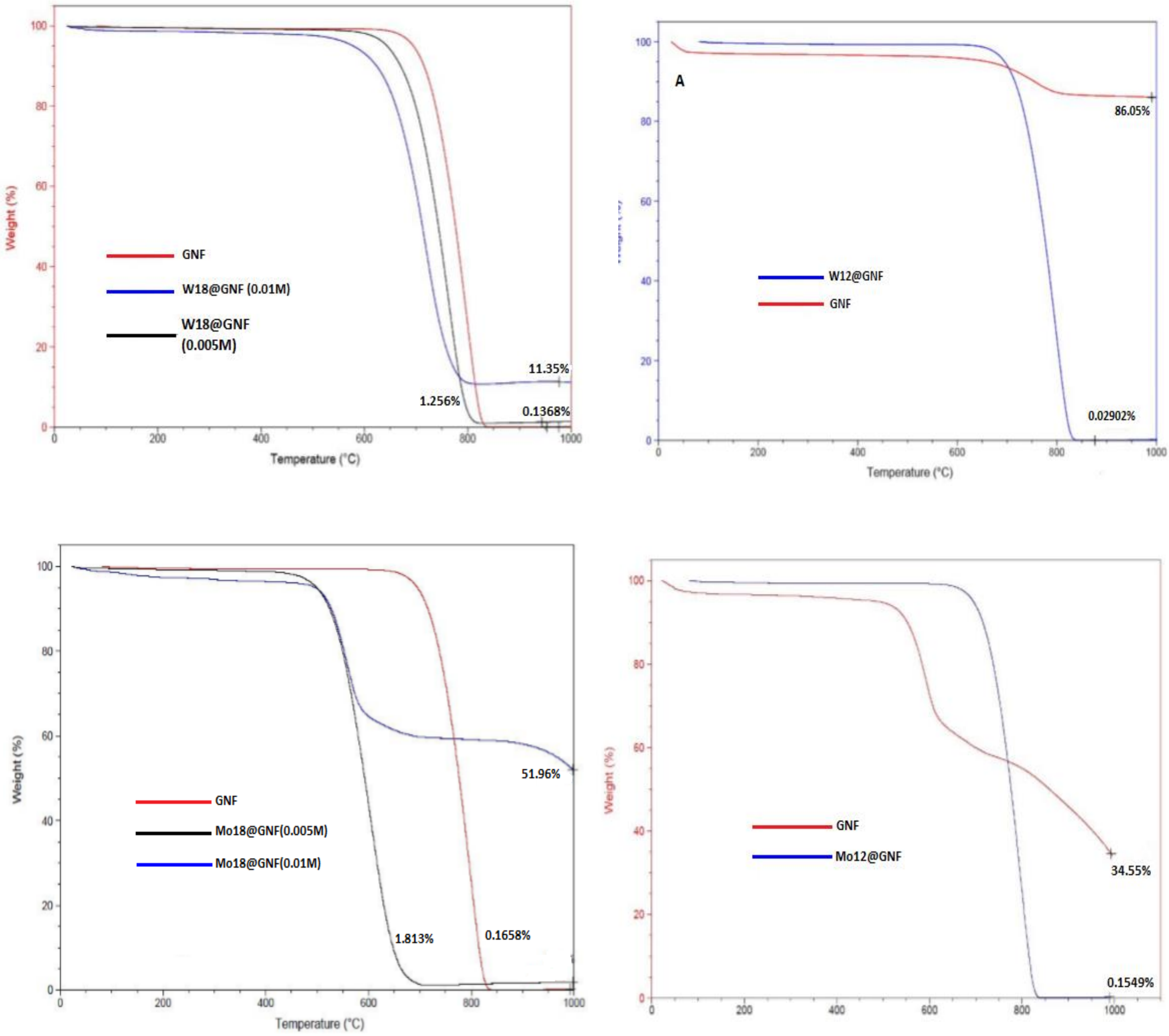

Figure 36. TGA curves of $K_6P_2W_{18}O_{62}$/$K_3PW_{12}O_{40}$@GNF And $K_6P_2Mo_{18}O_{62}$/ $K_3PMo_{12}O_{40}$ hybrids

5.0 PXRD of POM@GNF nanocomposites

Although TGA has provided evidence that successful loading of the synthesised POMs has been achieved, this technique is unable to provide confirmation regarding the crystallinity or oxidation state of the produced POM composites. Powder X-ray diffraction (PXRD) is a widely used technique which can determine information, regarding crystal structure of the encapsulated POM species and hence further prove if encapsulation has taken place. The PXRD patterns collected shows clear evidence for the presence of POMs in the composite materials, due to additional peaks being present when compared to the pattern obtained for the GNF on its own.

PXRD analysis was used to confirm the formation of $K_6W_{18}O_{62}$@GNF. The PXRD pattern of pure GNF, $K_6P_2W_{18}O_{62}$@GNF and $K_6P_2W_{18}O_{62}$ are shown in **fig 37** All of the diffraction peaks agree with standard literature amounts. Only the widths and diffraction peaks intensities demonstrated some changes, confirming the successful synthesis and purity of $K_6P_2W_{18}O_{62}$@GNF

The XRD patterns of the samples are indicated below, which show almost no difference among the pure W18 with the W18@GNF hybrid, the only difference seems to be that impurities have been washed away during the loading step of the W18 into the GNF. Consequently, the XRD patterns of Pure GNF, W18@GNF and W18 mainly resemble each other, which indicated that the crystalline structure of W18 was preserved after loading. The lower intensities of the diffraction peaks of $P_2W_{18}O_{62}$ in the nanohybrid were probably due to the uniform distribution of the $P_2W_{18}O_{62}$ within the Porous GNF. The low intensity of W18 in the hybrid could also be due to the low amount of W18 within the hybrid, which was further evidenced via TGA analysis, which showed around a 3% loading. Moreover, the XRD pattern together with FT-IR spectra demonstrated that the introduction of $P_2W_{18}O_{62}$ within the structure of the GNF did not lead to collapse/destruction of the framework.

Fig 38 shows PXRD patterns of $K_6P_2W_{18}O_{62}$@GNF and pure GNF. Short scan PXRD patterns reveal GNF is integrated part in all three materials. The diffraction peaks of GNF at 2θ = 26° , 42.4° , 44.6° , 54.4° and 77.4° correspond to (002), (100), (101), (104) and (110) planes of graphitic lattice and are unchanged in the $K_6P_2W_{18}O_{62}$@GNF composite. The pattern produced by the $K_6P_2W_{18}O_{62}$ nanocomposite contains additional peaks at 2θ= 29.2 ° confirming the presence of discrete $K_6P_2W_{18}O_{62}$ nanoparticles rather than decomposition products. For $K_6P_2W_{18}O_{62}$@GNF the crystallite size of the POM particles was calculated via the full width half maximum (FWHM) of the (311) peak at 2θ= 29.2 ° using Scherrer's equation which it outlined below:

$D = K\lambda/B \cos\theta$

D is the average crystallite size, λ is the wavelength of the x-ray radiation used and K is the constant taken 0.9, θ is the diffraction angle and B is the full width of the diffraction line at half the maximum intensity, measured in radian.

Overall the mean average size was found to be 1.16 nm.

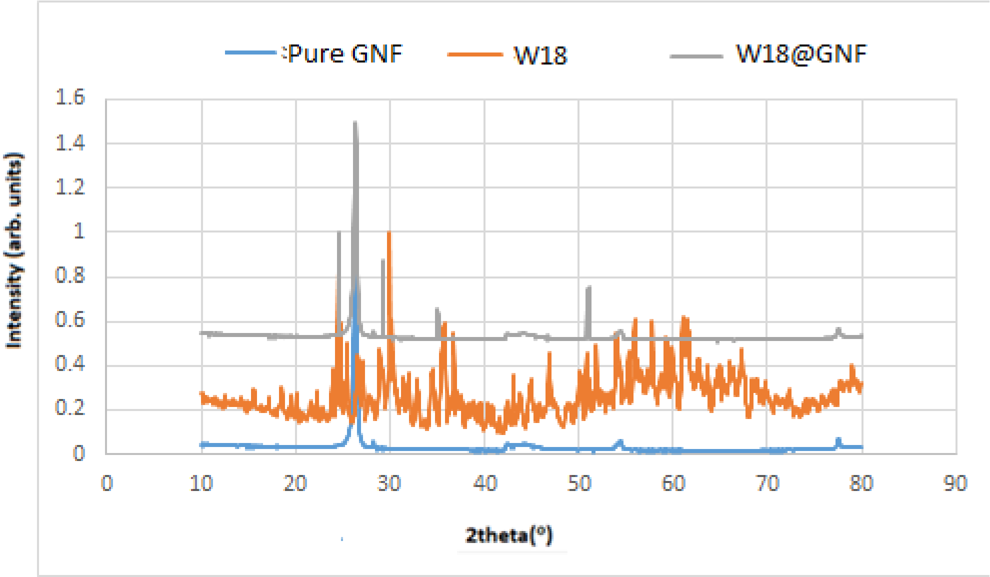

Figure 37. PXRD of Pure GNF, W18 and W18@GNF

The PXRD patterns of $K_3PW_{12}O_{40}$, $K_3PW_{12}O_{40}$@GNF and GNF are also shown in **Fig 39**. It can be seen that the $K_3PW_{12}O_{40}$@GNF sample has two narrow weak peaks at 35-50°, which are attributed to the (002) and (101) faces of amorphous carbon which were also seen in the above $K_3PW_{12}O_{40}$@GNF sample, this indicates that the catalysts are composed of amorphous carbon with a low degree of graphitization. Some reflections appeared at 2θ values = 16.2°, 23.7°, 26.1°, 30.2°, which are assigned to the characteristics of $K_3PW_{12}O_{40}$. It can also be noted that there were no decomposition peaks indicating that the Keggin structure retained its structure during the synthesis of the hybrid catalyst. Hence, it can be concluded that the $K_3PW_{12}O_{40}$ has been successfully supported on the encapsulation of the GNF. Using Scherrer's equation which it outlined below:

$D = K\lambda/B \cos\theta$

D is the average crystallite size, λ is the wavelength of the x-ray radiation used and K is the constant taken 0.9, θ is the diffraction angle and B is the full width of the diffraction line at half the maximum intensity, measured in radian.

Overall the mean average size was found to be around 3 nm.

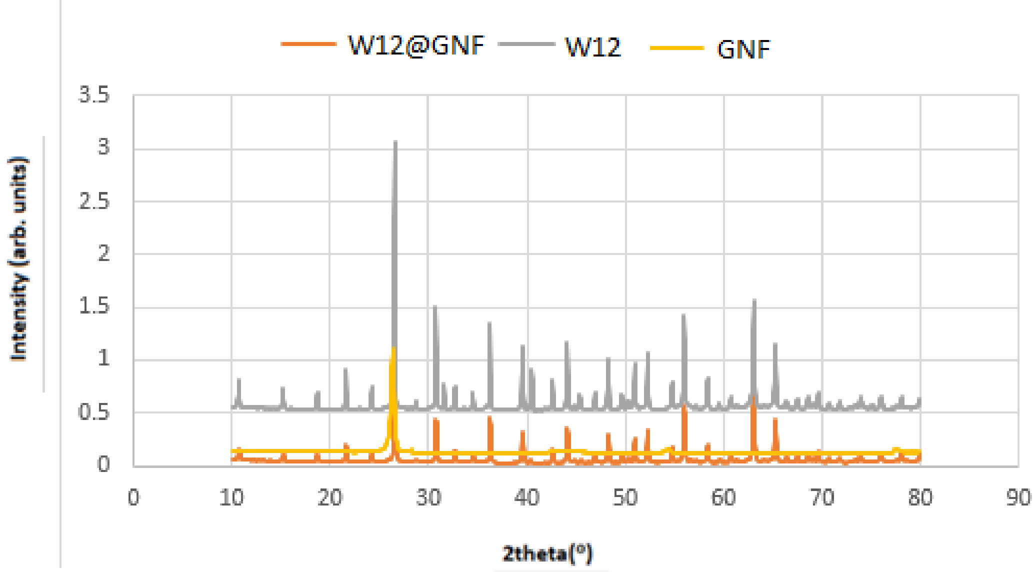

Figure 38. PXRD of Pure GNF, W12 and W12@GNF

Figure 40 shows XRD patterns of $K_3PMo_{12}O_{40}$@GNF (0.005M), and $K_3PMo_{12}O_{40}$ and GNF. Short scan (4 hours with a slow scanning rate was used to obtain the spectra) XRD patterns show intense peaks at 2θ = (26.4 °), which corresponds to [002] crystallographic planes of the GNF, furthermore less intense peaks are present at 2θ values of 67 °, 58 ° and 73 ° respectively. The pattern produced by the pure $K_3PMo_{12}O_{40}$ POM produces several peaks seen at 2θ = (24, 27 °, 28 °, 31 ° and 36 °) respectively. It is shown below that the pattern produced by the $K_3PMo_{12}O_{40}$ composite, not only has characteristic POM peaks at 2θ = (31 °,36 °) but also shows a multitude of molybdenum oxide peaks at 2θ = (40 ° and 66.7 °) suggesting that due to the confinement effects of insertion into the GNF, the keggin structure has decomposed into subsequent MoO_3. Using Scherrer's equation which it outlined below:

$D = K\lambda/B \cos\theta$

D is the average crystallite size, λ is the wavelength of the x-ray radiation used and K is the constant taken 0.9, θ is the diffraction angle and B is the full width of the diffraction line at half the maximum intensity, measured in radian.

Overall the mean average size was found to be around 0.8 nm.

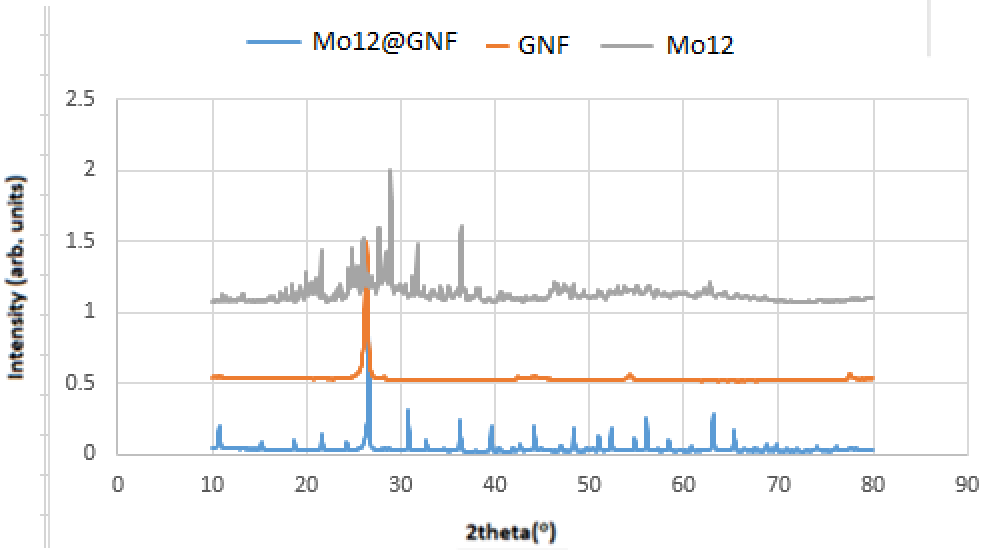

Figure 39. PXRD of Pure GNF, Mo12 and Mo12@GNF

The $K_6P_2Mo_{18}O_{62}$ peak observed besides the peak of GNF at 2θ =28 °, confirms the presence of $K_6P_2Mo_{18}O_{62}$ Poms within each sample of $K_6P_2Mo_{18}O_{62}$@GNF. If we look at the peak at 2θ = (15 °,27 °,28 °,40 °) for the $K_6P_2Mo_{18}O_{62}$@GNF(0.005M) sample, it can be seen that every peak regarding to POM is seen in this sample however in lower quantities, this shows a small amount of POM loading within the GNF which is consistent with the TGA results produced. However as for $K_6P_2Mo_{18}O_{62}$@GNF (0.01M) none of the key POM positions can be seen in this PXRD spectrum, additional peaks can be seen at 2θ= (40 ° and 66.7 °) which are contributed by the formation of MoO_2 due to the unstable nature and breakdown of the Wells Dawson structure. It can also be seen that the $K_6P_2Mo_{18}O_{62}$@GNF nanocomposite contains key keggin peaks at 2θ= (31 ° and 36 °) further facilitating the structure has undergone some sort of degradation. This is also confirmed via the TGA of the bulk POM. Although TGA and PXRD have provided enough evidence of nanocomposite formation it can be shown at higher concentration of precursor leads to the sequential breakdown and formation of Oxides. $K_6P_2Mo_{18}O_{62}$@GNF has been successfully synthesised, however, these analytical techniques do not possess the capability to investigate the size, shape and location of the $K_6P_2Mo_{18}O_{62}$ POMs/Oxide particles. Transmission microscopy (TEM), is a technique which provides information evaluating the size and distribution of particles and therefore leading to a greater understanding of the nature of the material.

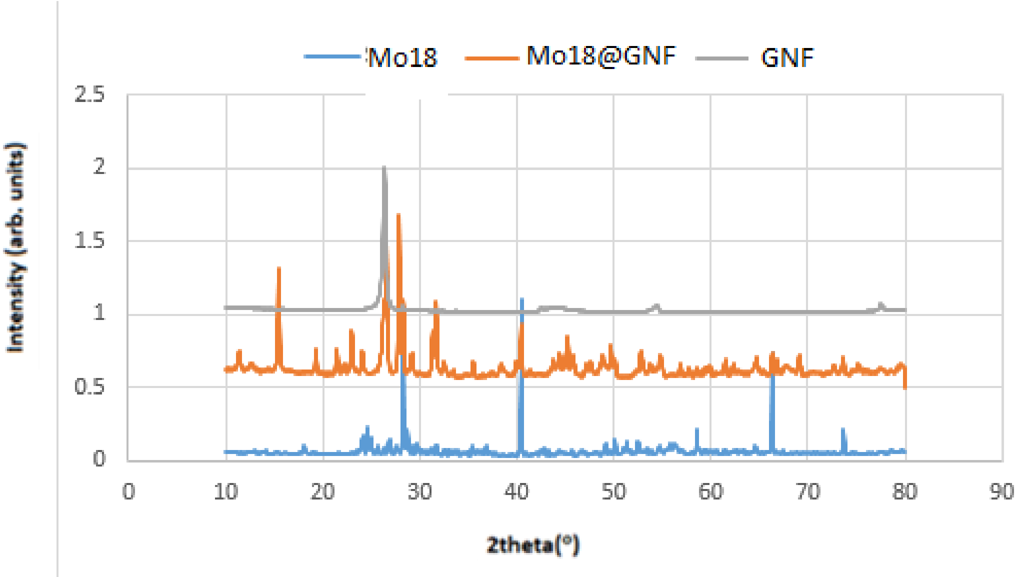

Figure 40. PXRD of Pure GNF, Mo18 and Mo18@GNF

5.1 Transmission electron microscopy (TEM) and Energy dispersive X-ray spectroscopy (EDX)

Although both TGA and PXRD have provided enough evidence of nanocomposite creation at the POM@GNF sites, these analytical techniques do not possess the capability to investigate the size, shape and location of the formed hybrids materials within the GNF itself. Transmission electron microscopy (TEM), is a technique which presents information evaluating both the size and distribution of the host particles, which in turn leads to a greater understanding of the nature of the material. TEM produces a 2D projection of the 3D material, by transmitting a beam of electrons through the sample in order to gather information no other technique has the capability to.

Besides providing information about the location of $K_6P_2W_{18}O_{62}$ nanoparticles inside GNFs, TEM analysis shows particle size, crystal structure and atomic scale arrangements with lattice planes and d spacing. **Figure 41** shows high resolution transmission electron microscopy images (HRTEM) images of $K_6P_2W_{18}O_{62}$@GNF nanocomposites. TEM reveals $K_6P_2W_{18}O_{62}$ nanoparticles are well dispersed within the GNF and are fairly uniform in size. The nanoparticles encapsulated within the internal cavity of the GNFs are shown to be anchored on the internal step-edges as predicted. This suggests the composite material has promising potential for use in electrocatalysis, as the confinement effect enhances the catalytic performance of the material. Using statistical size analysis, it was determined that the mean size of the particles was found to be around a diameter of 1.2-1.8 nm respectively. The small average size of the particles suggests excellent potential for the nanocomposite application within nanoreactors. Furthermore, during TEM analysis, energy dispersive X-ray spectroscopy or more commonly known as EDX was undertaken, EDX allows for the investigation of the elemental composition of the material. EDX analysis confirms the presence of $K_6P_2W_{18}O_{62}$ particles as the data shows characteristic peaks of W and O and C at 22, 14 and 19 eV respectively. Let it be noted that only small potassium signals were observed on the EDX spectra, thus indicating that potassium remained in solution via the filling process. The presence of copper in the sample is also indicated due to the composition of the TEM grid containing the element. Overall the semi-quantitative analytic technique further reinforced the $[P_2W_{18}O_{62}]^-$ assignment previously established via PXRD and TEM. As seen in **fig 41** it can be seen that at smaller concentrations distinct $[P_2W_{18}O_{62}]^-$ particles can be seen anchored within the GNF to the internal step edges, however at higher concentrations of POM and therefore higher amounts of precursor, something unusual occurs. **Fig 42** shows that at higher amounts of precursor (double concentrated solution), the sample became supersaturated forming what seems to be layers of POM particles rather then discrete POMs anchored onto the internal step edges. This phenom of the $[P_2W_{18}O_{62}]^-$ particles arrangement could be due to several reasons. It was first thought, that $[P_2W_{18}O_{62}]^-$ particles would decompose to their Keggin counterparts during encapsulation at high concentrations, however there is no evidence of this seen in either the PXRD or EDX analysis with no peaks corresponding to the crystal planes of either WO_3 or Keggin crystals. However, it was previously mentioned by Tsingdos that an increased POM concentration decreases their respective stability, and this coupled with an increased concentration due to loading effects within the GNF internal channels could cause a lower intermediate pH further along the GNF. Below (FIG) is a proposed mechanism for the results found within the TEM. The proposed mechanism explains that with increasing heterpolyanion concentrations, two conditions change simultaneously; more POM particles are available in the solution and along with them more protons are also available (charge-neutral dissolution). Increasing heteropolyanion solution concentrations will increase the probability of bringing the anions closer together. This can be demonstrated from molecular dynamics simulations which show that increasing proton solution concentrations increases the probability of creating more hydrogen-bonding interactions and hence more attractive interactions. This is due to the large surface area and the attractive van der Waals forces between nanoparticles in the suspension which can lead to them adhering together to form larger structures or agglomerates. The structure and size of these structures depend on different parameters, which can be related to differing conditions such as composition and size. It can be noted that the particle agglomeration can be decreased by effectively enhancing the stability via electrostatic stabilisation and hence discrete particles will be seen. In electrostatic stabilisation, the surfaces of particles become charged in order to prevent collisions between themselves and pH is one of the keys to particle stability. It is known that electrostatic stabilisation is dictated by the zeta potential, however for good stability the zeta potential value of the suspension needs to be high in both positive and negative values. In other words once the isoelectric point has been reached nanoparticles lose their ability to retain stability and undergo particle agglomeration at high rates. Different sizes and structures of particle agglomerates are able to be obtained thus altering the zeta potential and therefore altering the pH. Particle allogmeration is merited by two process of which are diffusion-limited agglomeration and reaction-limited agglomeration. In the process of diffusion-limited agglomeration the repulsive forces between particles are weakened and the pH value of the particles is often at or close to the isoelectric point. This coupled with the reduced space within the matrix of the GNF leads to a linear type of agglomeration where the particles are loosely packed together. Overall these increased interactions force POM molecules closer together and therefore the space between them is very limited and hence the structures in **fig 42** are seen. This idea seems to be further confirmed via PXRD as there are no peaks relating to any decomposition products, however Wells-Dawson peaks are still intact under confinement.

Overall the analysis thus far can confirm the formation of small encapsulated POM nanoparticles within the $[P_2W_{18}O_{62}]^-$ @GNF 0.005M composite and the formation of what seems to be agglomerated POM particles within the $[P_2W_{18}O_{62}]^-$ @GNF 0.01M composite sample. The $[P_2W_{18}O_{62}]^-$ @GNF 0.005M nanocomposite material has excellent catalytic potential due to the unrestricted diffusion and discrete POM particles accessible to electrochemical reaction combined with confinement effects caused by encapsulation.

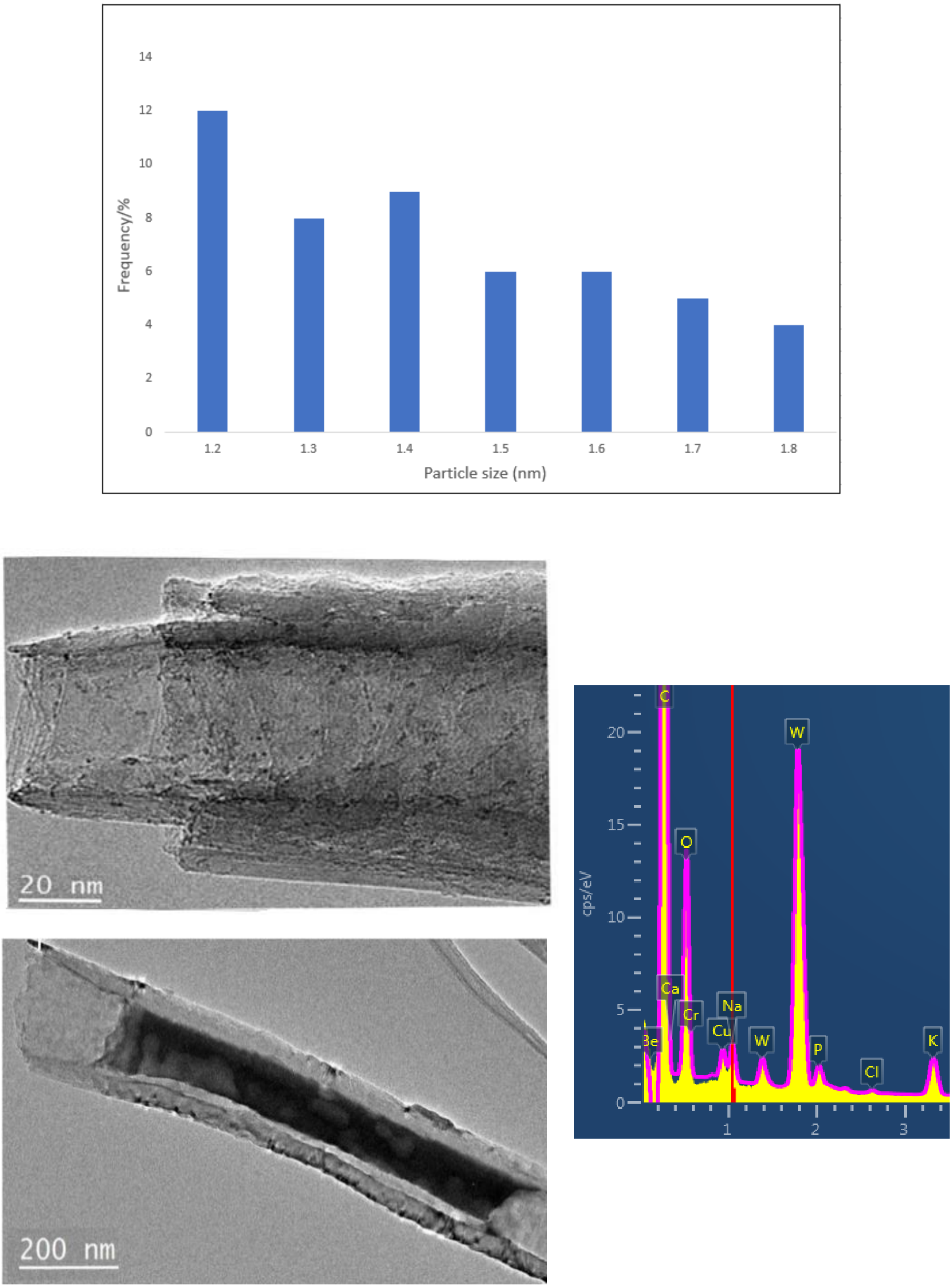

Figure 41. a) Statistical analysis of $K_6P_2W_{18}O_{62}$ nanoparticles b) TEM images of $K_6P_2W_{18}O_{62}$ nanoparticles (0.005M) c) TEM images of $K_6P_2W_{18}O_{62}$ nanoparticles (0.01M) d) EDX of $K_6P_2W_{18}O_{62}$ nanoparticles

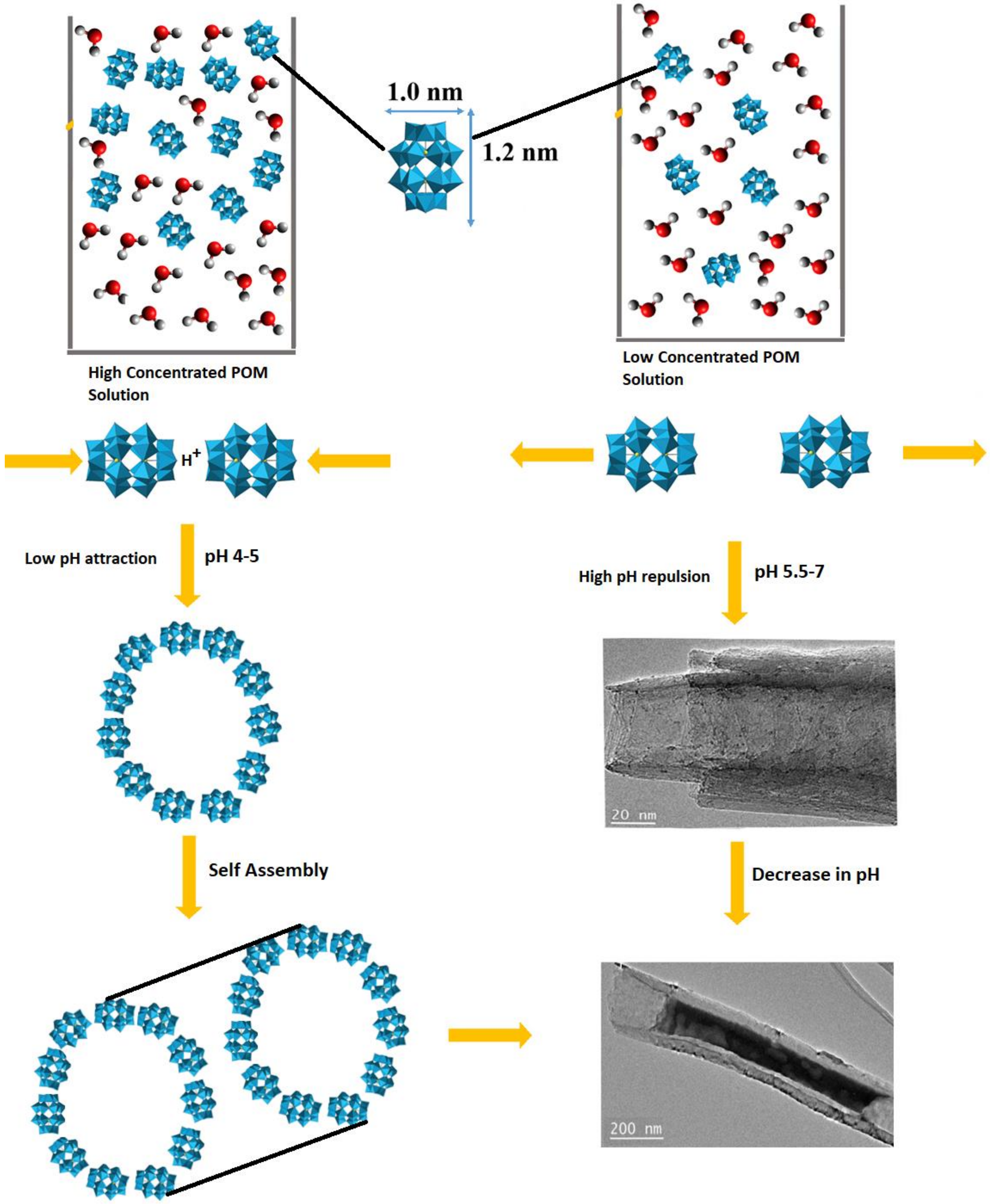

Figure 42. Schematic representation of POM tubular structure within GNFs

5.2 TEM OF $K_3PMo_{12}O_{40}$@GNF

High-resolution transmission electron microscopy of $K_3PMo_{12}O_{40}$@GNF shows poor dispersion of POMs throughout the GNF (FIG). It can be shown that the dark-contrast POMs in the TEM images are 0.4-0.7 nm wide. As seen in the higher concentration $K_3PMo_{12}O_{40}$@GNF sample, POM clusters fairly uniform in size and spherical 22-55nm **fig 44** have formed on the outside of the GNF, whilst single POM particles have formed in the tips of the GNF and long cylindrical POM structures(FIG) have formed deep within the GNF channels. As previously mentioned, it is thought that these cylindrical POM structures occur via the mechanism outlined in (FIG).

Using an increased concentration solution for filling causes super saturation of the sample, this occurs when a solution approaches a critical concentration, the solutes start to separate out of the solution and form crystals like that of how crystals are formed via nucleation. It is well known that Keggin POMs have acquired interest from research groups due to their self-assembling behaviours in solution often forming spherical structures known as "Blackberries". Although it is not exactly known or fully understood how this process occurs, it can be shown that POMs interact via short-range attractions and long range repulsions (FIG REF) The short-range attractions are due to the hydrogen-bonding interactions with protons (i.e., H_3O^+) and water molecules as mentioned previously, whereas the long range repulsions are due to screened columbic interactions. This is quite unique as it allows for both encapsulation and adsorption of POMs onto both the outside and inside of the GNF simultaneously. Using the models created, a pathway for this uptake coupled with this adsorption can be imagined **fig 45**. It is thought that when GNFs come into contact with POMs electron density is transferred from the GNFs to the POMs resulting in partially reduced POMs and positively charged GNFs. This results in an electrostatically driven encapsulation of negative POMs within the positively charged GNFs, however in higher concentration solutions, the sample becomes super saturated before the GNFs have been added, POM crystals start to form via short range attractions due to hydrogen-bonding interactions with water molecules. This means that when GNFs are added to the solution, electrostatic attraction occurs between both the small reduced POMs and the big anionic POM crystals that have formed resulting in both encapsulation and adsorption. The samples were also washed to make sure that POM crystals had actually adsorbed to the surface of the GNF and these crystals were not just “metal impurities” the washed samples were then examined via PXRD (FIG) and TEM and it was found that the samples had not changed further providing evidence for the adsorption of POM crystals onto the GNF **fig 43**

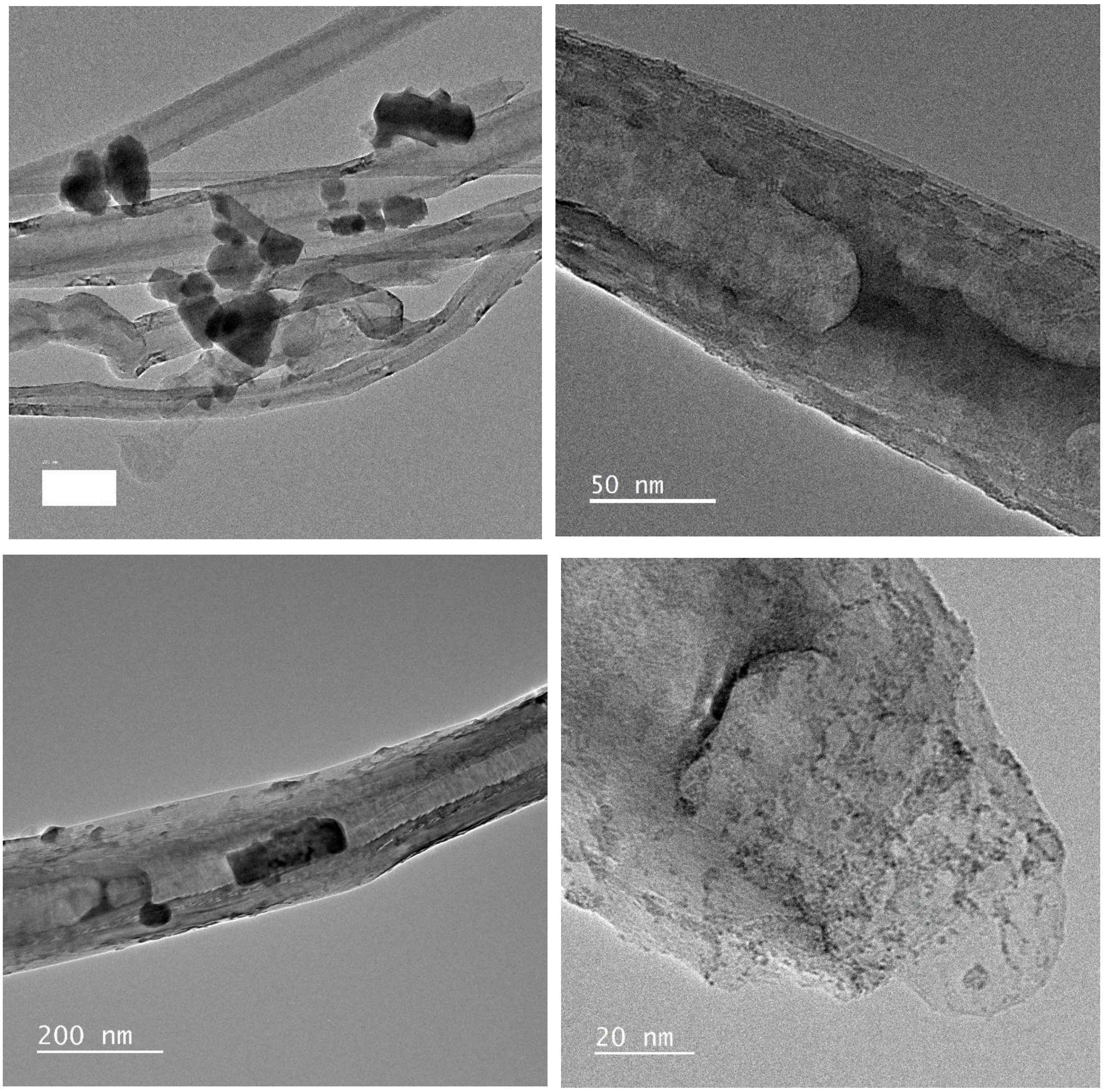

Figure 43. TEM images of $K_3PMo_{12}O_{40}$***@GNF***

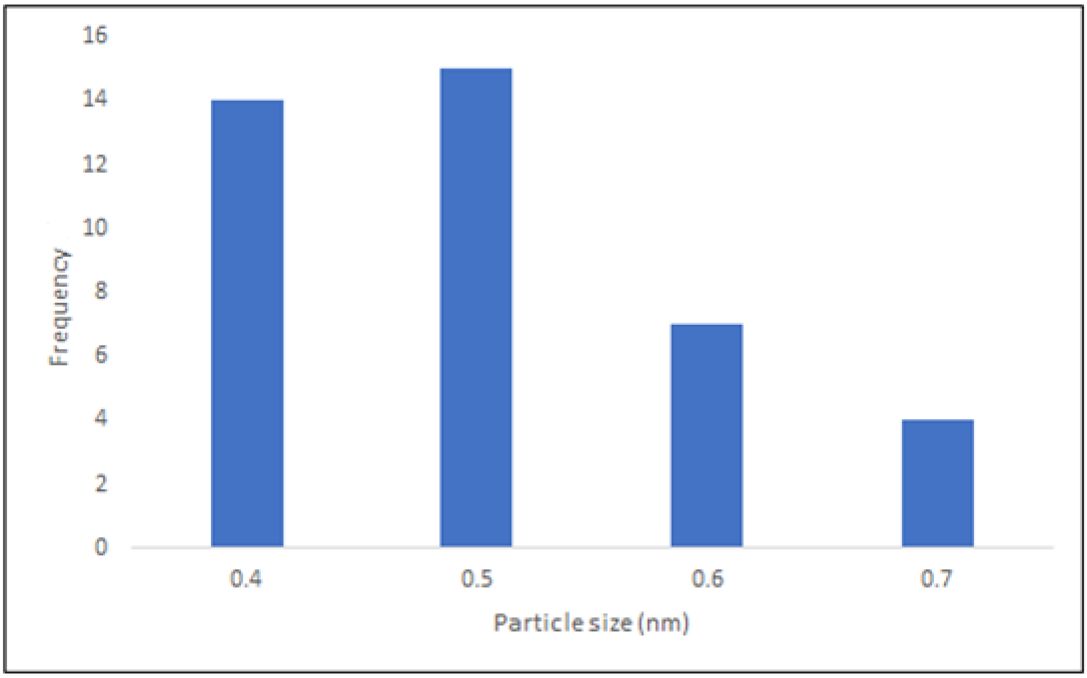

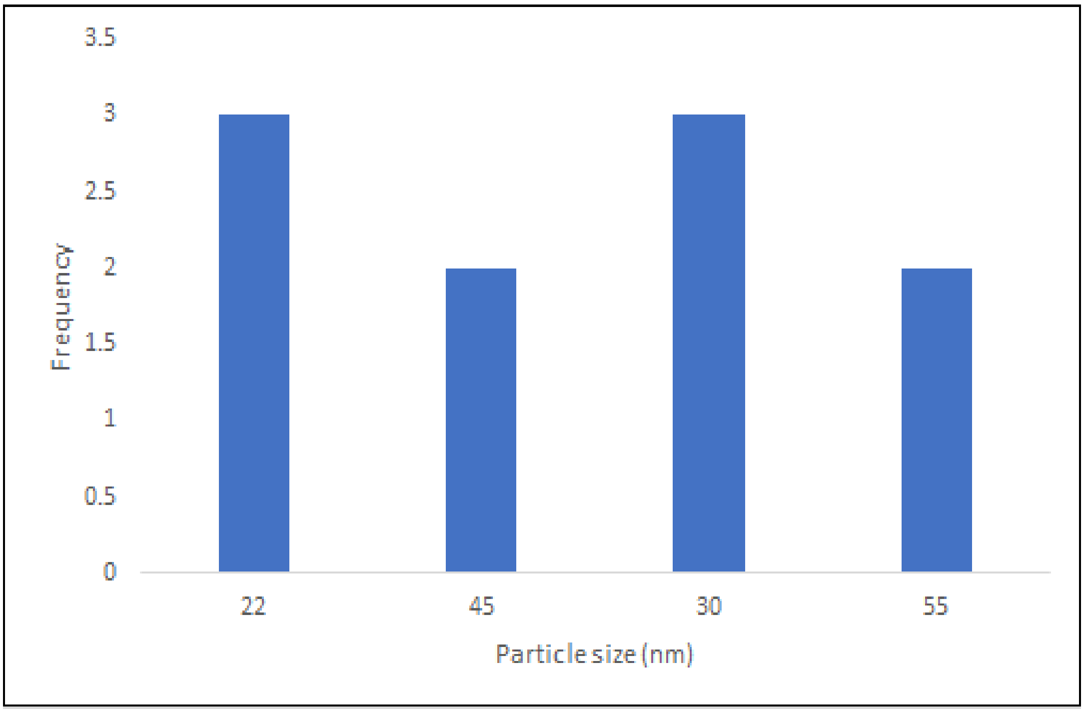

Figure 44. Size analysis of discrete POMs encapsulated within the GNF and Particles adsorpt onto the side of the GNF

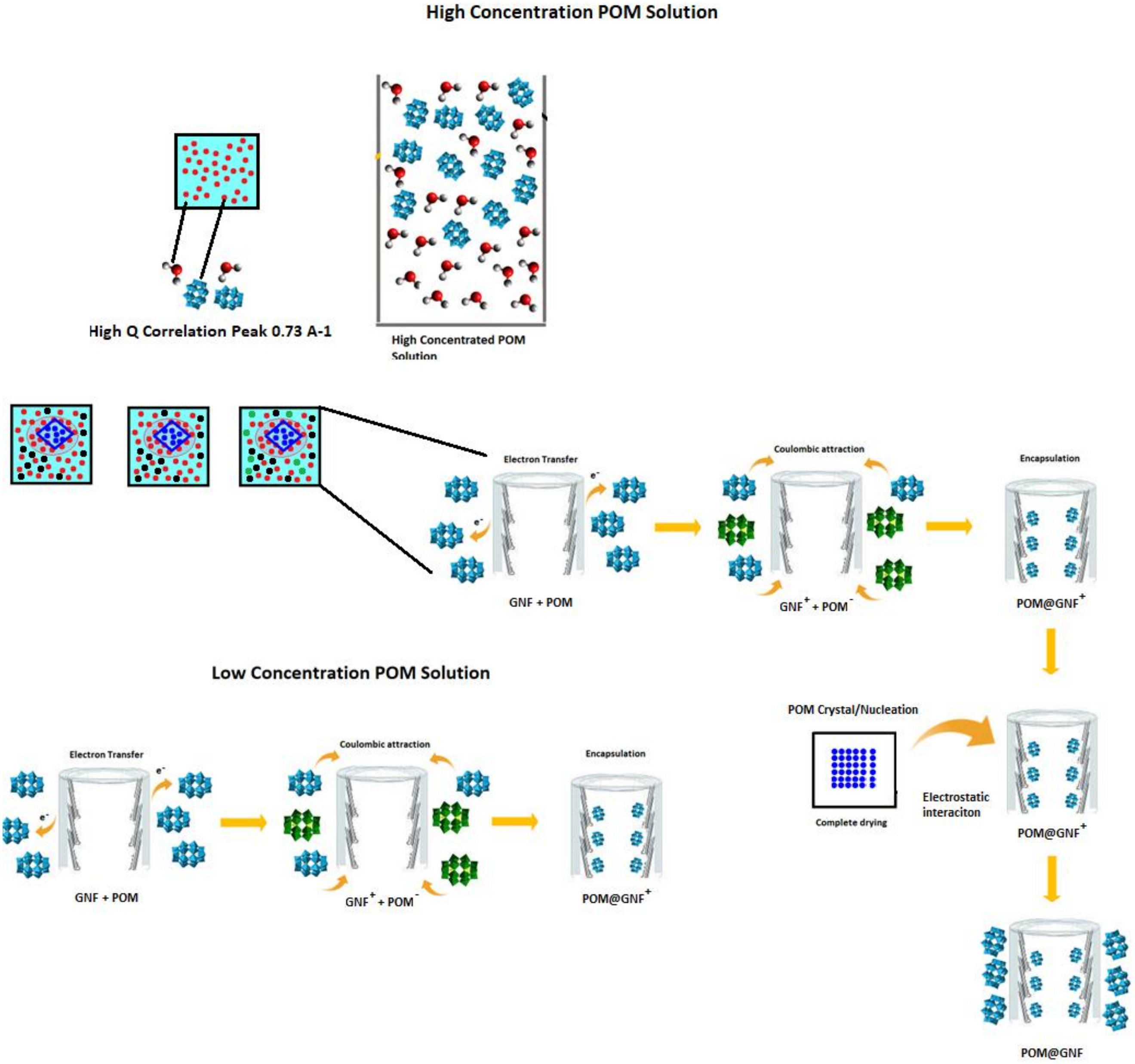

Figure 45. Schematic diagram for the encapsulation and adsorption of POMs to GNFs

5.3 TEM OF $K_6PMo_{18}O_{62}$@GNF

Fig 46 shows high resolution transmission electron microscopy images of both 0.005M and 0.01M $K_6PMo_{18}O_{62}$@GNF samples. TEM images reveal that in $K_6PMo_{18}O_{62}$@GNF POM particles were found to be around 0.8nm in size. For 0.005M concentration composite, POM particles have been encapsulated within the GNF and have adhered to the step edges as predicted. The small average size of the particles suggests excellent potential for the nanocomposite application within nanoreactors. Furthermore, during TEM analysis, energy dispersive X-ray spectroscopy was undertaken EDX analysis confirmed the presence of $K_6P_2Mo_{18}O_{62}$ particles as the data shows characteristic peaks of M and O and C at 22, 25 and 65 eV respectively. As seen in the above TEM samples of the other POMs at high precursor amounts POM agglomerates have formed which was promptly formed by the overfilling of the GNF. It was also seen that on a higher concentration of filling, MoO2 had formed on the subsequent decomposition of the Dawson structure during its encapsulation, this was seen on the PXRD earlier and is further proved via the EDX of the material, which shows characteristic peaks of Mo to O in a 1:2 ratio. The decomposition of the Wells-Dawson unit was expected due to their poor stability and the likehood of their decomposition was greatly increased under confinement.

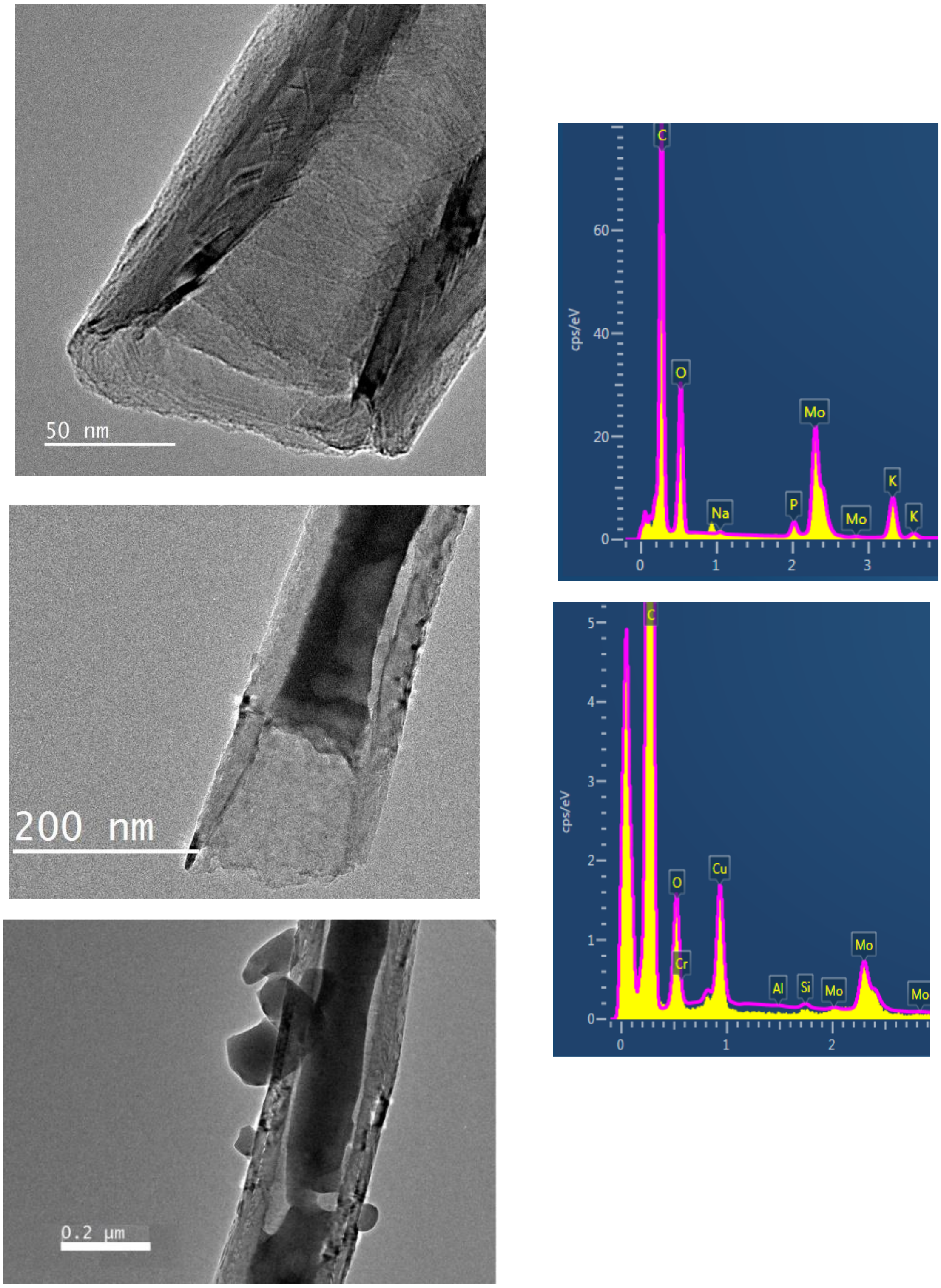

Figure 46. a) TEM image of $K_6P_2Mo_{18}O_{62}$@GNF (0.005M) b) EDX of $K_6P_2Mo_{18}O_{62}$@GNF (0.005M) c) TEM image of $K_6P_2Mo_{18}O_{62}$@GNF (0.01M) d) EDX of $K_6P_2Mo_{18}O_{62}$@GNF

5.4 TEM OF $K_3PW_{12}O_{40}$@GNF

Previous assignments from both TGA and PXRD suggest the formation of a $K_3PW_{12}O_{40}$@GNF nanocomposite, however, to ascertain the size and location of the nanoparticles within the GNF TEM was performed on the sample. Although previous PXRD suggested no formation of WO_3 within the sample it can be see that within the TEM images that small discrete POMs have not formed, however large WO_3 has formed with an average size of around 2-5nm, this formation was also proved via the EDX which clearly shows a Tungsten to Oxygen ratio of 1:3 at 1.5 and 0.4 eV respectively. Although no effort was made to produce WO_3 it has formed mostly due to human error, this could be because a calcined sample was accidently filled instead of a uncalcined sample, this mistake would account for the finding on both the TEM and EDX as the $K_3PW_{12}O_{40}$ POM is susceptible to degradation under increased heating. This fact is further proved via looking at TEM images of the other POMs analysed. As the saturation limited of other POMs was reached, tubular structures of close compact POM formation were seen yet no subsequent decomposition was seen, however this was not seen in this sample. Going by the trend, it makes no sense that these Tungsten Keggin POMs would decompose within the GNF with no evidence of small nanoparticle formation (as seen in the other samples) and therefore it is highly likely that the wrong sample has been filled.

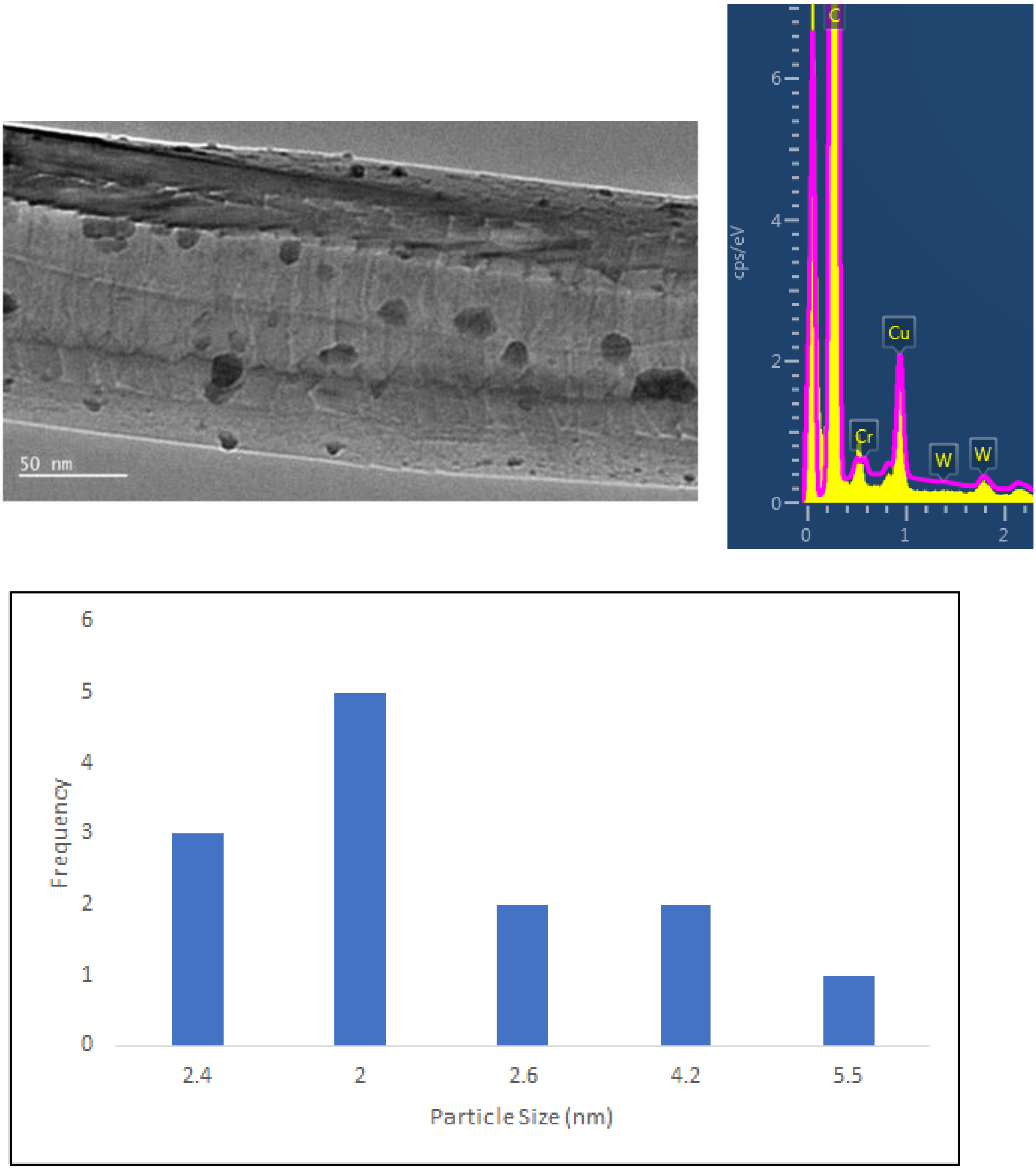

Figure 47. a) TEM image of $K_3PW_{12}O_{40}$@GNF b) EDX of $K_3Pw_{12}O_{40}$@GNF) c)EDX of $K_3PW_{12}O_{40}$@GNF

5.5 Electrochemistry of $K_6P_2W_{18}O_{62}$/ $K_6P_2W_{18}O_{62}$@GNF

In order to assess the feasibility of the synthesised $K_6P_2W_{18}O_{62}$/ $K_6P_2W_{18}O_{62}$@GNF composites for use within electrochemical storage, electrochemical experiments were carried out on the prepared samples. As noted in previous sections, POMs have an incredibly rich range of electrochemical properties, this is due to their highly reversible reduction waves. Unfortunately, as bulk POMs are insulating, attempts at forming coherent energy storage devices is difficult. Most attempts so far have focused on the adsorption of POMs onto the outside of carbon surfaces such as graphene and the outside walls of nanotubes. When POM composites are formed this way there are problem with chemical instability and there is a low affinity for carbonaceous support. These problems presented problems for application of POMs within real life devices, however GNFs are highly conductive and exponentially increase the contact of POMs with the substrate due to their step edges, this presents a good possible substrate for the loading of redox active POMs. Furthermore, the protective ability of GNFs allows a higher performance of potential catalysts over a long period therefore maximising the efficiency of the material. Using previously reported literature, it is known that in acidic conditions $0 < pH < 3$, $K_6P_2W_{18}O_6$ undergoes four reversible reduction at approximately: -0.005, -0.135, -0.380 and -0.610 respectively. Let it be noted that both (6) and (7) are double wave reductions accompanied by the addition of two protons. The equations for each reduction can be seen below.

$$P_2W_{18}O_{62}^{6-} + e^- \longleftrightarrow P_2W_{18}O_{62}^{7-}$$

$$P_2W_{18}O_{62}^{7-} + e^- \longleftrightarrow P_2W_{18}O_{62}^{8-}$$

$$P_2W_{18}O_{62}^{8-} + 2e^- + 2H^+ \longleftrightarrow H_2\,P_2W_{18}O_{62}^{8-}$$

$$H_2P_2W_{18}O_{62}^{8-} + 2e^- + 2H^+ \longleftrightarrow H_4P_2W_{18}O_{62}^{8-}$$

These reduction peaks are labelled on the below figures and are similar to those reported by other research groups. Cyclic voltammograms experiments was carried out on both $K_6P_2W_{18}O_{62}$/ $K_6P_2W_{18}O_{62}$@GNF samples and confirmed that upon encapsulation, both materials retained the redox chemistry of the confined species. In the $K_6P_2W_{18}O_{62}$@GNF sample three reversible redox peaks were observed at -0.153, -0.346 and -0.574V respectively. It can be determined that all three reductions are one electron reductions, based on the $\Delta E_{1/2}$ values of (62,61,55). The current response increased with the increase of the scan rate and similar curves with three pairs of redox peaks were observed at all scan rates, with little to no distortion. This observation indicates sufficient electron transfer from the $K_6P_2W_{18}O_{62}$@GNF composite to the electrode in all subsequent redox steps. The negative shift in redox potentials between the standard POM and the composite, indicates there is a charge effect from the GNF-host to the POM guest species. Concomitantly, no leaching was observed when the potential was cycled between − 0.2 and 0.5 V. Using the cyclic voltammetry data gathered, samples suggest that electron transfer is rapid between the electrode and the POM molecules. There is shown to be a linear relationship between the scan rate and peak current, as well as the peak to peak separation. Based on the redox peaks of $K_6P_2W_{18}O_{62}$@GNF, at 1 Vs^{-1} their peak separations (ΔE_p) were calculated to be as small as ≈ 17–50 mV thus indicating that the system is not limited by diffusion with an extremely rapid electron transfer. Using this data, the effective concentration of electrochemically accessible POM can be calculated.

$$Q = \Gamma / nFA$$

Where Q is electrolysis charge, F is faradays constant, n is the number of moles of electrons and A is the area of the electrode. Comparing Γ to the known wt% loading from TGA suggests that over 68% of the POM species are electrochemically accessible.

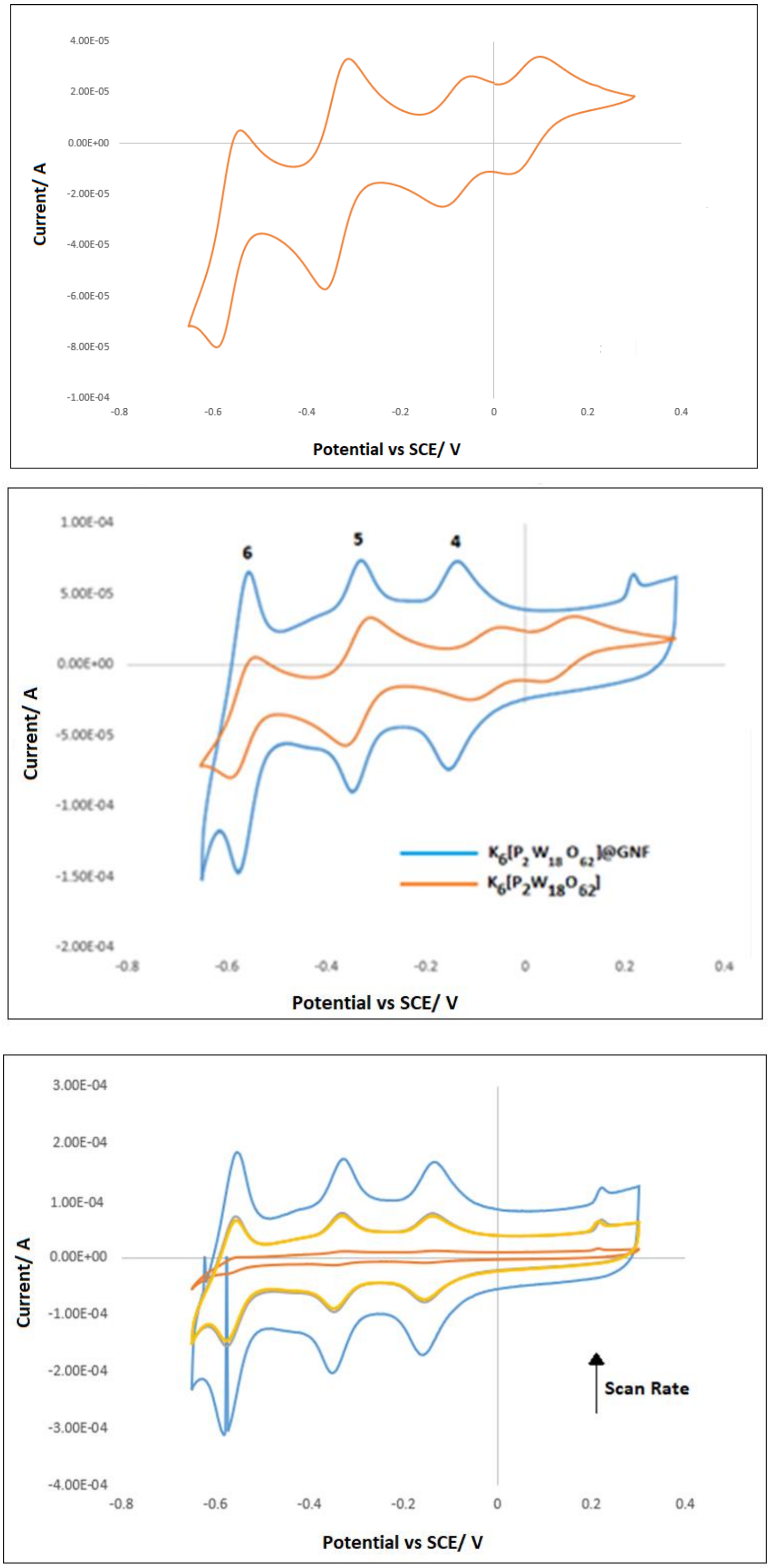

Figure 48. CVs of a) $K_6P_2W_{18}O_{62}$ b) $K_6P_2W_{18}O_{62}$@GNF c) $K_6P_2W_{18}O_{62}$@GNF at different scan rates.

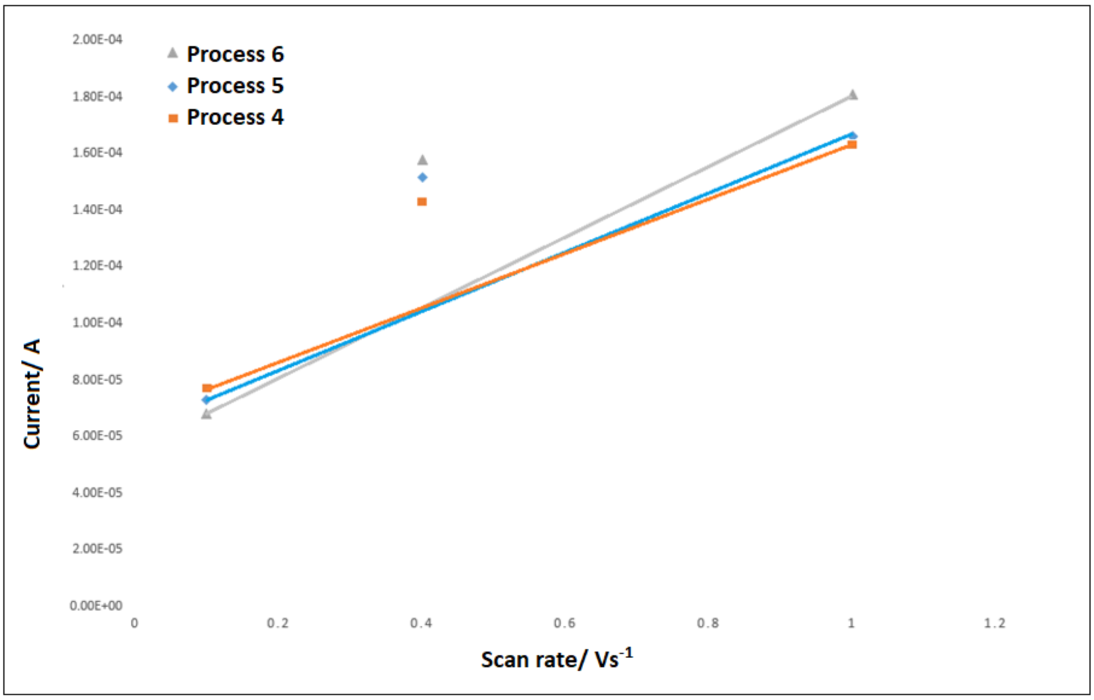

Figure 49. peak currents plotted for [$P_2W_{18}O_{62}$] @GNF against varied scan rates

5.6Electrochemistry of $K_6P_2Mo_{18}O_{62}$@GNF

Molybdenum POMs are known for their ability to accept a high number of electrons, which makes them incredibly interesting for their potential applications within electrochemical reactions, in particular energy storage. It has been shown that some molybdenum POMs can even accept up to 24 electrons per molecule. Using the data acquired, it can be shown that the Wells-Dawson $[P_2Mo_{18}O_{62}]^{6-}$ anion on its own undergoes four reversible reduction waves at approximately: 0.544, 0.418, 0.236 and 0.04 respectively. All reductions are accompanied by the equivalent number of protons:

$$P_2Mo_{18}O_{62}^{6-} + 2e^- + 2H^+ \longleftrightarrow H_2P_2Mo_{18}O_{62}^{6-}$$

$$H_2P_2Mo_{18}O_{62}^{6-} + 2e^- + 2H^+ \longleftrightarrow H_4P_2Mo_{18}O_{62}^{6-}$$

$$H_2P_2Mo_{18}O_{62}^{6-} + 2e^- + 2H^+ \longleftrightarrow H_6P_2Mo_{18}O_{62}^{6-}$$

$$H_6P_2Mo_{18}O_{62}^{6--} + 4e^- + 4H^+ \longleftrightarrow H_{10}P_2Mo_{18}O_{62}^{6-}$$

These peaks can be found labelled in fig and match well with those reported in the literature. Preliminary CV experiments carried out on [$P_2Mo_{18}O_{62}$] @GNF show that the redox chemistry of the POM can still be accessed via the GNF upon encapsulation. Four reversible redox waves are observed at 0.566, 0.414, 0.277 and 0.052. $\Delta E_{1/2}$ values of 49, 57, 51 and 41 mV indicate that reductions 1' and 4' proceed with a two-electron transfer, whilst 2' and 3' proceed with a one electron transfer, assuming all processes are surface bound. Akin to the tungsten analogues presented above, electron transfer mediated by the GNF on the surface of the electrode is rapid and reversible, which is demonstrated by varying the scan rate as seen below. All CVs were recorded in 1M H_2SO_4 using a glassy carbon working electrode, platinum counter electrode and a SCE reference electrode. Concomitantly, no leaching was observed when the potential was cycled between − 0.2 and 0.5 V. Using the cyclic voltammetry data gathered, samples suggest that electron transfer is rapid between the electrode and the POM molecules. There is shown to be a linear relationship between the scan rate and peak current, as well as the peak to peak separation. Based on the redox peaks of $K_6P_2Mo_{18}O_{62}$@GNF, their peak separations (ΔE_p) were calculated to be as small as ≈ 20–50 mV thus indicating that the system is not limited by diffusion with an extremely rapid electron transfer. Using this data, the effective concentration of electrochemically accessible POM can be calculated.

$$Q = \Gamma/nFA$$

Where Q is electrolysis charge, F is faradays constant, n is the number of moles of electrons and A is the area of the electrode. Comparing Γ to the known wt% loading from TGA suggests that over 68% of the POM species are electrochemically accessible.

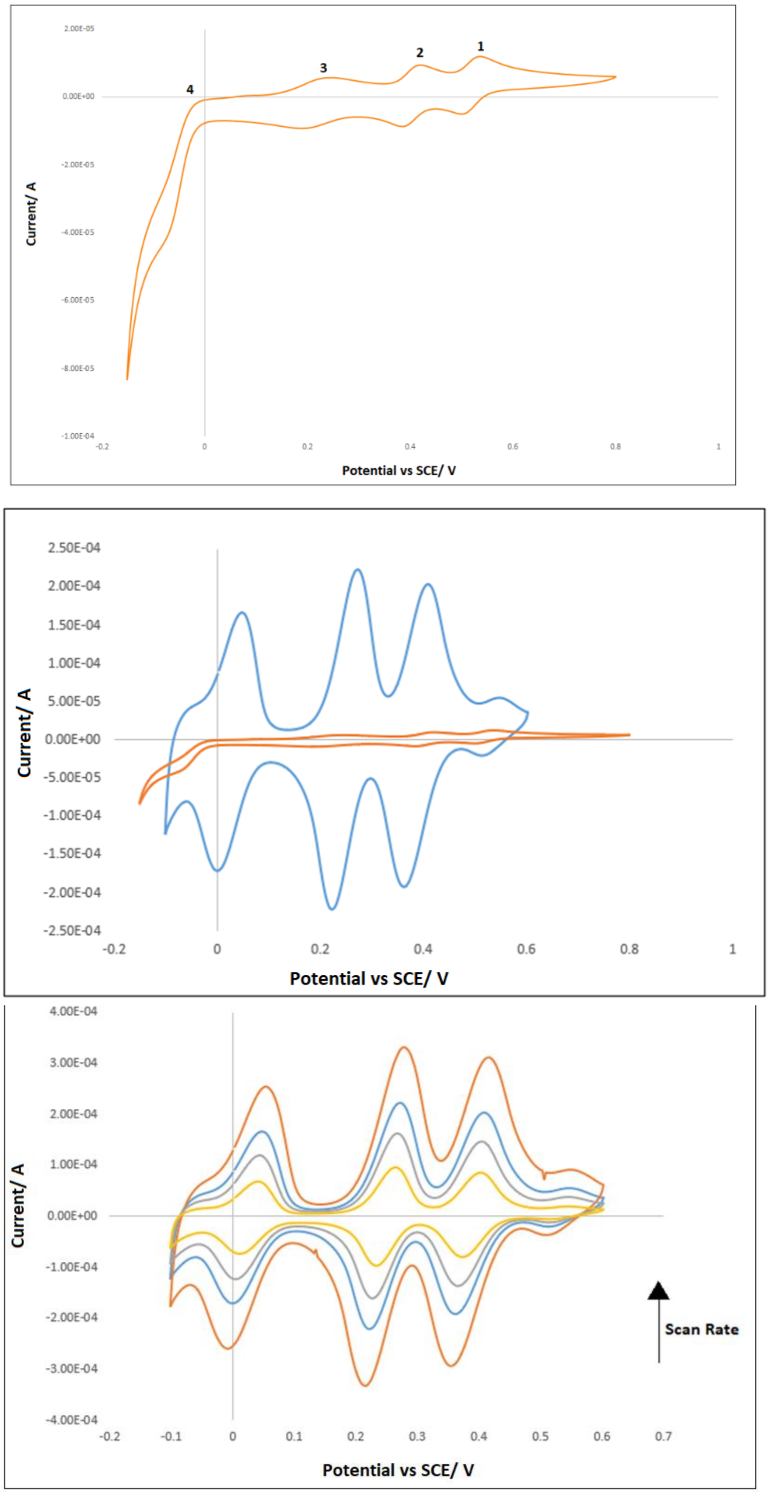

Figure 50. CVs of a) $K_6P_2Mo_{18}O_{62}$ b) $K_6P_2Mo_{18}O_{62}$@GNF c) $K_6P_2Mo_{18}O_{62}$@GNF at different scan rates.

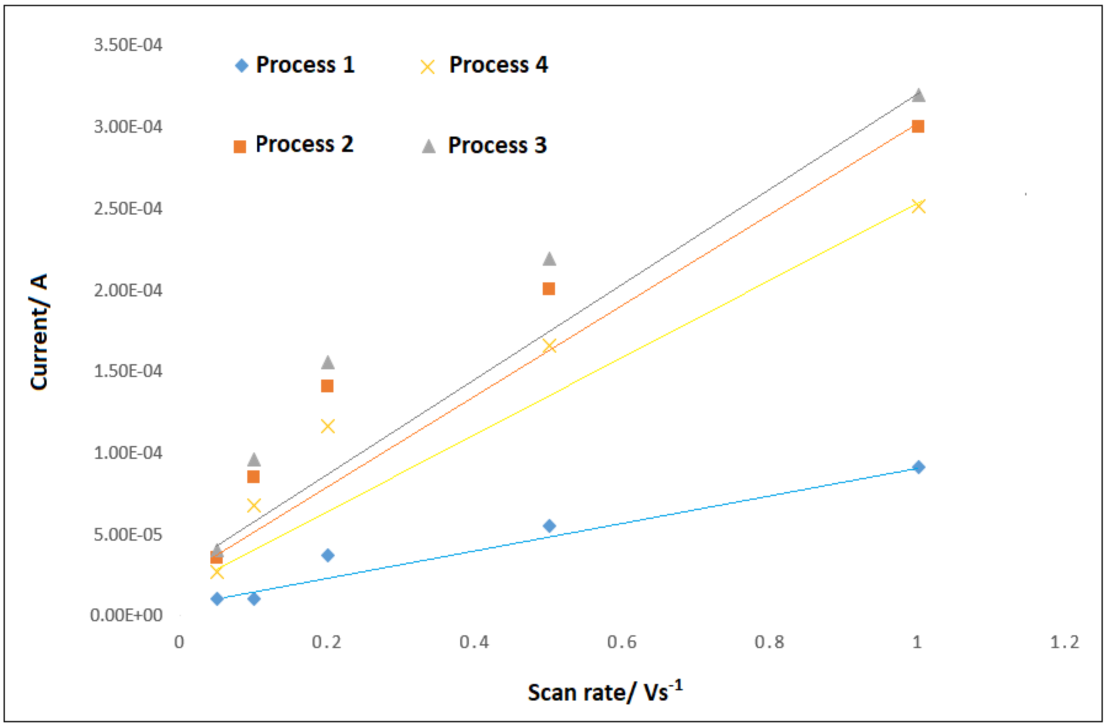

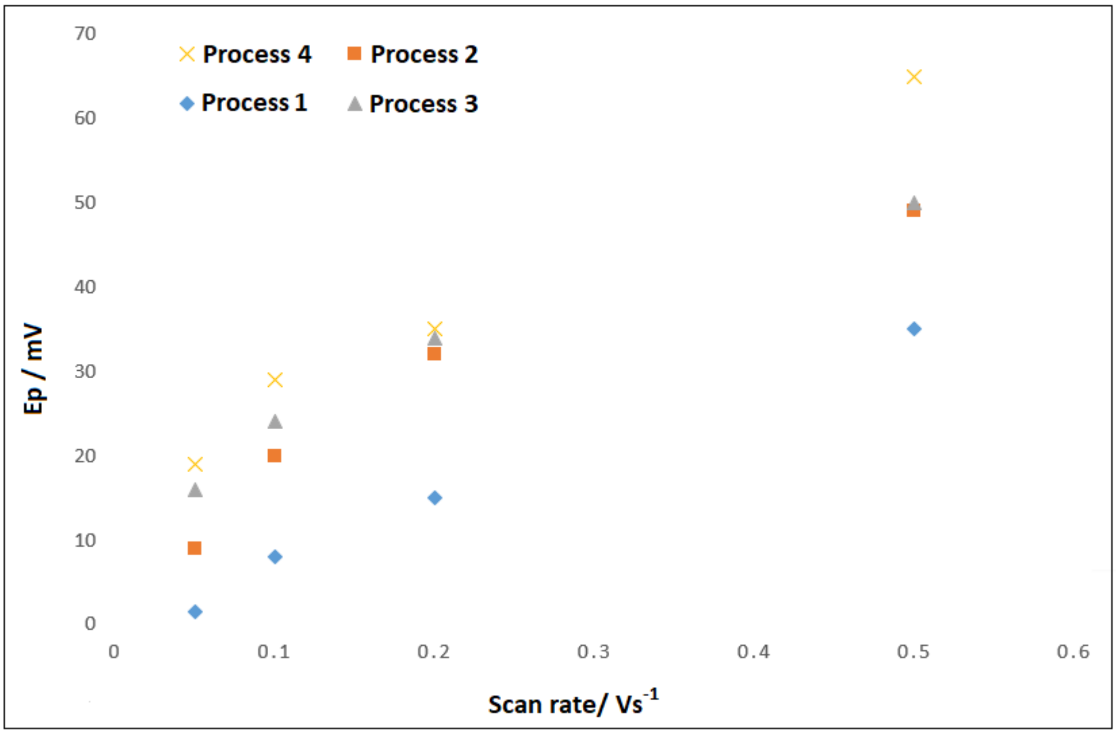

Figure 51. Peak currents plotted for $K_6P_2Mo_{18}O_{62}$@GNF and Ep values plotted for $K_6P_2Mo_{18}O_{62}$@GNF

5.7 Conclusion

The work outlined above presents the successful encapsulation of POMs within GNFs with a varied molecular structure and elemental composition. This unexpected result likely proceeds due to the rich redox chemistry of the POMs oxidising the GNFs upon their addition to the POM solution. Partially successful encapsulation and characterisation of four polyoxometalates has been shown within nanostructured carbon, in this case GNFs. The oxidising effect from encapsulation leads to an increased electrostatic interaction between the GNF and the POM, which in turn makes encapsulation a more favourable process. Uptake of the POMs within the GNF is high, confirmed with thermogravimetric analysis, however it was seen that an increased concentration of POM loading increased the likelihood of supersaturation and formation of compact linear POM structures. Local environmental analysis carried out via TEM confirmed the presence of a high number of encapsulated POM molecules within the GNFs and captured bulk Oxide adsorbed to the outer edges of the GNF on the degradation of the POM units. Analysis of the species show that sizes of the species corroborates well with the known size of POMs, with the range of POM sizes attributed to interactions of the sample with the electron beam. Inter atomic M-M distances match well with TEM images, which further provides evidence that the encapsulated species is both POM and Oxide. A periodic repeated structure was observed for both molybdenum and tungstate POMs, indicating that the driving force for encapsulation is substantial and that filling rates are high. Observations made through the research via PXRD, TEM and EDX all suggest that POMs are highly sensitive to encapsulation and will degrade to their oxide forms and form linear compact POM structures on an increased concentration uptake due to the GNF confinement effect/supersaturation of the sample. It was also noted that pH within the sample plays a key role in the formation of these structures and a sample of the correct concentration should be prepared if only discrete POM particles are wanted. Preliminary electrochemical reactions were done on both Wells-Dawson compsoites. Electrochemical measurements demonstrate that redox processes of the POM species are still active when confined. The measurements demonstrate that GNFs have the ability to act as highly effective conduction substrates from the electrode, allowing for the reversible and rapid transferring of electrons from the redox active POMs confined within them.

5.8 Future Work

The materials synthesised for this study show promise as electrochemical energy storage materials. Filling rates at differing pH's and temperatures should be investigated due to the dependent POM stability on both their pH and temperature. It should be noted that concentration studies to study the effect of uptake of POMs within the GNF should also be undertaken. So far, only ex situ encapsulation of POMs has been carried out and therefore in future works, in situ filling of POMs should be investigated, possibly isolating novel POM species and increasing filling rates further. Additionally, interactions of POMs.

Further work should be carried out on further characterisation of both molybdenum samples for the formation of test batteries/capacitors with the materials described within this report. Real life energy storage materials must be light for them to be portable. Synthesis of POM@GNFs with POMs composed of lighter elements such as vanadium should also be carried out for investigations into their confinement effects and also in their energy storage capabilities. Further work should also be done to test the stability of the nanocomposites stability over long cycles too see if they retain their electrochemical potency over long use.

Overall POMs are known for their high desirable photo activities, and so encapsulation of POMs within other nanotubes, such as BNNT, or Ti/NT should be carried out to investigate the effect of confinement on the optical and catalytic properties of POMs.

It can be shown that POM catalysis can be applied to many different reactions and as mentioned within this report, it can be induced through a multitude of stimuli. Encapsulation of POMs within larger CNT structures should also be undertaken to test their catalytic effectiveness in both thermal and electro catalysis.

5.9 General

All common reagents and solvents were purchased and used as received from Sigma-Aldrich. Graphitised Nano fibres (PR-19) were purchased from Pyrograf Products Inc.

NMR data was acquired on using a Bruker DX300 300MHz spectrometer.

Thermogravimetric analysis was obtained using a TA Q500 analyser, on platinum pans. In all cases ramp rates were 100^0C per minute to 1000^0C.

MALDI-ToFMS analysis was performed using a Bruker ultraFlexIII instrument. Samples were mixed in solution with (DCTB) which was used as a matrix and then deposited on a stainless-steel target plate (type MTP384). A pulsed solid-state UV laser (355nm) was used to ionise the sample and matrix. The instrument was operated in REFLECTRON mode.

Transmission electron microscopy images were acquired on a JOEL 2100F TEM field emission gun microscope at both 100 kV and 200 kV. Samples were prepared by dispersion of isopropyl alcohol (IPA) and were dispersed onto a copper grid mounted with a carbon film. All images were processed using Gatan Digital Micrograph, and quoted distances were measured by drawing a line profile and measuring the electron density.

EDX spectra were acquired for samples mounted on copper TEM grids using an Oxford instruments INCA X-ray microanalysis system.

POM electrochemistry experiments were performed on an Autolab PGSTAT302N. Electrodes were purchased from IJCambria and Mertrohm. The electrochemistry was performed using a three-electrode set up with a reference Ag/AgCl reference electrode, a platinum counter electrode and a glassy carbon working electrode. The sample was drop cast from a 10 mg/ mL DMF suspension after sonication onto the glassy carbon and left till completely dry.

Synthesis of $K_6P_2W_{18}O_{62}$

$Na_2WO_4.2H_2O$ (100 g, 0.3 moles) was dissolved in water (117 ml). This solution was then set to rapidly stir. HCl (4 M, 83 ml) was then added dropwise to the solution at a rate of 5 drops per second. Upon the addition of HCl a white precipitate formed, however once the addition was completed the precipitate had dissolved. H_3PO_4 (4 M, 83 ml) was then added dropwise to the solution at a rate of 3 drops per second. This dropwise additional results in the formation of a clear yellow solution, which was then refluxed and constantly stirred for 8 hours. Once the reaction was complete, the clear yellow solution was removed the heat and allowed to cool to room temperature ($25^{O}C$). KCl (50 g, 0.67 moles) was then added to the solution with constant stirring. A white precipitate immediately formed, and the solution was then filtered to give a white solid, which was consequently allowed to air dry overnight. The white solid was then re dissolved in water (50 ml) and heated to 100 ^{O}C. This was left for 2 hours, with no stirring, giving a dry white crystalline solid of $K_6P_2W_{18}O_{62}$ (65.5 g, 83% yield) 31P NMR (δ, D_2O) -12.6ppm

Synthesis of $K_6P_2W_{18}O_{62}$@GNF

GNFs (10.0 mg) were heated to 500 ^{O}C for 40 minutes. The resulting black solid was then added to a rapidly stirred solution of $K_6P_2W_{18}O_{62}$ in water (0.05M). On addition of the GNF to the solution, the solution did not change colour. The mixture was briefly sonicated for 5 minutes and the resulting dispersion was stirred for 2 days at room temperature ($25^{O}C$). The black suspension was then filtered through a PTFE filter, giving a colourless liquid and a black solid, which was then dried in the desiccator for 2 days.

Synthesis of $K_6P_2Mo_{18}O_{62}$@GNF

GNFs (10.0 mg) were heated to 500 ^{O}C for 40 minutes. The resulting black solid was then added to a rapidly stirred solution of $K_6P_2Mo_{18}O_{62}$ in water (0.05M). On addition of the GNF to the solution, the solution did not change colour. The mixture was briefly sonicated for 5 minutes and the resulting dispersion was stirred for 2 days at room temperature ($25^{O}C$). The black suspension was then filtered through a PTFE filter, giving a colourless liquid and a black solid, which was then dried in the desiccator for 2 days.

Synthesis of $K_6P_2Mo_{18}O_{62}$

A mixture of $Na_2MoO_4.2H_2O$ (20 g) was mixed with H_3PO_4 (3 ml) and concentrated HCl (16.5 ml) in 50 ml of distilled water. The mixture was then boiled at reflux for 8 hours. After 3 hours, a yellow solution had formed. After the 8 hours had passed, the mixture was taken off the heat and left to cool down at room temperature. The mixture was then filtered via a Buchner flask which resulted in a clear yellow solution. KCl (50 g) was added. The precipitation of a yellow solid was observed immediately after the addition of KCl. This precursor and the supernatant solution were then kept at 50C for 24 hours in order to enhance the precipitation. The solid was filtered on a Buchner funnel and then dissolved in the minimum amount of distilled water (25 ml). KCl (25 g) were added to re-precipitate the salt. The precursor and supernatant solution were kept at 50C for a further 24 hours. The salt was filtered and washed with ethanol (15 ml) and anhydrous diethyl ether (15 ml) and dried at room temperature giving a dry yellow crystalline solid of K6[Mo18P2O62].14H20 (9.3 g, 45% yield) 31P NMR (δ, D2O) -3.1

Synthesis of $K_3PW_{12}O_{40}$

$Na_2WO_4.2H_2O$ (100 g, 0.3 moles) and Na_2HPO_4 (50 g, 281 mmol) were suspended in water (100 mL) and refluxed for 45 mins. HCl (12.1 M, 100 mL) was added and the resulting mixture was refluxed overnight, resulting in a yellow solution with a white precipitate. The precipitate was filtered, then recrystallized from the minimum amount of hot water, giving a white crystalline. The white crystalline solid was then dissolved in water (10 ml) and KCl (30g) was added. The resulting suspension was then stirred for 6 hours.

After this the suspension was then rotary evaporated to remove any excess solvent and left in a desiccator for two days to dry. (57.5 g, 76.7%). 31P NMR (D2O) (δ, ppm) -15.30.

Synthesis of $K_3PMo_{12}O_{40}$

$Na_2MoO_4·2H_2O$ (100g, 0.3 moles) $Na_2WO_4.2H_2O$ (100 g, 0.3 moles) and Na_2HPO_4 (50 g, 281 mmol) were suspended in water (100 mL) and refluxed for 45 mins. HCl (12.1 M, 100 mL) was added and the resulting mixture was refluxed overnight, resulting in a yellow solution with a white precipitate. The precipitate was filtered, then recrystallized from the minimum amount of hot water, giving a white crystalline. The white crystalline solid was then dissolved in water (10 ml) and KCl (30g) was added. The resulting suspension was then stirred for 6 hours.

After this the suspension was then rotary evaporated to remove any excess solvent and left in a desiccator for two days to dry. (6.5 g, 16%). 31P NMR (D2O) (δ, ppm) -13.2

Synthesis of $K_3PMo_{12}O_{40}$@GNF

GNFs (10.0 mg) were heated to 500 ^{O}C for 40 minutes. The resulting black solid was then added to a rapidly stirred solution of $K_3PMo_{12}O_{40}$ in water (0.05M). On addition of the GNF to the solution, the solution did not change colour. The mixture was briefly sonicated for 5 minutes and the resulting dispersion was stirred for 2 days at room temperature (25^{O}C). The black suspension was then filtered through a PTFE filter, giving a colourless liquid and a black solid, which was then dried in the desiccator for 2 days.

Synthesis of $K_3PW_{12}O_{40}$@GNF

GNFs (10.0 mg) were heated to 500 ^{O}C for 40 minutes. The resulting black solid was then added to a rapidly stirred solution of $K_3PW_{12}O_{40}$ in water (0.05M). On addition of the GNF to the solution, the solution did not change colour. The mixture was briefly sonicated for 5 minutes and the resulting dispersion was stirred for 2 days at room temperature (25^{O}C). The black suspension was then filtered through a PTFE filter, giving a colourless liquid and a black solid, which was then dried in the desiccator for 2 days.

6.0 References

1. J. M. Cameron, D. J. Wales and G. N. Newton, Dalton Trans., 2018, 47, 5120-5136.

2. M. Sadakane and E. Steckhan, Chem. Rev., 1998, 98, 219-238.

3. B. Keita and L. Nadjo, J. Mol. Catal. A: Chem., 2007, 262, 190-215

4. C. Streb, Dalton Trans., 2012, 41, 1651-1659

5. E. Papaconstantinou, Chem. Soc. Rev., 1989, 18, 1-31.

6. A. Dolbecq, E. Dumas, C. R. Mayer and P. Mialane, Chem. Rev., 2010, 110, 6009-6048

7. J. M. Cameron, S. Fujimoto, K. Kastner, R.-J. Wei, D. Robinson, V. Sans, G. N. Newton and H. H. Oshio, Chem. - Eur. J., 2017, 23, 47-50.

8. Neumann, R. Polyoxometalate complexes in organic oxidation chemistry. Prog. Inorg. Chem. 1998, 47, 317–370.

9. Proust, A.; Thouvenot, R.; Gouzerh, P. Functionalization of polyoxometalates: Towards advanced applications in catalysis and materials science. Chem. Commun. 2008, 1837–1852

10. Ni, L.; Spingler, B.; Weyeneth, S.; Patzke, G.R.TrilacunaryKeggin-typePOMsasversatilebuildingblocksfor lanthanoid silicotungstates. Eur. J. Inorg. Chem. 2013, 2013, 1681–1692.

11. Guo, J.; Zhang, D.; Chen, L.; Song, Y.; Zhu, D.; Xu, Y. Syntheses, structures and magnetic properties of two unprecedentedhybridcompoundsconstructedfromopenWells–Dawsonanionsandhigh-nucleartransition metal clusters. Dalton Trans. 2013, 42, 8454–8459.

12. Zhang, F.-Q.; Guan, W.; Yan, L.-K.; Zhang, Y.-T.; Xu, M.-T.; Hayfron-Benjamin, E.; Su, Z.-M. On the origin of therelativestabilityofWells–Dawsonisomers: ADFTstudyof α-, β-, γ-, α*-, β*-, and γ*-[(PO4)2W18O54]6´ anions. Inorg. Chem. 2011, 50, 4967–4977.

13. Kato, C.N.; Kashiwagi, T.; Unno, W.; Nakagawa, M.; Uno, H. Syntheses and molecular structures of monomeric and hydrogen-bonded dimeric Dawson-type trialuminum-substituted polyoxotungstates derived under acidic and basic conditions. Inorg. Chem. 2014, 53, 4823–4832

14. Carraro, M.; Bassil, B.S.; Sorarù, A.; Berardi, S.; Suchopar, A.; Kortz, U.; Bonchio, M. A Lewis acid catalytic core sandwiched by inorganic polyoxoanion caps: Selective H2O2-based oxidations with [AlIII4(H2O)10(β-XW9O33H)2]6´ (X=AsIII,SbIII). Chem. Commun. 2013,49,7914–7916.

15. Zhu, G.; Geletii, Y.V.; Zhao, C.; Musaev, D.G.; Song, J.; Hill, C.L. A dodecanuclear Zn cluster sandwiched by polyoxometalate ligands. Dalton Trans. 2012, 41, 9908–9913.

16. Jameel, Umsa & Zhu, Mingqiao & Chen, Xinzhi & Tong, Zhangfa. (2015). Recent progress of synthesis and applications in polyoxometalate and nanogold hybrid materials. Journal of Materials Science. 51. 10.1007/s10853-015-9503-1.

17. Limanski, E.M.; Drewes, D.; Krebs, B. Sandwich-like polyoxotungstates with indium (III) as a heteroatom synthesis and characterization of the first examples of a new type of anions. Z. Anorg. Allg. Chem. 2004, 630, 523–528

18. Kazuhiro Uehara, Tatsuya Taketsugu, Kazuhiro Yonehara, and Noritaka Mizuno . Effects of Isolobal Heteroatoms in Divanadium-Substituted γ-Keggin-type Polyoxometalates on (OV)2(μ-OH)2 Diamond and (OV)2(μ-O) Core Structures and the Transformation. Inorganic Chemistry 2013, 52 (2) , 1133-1140. DOI: 10.1021/ic302508c

19. Masahiro Sadakane, Yoshifumi Iimuro, Daisuke Tsukuma, Bassem S. Bassil, Michael H. Dickman, Ulrich Kortz, Yi Zhang, Shen Ye, Wataru Ueda. Carbonyl–ruthenium substituted α-Keggin-tungstosilicate, [α-SiW11O39RuII(CO)]6−: synthesis, structure, redox studies and reactivity. Dalton Transactions 2008, 30 (47) , 6692. DOI: 10.1039/b810987g.

20. Nakamura, S.; Ozeki, T. Guest driven rearrangements of protonation and hydrogen bonding in decavanadate anions as their tetraalkylammonium salts. Dalton Trans. 2008, 6135–6140. 71

21. Fang, X.; Hill, C.L. Multiple reversible protonation of polyoxoanion surfaces: Direct observation of dynamic structural effects from proton transfer. Angew. Chem. Int. Ed. 2007, 46, 3877–3880.

22. Müller, A.; Krickemeyer, E.; Bögge, H.; Schmidtmann, M.; Beugholt, C.; Kögerler, P.; Lu, C. Formation of a Ring-Shaped Reduced “Metal Oxide” with the Simple Composition [(MoO3)176(H2O)80H32]. Angew. Chem. Int. Ed. 1998, 37, 1220–1223

23. M. T. Pope, A. Muller, Angew. Chem. hit. Ed, Engl., 30,34, (1991)

24. D. H. Brown and J. A. Mair, J. Chem. Soc., 1958, 2597. (b) P. Souchay and R. Contant , Bull. Soc. Chim. Fr., 1973, 3287. (c) S. C. Termes and M. T. Pope, Transition Met. Chem., 1978, 3, 103.

25. K. Don D. Gunaratne, Grant E. Johnson, Amity Andersen, Dan Du, Weiying Zhang, Venkateshkumar Prabhakaran, Yuehe Lin, and Julia Laskin . Controlling the Charge State and Redox Properties of Supported Polyoxometalates via Soft Landing of Mass-Selected Ions. The Journal of Physical Chemistry C 2014, 118 (48) , 27611-27622. DOI: 10.1021/jp505050m

26. Zhang, F.-Q.; Guan, W.; Yan, L.-K.; Zhang, Y.-T.; Xu, M.-T.; Hayfron-Benjamin, E.; Su, Z.-M. On the origin of therelativestabilityofWells–Dawsonisomers: ADFTstudyof α-, β-, γ-, α*-, β*-, and γ*-[(PO4)2W18O54]6´ anions. Inorg. Chem. 2011, 50, 4967–4977.

27. Wu, H.: 1920, J.Biol.Chem., 43, p. 189.

28. Synthesis, structures and applications of electron-rich polyoxometalates

Nadiia I. Gumerova and Annette Rompe lNat Rev Chem, 2018, 2 DOI: 10.1038/s41570-018-0112

29. Keita, Bineta & NADJO, L. (1989). New oxometalate-based materials for catalysis and electrocatalysis. Materials Chemistry and Physics - MATER CHEM PHYS. 22. 77-103. 10.1016/0254-0584(89)90032-1.

30. Sokolov, Maxim & Adonin, Sergey & Mainichev, Dmitry & Sinkevich, Pavel & Vicent, C & Kompankov, Nikolay & Gushchin, Artem & Nadolinny, V. & Fedin, V.. (2013). New {RuNO} polyoxometalate [PW11O39Ru(II)(NO)]4-: synthesis and reactivity. Inorganic chemistry. 52. 10.1021/ic401492q.

31. B. Keita and L. Nadjo, J. Electroanal. Chem. Interfac. Electrochem., 1988, 240, 325-332.

32. Hill C. L., Prosser-McCartha C. M. (1995). Homogeneous catalysis by transition metal oxygen anion clusters. Coord. Chem. Rev. 143, 407–455.

33. Ronny Neumann and Mohammad Gara Journal of the American Chemical Society 1994 116 (12), 5509-5510

34. Iijima, S. Helical microtubules of graphitic carbon. Nature 354, 56–58 (1991) doi:10.1038/354056a0

35. Gately, R. D.; in het Panhuis, M. Beilstein J. Nanotechnol. 2015, 6, 508–516.

36. P.M.F.J. Costa, et al.Comparative study of the stability of sulfide materials encapsulated in and expelled from multi-walled carbon nanotube capsules Carbon, 49 (1) (2011), pp. 342-346

37. Synthesis and properties of filled carbon nanotubes Diam. Relat. Mater., 12 (3–7) (2003), pp. 790-793

38. B. Keita, L. Nadjo and J. Haeussler, J. Electroanal. Chem. Interfac. Electrochem., 1988, 243, 481-491.

39. D.P. Tang, B.L. Su, J. Tang, Q.F. Li, G.N. Chen

40. B. Su, D. Tang, J. Tang, Q. Li, G. ChenAn organic–inorganic hybrid nanostructure-functionalized electrode for electrochemical immunoassay of biomarker by using magnetic bionanolabels Analytical Biochemistry, 417 (1) (2011), pp. 89-96

41. J. Kong, M.G. Chapline, H.J. DaiFunctionalized carbon nanotubes for molecular hydrogen sensors Advanced Materials, 13 (18) (2001), pp. 1384-1386

42. Hamada, N.; Sawada, S.; Oshiyama, A. (1992). "New one-dimensional conductors: graphitic microtubules". Phys. Rev. Lett. 68 (10): 1579–1581.

43. Mithin Kumar S., Arun S., Mayavan S. Effect of carbon nanotubes with varying dimensions and properties on the performance of lead acid batteries operating under high rate partial state of charge conditions Journal of Energy Storage, Volume 24, 2019

44. B.M. Kim, S. Qian, H.H. Bau, Filling carbon nanotubes with particles, Nano Letters, 5 (2005) 873-878.

45. G. Korneva, H. Ye, Y. Gogotsi, D. Halverson, G. Friedman, J.-C. Bradley, K.G. Kornev, 47 Carbon nanotubes loaded with magnetic particles, Nano letters, 5 (2005) 879-884.

46. Z. Zhang, B. Li, Z. Shi, Z. Gu, Z. Xue, L. Peng, Filling of single-walled carbon nanotubes with silver, Journal of Materials Research, 15 (2000) 2658-2661.

47. A. Govindaraj, B. Satishkumar, M. Nath, C.N.R. Rao, Metal nanowires and intercalated metal layers in single-walled carbon nanotube bundles, Chemistry of Materials, 12 (2000) 202-205.

48. W. A. Solomonsz , G. A. Rance and A. N. Khlobystov,Small,2014, 10,1866–1872

49. M. d. C. Gimenez-Lopez, A. Kurtoglu, D. A. Walsh and A. N. Khlobystov, Adv. Mater., 2016, 28, 9103-9108

50. G. A. Rance , W. A. Solomonsz , A. N. Khlobystov , Chem. Commun., 2013,49,1067-1069.

51. Ramirez-Barria C.S., Isaacs M., Parlett C., Wilson K., Guerrero-Ruiz A., Rodríguez-Ramos I.

52. Brownlie L., Shapter J.Advances in carbon nanotube n-type doping: Methods, analysis and applications Carbon, Volume 126, 2018

53. Corma, A.; Garcia, H.; Leyva, A. Catalytic activity of palladium supported on single wall carbon nanotubes compared to palladium supported on activated carbon: Study of the Heck and Suzuki couplings, aerobic alcohol oxidation and selective hydrogenation. J. Mol. Catal. A Chem. 2005, 230, 97–105.

54. Beletskaya, I.P.; Cheprakov, A.V. The Heck reaction as a sharpening stone of palladium catalysis. Chem. Rev. 2000, 100, 3009–3066

55. P.Zhang, H. Lu, Y. Zhou, L. Zhang, Z. Wu, S. Yang, H. Shi, Q. Zhu, Y. Chen and S. Dai, Nat. Commun., 2015, 6,8446, 1-10.

56. Christian, Patsy & von der Kammer, Frank & Baalousha, Mohammed & Hofmann, Thilo. (2008). Nanoparticles: Structure, Properties, Preparation and Behaviour in Environmental Media. Ecotoxicology (London, England). 17. 326-43. 10.1007/s10646-008-0213-1.

57. T. W. Chamberlain, T. Zoberbier, J. Biskupek, A. Botos, U. Kaiserb and A. N. Khlobystov, Chem. Sci., 2012, 3, 1919-1924

58. E. Philp, J. A. Sloan, I.Kirkland, R. R. Meyer, S.Friedrichs, , J. L. Hutchison and M. L. H. Green, Nat. Mater., 2003, 2, 788–791.

59. W. Chen, X. Pan, X. Bao, J. Am. Chem. Soc., 2007, 129, 7421 –7426.

60. Meek, S. T., Greathouse, J. A. & Allendorf, M. D. Metal-organic frameworks: a rapidly growing class of versatile nanoporous materials. Adv. Mater. 23, 249–267 (2011).

61. R. M. M. Abbaslou, A. Tavassoli, J. Soltan and A. K. Dalai, Appl. Catal. A: Gen., 2009, 367, 47–52.

62. S. Guo, X. Pan, H. Gao, Z. Yang, J. Zhao and X. Bao, Chem. Eur. J., 2010,16, 5379–5384

63. Pedro M. F. J. Costa, Jeremy Sloan, Thomas Rutherford and Malcolm L. H. Green Chemistry of Materials 2005 17 (26), 6579-6582

64. Z. Guan, S. Lu and C. Li, J. Catal., 2014, 311,1–5

65. Das, Tapas & Banerjee, Seemita & Dasgupta, Kinshuk & Joshi, J & Sudarsan, V. (2015). Nature of Pd-CNT interaction in Pd nanoparticles dispersed multi-walled carbon nanotubes and its implications in Hydrogen storage properties. RSC Adv.. 5. 10.1039/C5RA03508B.

66. D. Wang, G. Yang, Q. Ma, M. Wu, Y. Tan, Y. Yoneyama and N. Tsubaki, ACS Catal., 2012, 2, 1958 – 1966.

67. . Xiao, J. Hwang, I. Belharouak, Y. Sun, Na-storage capability investigation of carbon nanotubes-encapsulated $Fe_{1-x}S$ composite. ACS Energy Lett. 2(2), 364–372 (2017).

68. W. Chen, L. Huang, J. Hu, T. Li, F. Jia and Y.-F. Song, Phys. Chem. Chem. Phys., 2014, 16, 19668-19673.

69. F. M. Toma, A. Sartorel, M. Iurlo, M. Carraro, P. Parisse, C. Maccato, S. Rapino, B. R. Gonzalez, H. Amenitsch, T. Da Ros, L. Casalis, A. Goldoni, M. Marcaccio, G. Scorrano, G. Scoles, F. Paolucci, M. Prato and M. Bonchio, Nat Chem, 2010, 2, 826-831.

70. Debiemme-Chouvy, Catherine & Thomas, Benjamin & Lucas, Ivan & Tran, MaïTT & Heintz, Jean-Marc & Veillère, A. & Silvain, J.-F. (2016). Facile and green reduction of graphene oxide by a reduced polyoxometalate and nanohybrid formation. ChemPlusChem. 82. 10.1002/cplu.201600484.

71. Liu, Rongji & Xian, Zhaowei & Zhang, Shuangshuang & Chen, Chunhua & Yang, Zhihua & Li, Hang & Zheng, Wanquan & Zhang, Guangjin & Cao, Hongbin. (2015). Electrochemical-reduction-assisted assembly of ternary Ag nanoparticles/polyoxometalate/graphene nanohybrids and their activity in the electrocatalysis of oxygen reduction. RSC Adv.. 5. 74447-74456. 10.1039/C5RA12556A.

72. Toma, F., Sartorel, A., Iurlo, M. et al. Efficient water oxidation at carbon nanotube–polyoxometalate electrocatalytic interfaces. Nature Chem 2, 826–831 (2010) doi:10.1038/nchem.761

73. Impregnated Electroreduced Pt on Ru/C as an Anode Catalyst for Direct Methanol Fuel CellsJ. Electrochem. Soc. 2019 166(15): F1173-F1179

74. D. Pan , J. Chen , W. Tao , L. Nie and S. Yao , Langmuir, 2006, 22 , 5872 —5876